

Imperial College London

Department of Mechanical Engineering  
Advanced Mechanical Engineering Course

---

**Simulation of injection-moulded composite structures for  
automotive applications**

---

*Author:*

Yeung Chak Hoi Wisely

*Supervisor:*

Dr. Soraia Pimenta

*Co-Supervisor:*

Mr. Yuki Fujita

A thesis submitted in partial fulfilment of the requirements for the Master of Science Degree  
of Imperial College London and the Diploma of Membership of Imperial College

Date: September 9, 2023

*Word limit:* 18000

*Word count:* 15118

# Abstract

Short fibre reinforced plastics (SFRP) for structural applications in the automotive industry have been rapidly growing owing to their multiple material advantages over metals. Nonetheless, the distinct features of Fibre Orientation Distribution (FOD) lead to a heterogeneous and anisotropic material behaviour. Precise prediction of failure in complex SFRP structures remains a challenge. This research project, divided into three main phases, aims to improve the understanding and modelling of the mechanics of injection moulded SFRP (IM-SFRP) components.

Phase 1 investigates the energy dissipation mechanisms of SFRP under multi-axial loading, to address the overestimation problem observed in puncture test simulations conducted by Yuki Fujita. This research utilises a single fibre matrix Representative Volume Element (RVE) model of SFRP. Cohesive Zone Modelling (CZM) was found to be crucial in simulating the failure mechanism of SFRPs and modelling the behaviour of the fibre and matrix interface. Furthermore, results of the RVE model exhibited higher combined plastic and damage dissipation energy in the multi-axial stress state than in the uniaxial axial stress. This rejects the hypothesis that lower fracture toughness caused the overestimation of failure load, demanding further inquiry into the failure mechanisms.

Phase 2 assesses virtual testing methodologies for PA66-GF50 Engine Mount (EM) components. Coupling injection-moulding and Finite Element (FE) analysis with Cohesive Elements (CE) yields accurate structural behaviour and failure load predictions under tensile test simulations. Nevertheless, this research reveals software limitations in Digimat, prompting the need for enhanced automation in Fiber Orientation (FO) mapping for CE.

Phase 3 delves into the experimental testing of the compressive properties of IM-SFRP. Variations in compressive modulus and strength are observed across different FO. Notably, specimens with  $0^\circ$  FO exhibit higher compressive modulus values compared to  $45^\circ$  and  $90^\circ$  FO. Moreover, SFRP specimens under compression demonstrated greater ultimate strength at a greater strain compared to tension. Limitations in the current compression test methodology are identified, especially for  $45^\circ$  and  $90^\circ$  FO specimens, where global failures in those FO were restricted by the clearance between the jig and the specimen. Alternative testing configurations along with specimen dimension adjustments were proposed for a more comprehensive understanding of SFRP compressive properties.

The distinct tensile and compressive behaviours of SFRP revealed in Phase 3 underscore the necessity for an integrated approach in future research. These differences offer a critical key to fine-tuning the predictive models in Phases 1 and 2. Future work should therefore leverage the material properties identified in Phase 3 to enhance the multi-axial stress models of Phase

1 and the virtual testing methodologies of Phase 2. This helps achieve a more holistic and accurate understanding of IM-SFRP failure mechanisms, laying the groundwork for scalable, resource-efficient testing procedures for automotive components manufacturing.

## Acknowledgements

I would like to express my heartfelt appreciation to my supervisor, Dr. Soraia Pimenta, for her invaluable guidance and continuous support throughout my research journey. Her advice and expertise have been instrumental in enabling the successful completion of my research.

I am grateful to my co-supervisor, Mr. Yuki Fujita for his academic assistance in refining the scope and focus of my research. His generosity in sharing professional insights and experiences has enriched my academic pursuits immeasurably.

Lastly, I would also like to extend my special thanks to Mr. Keith Wolstenholme and Mr. Suresh Viswanathan Chettiar, for their assistance in setting up the compression experiment.

# Contents

<b>Abstract</b>	<b>III</b>
<b>Acknowledgements</b>	<b>IV</b>
<b>List of Figures</b>	<b>X</b>
<b>List of Tables</b>	<b>X</b>
<b>1 Introduction</b>	<b>1</b>
<b>2 Literature Review</b>	<b>3</b>
2.1 Tensile Behaviour of SFRPs . . . . .	3
2.1.1 Macro-mechanical Approach . . . . .	3
2.1.2 Micro-mechanical Approach . . . . .	4
2.1.3 Biaxial Behaviour . . . . .	4
2.1.4 Puncture Tests and Simulations . . . . .	5
2.1.5 Triaxiality . . . . .	7
2.2 Compression Behaviour of SFRPs . . . . .	8
2.3 Fracture Toughness and Impact Behaviour . . . . .	11
2.3.1 Methodologies for Measuring Fracture Toughness in SFRPs . . . . .	11
2.3.2 Numerical Implications of the Fracture Toughness . . . . .	12
2.4 Failure Prediction and Cohesive Zone Modelling . . . . .	13
2.4.1 Bi-linear Traction-Separation Law . . . . .	13
2.4.2 Damage Initiation . . . . .	14
2.4.3 Damage Evolution . . . . .	15
2.5 Existing Virtual Testing Methodology . . . . .	15
2.5.1 Manufacture Processing . . . . .	16
2.5.2 Structure FEA Mapping . . . . .	16
2.5.3 Coupled Simulations . . . . .	17
<b>3 Phase 1 - Investigation of the Failure of SFRP under Multi-axial Stress State</b>	<b>18</b>
3.1 Methodology . . . . .	18
3.1.1 Geometry of the Finite Element Model . . . . .	18
3.1.2 Boundary Condition . . . . .	19
3.1.3 Material Properties without Failure Criteria . . . . .	20
3.1.4 Introduction of Cohesive Elements . . . . .	20
3.1.5 Mesh Convergence Study . . . . .	23
3.2 Results . . . . .	23
3.2.1 Effect of Cohesive Elements . . . . .	23
3.2.2 Effect of the Geometrical Gap . . . . .	24

3.2.3	Validation of the Hypothesis . . . . .	26
3.2.4	Parametric Study . . . . .	28
3.3	Discussion . . . . .	29
3.3.1	Criticality of CZM . . . . .	29
3.3.2	Validation of the Hypothesis . . . . .	30
<b>4</b>	<b>Phase 2 - Simulation of IM-SFRP EM using coupled FEA</b>	<b>31</b>
4.1	Methodology . . . . .	31
4.1.1	Geometry of the Finite Element Model . . . . .	31
4.1.2	Boundary Conditions . . . . .	32
4.1.3	Material Properties . . . . .	35
4.1.4	Discretisation & Mesh Convergence Study . . . . .	39
4.1.5	Coupled FE Analysis . . . . .	42
4.2	Results . . . . .	44
4.2.1	Determining Optimal Boundary Conditions Configuration . . . . .	44
4.2.2	Experiment Data Modification for the Initial Stiffening Effect . . . . .	44
4.2.3	Coupled FE Analysis with CZM . . . . .	48
4.3	Discussion . . . . .	51
4.3.1	Boundary Condition Analysis . . . . .	51
4.3.2	Stiffness Comparisons . . . . .	52
4.3.3	Failure Predictions . . . . .	52
4.3.4	Investigation of Stiffening Effect . . . . .	53
<b>5</b>	<b>Phase 3 - Experimental investigation of compressive properties of IM-SFRP</b>	<b>54</b>
5.1	Experimental Methods and Specimen Manufacture . . . . .	54
5.1.1	Test Apparatus . . . . .	54
5.1.2	Specimen Preparation . . . . .	55
5.1.3	Experimental Setup . . . . .	56
5.1.4	Experimental Procedure . . . . .	57
5.2	Results . . . . .	58
5.2.1	Stress-Strain Curves . . . . .	58
5.2.2	Specimen Scans . . . . .	61
5.2.3	0° Specimen Failure Cycle Analysis . . . . .	62
5.3	Discussion . . . . .	63
5.3.1	Preliminary Compressive Properties . . . . .	63
5.3.2	Limitations of the Current Compression Test Methodology . . . . .	64
<b>6</b>	<b>Conclusion</b>	<b>65</b>
6.1	Summary of Key Findings . . . . .	65
6.2	Implications . . . . .	66

<b>7</b>	<b>Future Work</b>	<b>67</b>
7.1	Phase 1 . . . . .	67
7.2	Phase 2 . . . . .	68
7.3	Phase 3 . . . . .	68
7.4	Integration Across Phases . . . . .	70
<b>A</b>	<b>Appendix</b>	<b>78</b>
A.1	Halpin-Tsai SFRP model . . . . .	78
A.2	Effect of EM sliding . . . . .	78

## List of Figures

1	Schematic fibre layer structure of IM-SFRPs [1]. . . . .	1
2	Engine mount bracket manufactured by Asahi Kasei [2]. . . . .	2
3	SFRP in (a) Macroscopic scale, (b) Microscopic scale [3] . . . . .	3
4	PA66-GF60 specimen puncture test [4]. . . . .	5
5	Puncture test on rectangular SFRP specimen [4] . . . . .	6
6	FE model of the puncture test [4]. . . . .	6
7	Puncture test simulation results. . . . .	7
8	Tensile Engineering stress–engineering strain curves of PA6-20CF specimens with different strain rates. (a) $\theta = 0^\circ$ , (b) $\theta = 45^\circ$ , (c) $\theta = 90^\circ$ [5]. . . . .	9
9	Compressive Engineering stress–engineering strain curves of PA6-20CF specimens with different strain rates. (a) $\theta = 0^\circ$ , (b) $\theta = 45^\circ$ , (c) $\theta = 90^\circ$ [5]. . . . .	9
10	SEM fracture mechanism observed for compressive specimens: (left) magnification: $\times 200$ , scale: $100\mu\text{m}$ , (middle) magnification: $\times 350$ , scale: $10\mu\text{m}$ , (right) magnification: $\times 10,000$ , scale: $1\mu\text{m}$ [5]. . . . .	11
11	Initiation and propagation fracture toughness of $0^\circ$ FO specimens calculated using the compliance calibration and J-integral methods. Error bars represent one standard deviation [4]. . . . .	12
12	Load-displacement curves of CT specimens under $23^\circ\text{C}$ -DAM conditions, comparing results from the experimental tests and FE simulation using bilinear and trilinear cohesive laws, for two machining angles: (a) $0^\circ$ and (b) $90^\circ$ [4]. . . . .	13
13	Typical traction separation behaviour when a fibre is pulled out from the matrix [6]. . . . .	14
14	Flowchart of the direct transfer of the Moldflow simulation data to Abaqus analysis. . . . .	16
15	Single fibre matrix RVE geometry. . . . .	19
16	Loading boundary conditions. . . . .	19
17	True stress-strain curve of PA66 [7]. . . . .	20
18	Geometry of the single fibre matrix RVE model with CZM. . . . .	21
19	Bad adhesion region represented by an empty gap. . . . .	21
20	Mesh convergence study on 0.3 PEEK. . . . .	23
21	Plastic Strain at total strain $\epsilon = 0.02$ . . . . .	24
22	Comparison of Stress-Strain Curves: FE Model with gap vs. FE Model without gap, in relation to experimental test curve for FO tensor $a_{11}=0.9$ . . . . .	25
23	Comparison of Stress-Strain Curves: FE Model without gap vs. FE Model without gap and with stabilisation, in relation to experimental test curve for FO tensor $a_{11}=0.9$ . . . . .	25
24	Stress-strain curve of longitudinal uniaxial loading (blue), longitudinal biaxial loading (orange) and transverse biaxial loading (yellow). . . . .	26



25	Energy dissipation of the uniaxial, biaxial, and triaxial loading per unit cell. . .	28
26	Comparative energy dissipation curves for Mode II and III traction stresses ( $T_s$ , $T_t$ ) and critical fracture energies ( $G_s^C$ , $G_t^C$ ) in the parametric study. . . . .	29
27	Tensile test setup for the IM-SFRP fabricated EM. . . . .	31
28	3D geometry of the EM. . . . .	32
29	Schematic of the baseline FE model. . . . .	33
30	Schematic of the 'analytical rigid pin' FE model. . . . .	33
31	Schematic of the 'bottom constraint' FE model. . . . .	34
32	Schematic of the 'fixture constraint' FE model. . . . .	34
33	Schematic of the 'without legs' FE model. . . . .	35
34	Schematic of the 'without legs with bottom constraint' FE model. . . . .	35
35	After-test EM specimen indicating the weldline location. . . . .	36
36	Locations of the CE in the EM cross-section. . . . .	37
37	Injection-moulding simulation and SEM image illustrating skin-core ratio. . . .	38
38	Partitioning schemes for the top-of-the-arc CE. . . . .	38
39	EM partitions illustrating the pentagon meshing technique. . . . .	40
40	Meshing of the EM. . . . .	40
41	Meshing of the loading pin. . . . .	41
42	Mesh convergence study on the number of mesh layers. . . . .	41
43	Mesh convergence study on the CE sizes. . . . .	42
44	Moldflow injection-moulding simulations. . . . .	43
45	Mapping of fibre orientation in Digimat-MAP. . . . .	43
46	Load Displacement curves of various boundary conditions with the modified experiment results (explored in Section 4.2.2). . . . .	44
47	Load-Displacement curves of the tensile experiments. . . . .	45
48	Side trackers on the EM in tensile experiments. . . . .	46
49	Schematic of pin offset by 5mm in the x-direction. . . . .	47
50	Schematic of pin offset in the y-direction. . . . .	47
51	Load-Displacement curves of pin shift simulations versus without pin shift. . .	48
52	Modified Load-Displacement curves of the tensile experiments. . . . .	48
53	Load-Displacement curves of the coupled FE analysis with CE for top-of-the-arc failures. . . . .	49
54	Load-Displacement curves of the coupled FE analysis with CE for weldline failures.	50
55	Direction and location of specimens cut from injection moulded plaques (arrows indicate the injection moulding direction and the dashed areas are discarded materials) [8]. . . . .	56
56	Dogbone specimen dimensions for compressive testing. . . . .	56
57	Compressive test configurations. . . . .	57
58	Compressive stress-strain curves for IM-SFRP dogbone specimens. . . . .	59
59	Tensile and compressive stress-strain curves for IM-SFRP dogbone specimens. .	60

60	After-test scans of specimen batch 2. . . . .	62
61	After-test scans of specimen batch 3. . . . .	62
62	Compressive stress-strain curves for IM-SFRP dogbone specimens undergone three loading cycles. . . . .	63
63	After-test scans of 0° specimen cycle 2 and 3. . . . .	63
64	Alternative test standards for compressive properties. . . . .	69
65	Regions of the EM under compressive stress state. . . . .	70
A.1	Horizontal displacements of the left tracker recorded in tensile tests. . . . .	78
A.2	Vertical displacements of the left tracker recorded in tensile tests. . . . .	79
A.3	Horizontal displacements of the right tracker recorded in tensile tests. . . . .	79
A.4	Vertical displacements of the right tracker recorded in tensile tests. . . . .	80

## List of Tables

1	CE failure properties for puncture test simulations [4]. . . . .	7
2	Isotropic material properties of E-glass fibre and PA66 epoxy matrix. . . . .	20
3	Failure traction stress and fracture energy for CE. . . . .	22
4	Parametric study on failure parameters. . . . .	28
5	Isotropic material properties at 23 °C DAM condition of the EM and loading pin. . . . .	36
6	CE material properties for different partitioning schemes. . . . .	38
7	Initial stiffness and failure loads of the modified tests and coupled FE simulations for top-of-the-arc failures. . . . .	49
8	Initial stiffness and failure loads of the modified tests and coupled FE simulations for weldline failures. . . . .	50
9	Key test information. . . . .	54
10	Summary of apparatus selected for compressive test. . . . .	55
11	Tensile and compressive modulus of IM-SFRP dogbone specimens in 0°, 45°, and 90° FO. . . . .	61

# 1 Introduction

Short fibre reinforced plastics (SFRP) have become increasingly popular for structural applications in the automotive industry due to their high mechanical strength-to-weight ratio compared to traditional materials. For instance, an identical component made by PA66-GF50 [9] is five times lighter than that made by AISI-1020 (low carbon steel) [10] while maintaining high material strength. Vehicles such as the Nissan Rogue [11] have pioneered the use of all-thermoplastic composite liftgates in North America, with its lighter weight estimated to reduce fuel consumption by 10 %. Meanwhile, current EU legislation has set mandatory targets to reduce CO<sub>2</sub> emissions for car manufacturers [8], further propelling manufacturers towards the adoption of composite to help reach the target. The benefits of SFRP in cost-effectiveness and production speed, as well as its capability to be manufactured into complex geometries are favourable towards its wider future use in the automotive industry.

One of the main challenges when predicting the failure of injection-moulded SFRP (IM-SFRP) is its complex microstructure resulting from the injection moulding process. Fibre orientation distribution (FOD) in IM-SFRP is highly dependent on the mould thickness, and a continuous variation of FOD through the thickness is observed after the injection-moulding process [8]. Two shell layers and a core layer are produced as a result of the shear effect induced by the velocity profile over the mould thickness, illustrated in Figure 1. In the shell layers, fibres are mainly oriented parallel to the flow direction, whereas, in the core layer, fibres are mainly oriented perpendicularly. The polymer flow-dependent fibre orientation (FO) overall leads to anisotropic and heterogeneous material behaviour. Moreover, FO is also influenced by the temperature gradient, filling time, injection pressure and injection point [12]. This results in the FO never being completely unidirectional or homogeneous. Thus, mechanical testing of SFRP is only an average measure of local properties over the specimen volume.

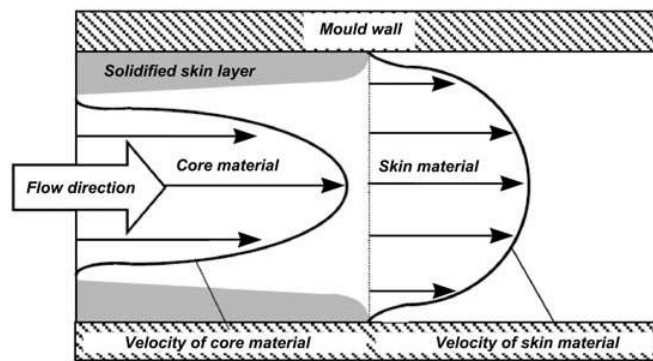


**Figure 1:** Schematic fibre layer structure of IM-SFRPs [1].

Regarding the existing virtual testing methodology for IM-SFRPs, there have been extensive research studies [3, 8, 12–18] conducted using structural simulation (i.e. Finite-Element (FE)) software coupled with the simulation of the injection-moulding process. While high accuracies of  $\approx 90\%$  [7, 19] have been achieved in stress-strain relation for single-point injection

specimens, this accuracy of simulations diminishes with increasing structural complexity and multiple weldlines arising from multiple nozzle injections.

At present, three primary obstacles hinder the precise modelling of the mechanical behaviour of IM-SFRP. Firstly, regarding the virtual testing methodology, Y. Fujita [4] has demonstrated that utilising a coupled injection-moulding process and finite-element solver with Cohesive Zone Modelling (CZM) can provide an accurate estimation of failure for components under a uniaxial stress state. However, discrepancies arise when simulating the triaxial stress state of SFRP in puncture tests using the same methodology, as further discussed in Section 2.1.4. These discrepancies resulted in an overestimation of approximately 50 % error in the failure load. One hypothesis is that under a multi-axial stress state, SFRPs might exhibit lower fracture toughness than that in the uniaxial stress state.

Secondly, there is a lack of research in modelling complex industrial IM-SFRP structures to predict their mechanical properties and response, such as the IM-SFRP Engine Mount (EM) as seen in Figure 2. It is an important component used to dampen out the excessive vibration and noise induced by the car chassis and the engine itself. Considering the expanding prospects of SFRP in future automotive applications, establishing virtual testing methodologies for accurate failure prediction is crucial to avoid material waste and over-engineered components being manufactured.



**Figure 2:** Engine mount bracket manufactured by Asahi Kasei [2].

Additionally, the investigation of compressive properties of IM-SFRP has been largely overlooked in existing literature. Components used in the automotive industry are regularly subjected to compressive loading. Therefore, through a series of experimental explorations, this research seeks to bridge the knowledge gap, aiming to identify the failure properties of SFRP under compression, as well as the effect under various factors such as FO and layer morphology.

This research is in collaboration with Asahi Kasei, with the overall aim to improve the current understanding and modelling methodologies of the mechanics of IM-SFRP components, particularly when simulating the behaviour of automotive components under multi-axial stress conditions. To fulfil these research objectives, the project is divided into three phases. Phase 1 entails investigating the failure of SFRP under multi-axial stress state, validating the hy-

pothesis for the failure load overestimation. Phase 2 involves the simulation of IM-SFRP EM using coupled FEA to provide a feasibility study of the virtual testing methodology. Phase 3 conducts an experimental investigation to explore the compressive properties of IM-SFRP for future incorporation into computational modelling.

## 2 Literature Review

### 2.1 Tensile Behaviour of SFRPs

The numerical modelling of SFRPs remains a challenging task due to their highly complex material behaviour, which arises from the randomness of the FOD influenced by the manufacturing process. Different approaches adopted for fracture characterisation of composites can be broadly classified as (i) macro-mechanical and (ii) micro-mechanical approaches [16].

#### 2.1.1 Macro-mechanical Approach

The macro-mechanical approach, as illustrated in Figure 3(a), reduces the complexity by representing the composite as a homogeneous, anisotropic, elastoplastic material. This approximation neglects fine details like the actual FOD and core layer properties [16]. Homogenised material properties such as the elastic constants are obtained directly from experimental off-axis tests as an estimate of the global tensile properties [13].

The macro-mechanical approach offers the advantage of computational simplicity and is generally sufficient for straightforward geometries and loading conditions. However, it can be inadequate for accurately simulating SFRPs with complex geometries or those that cannot be approximated as transversely isotropic. It often fails to capture intricate stress distributions and localised failure mechanisms.

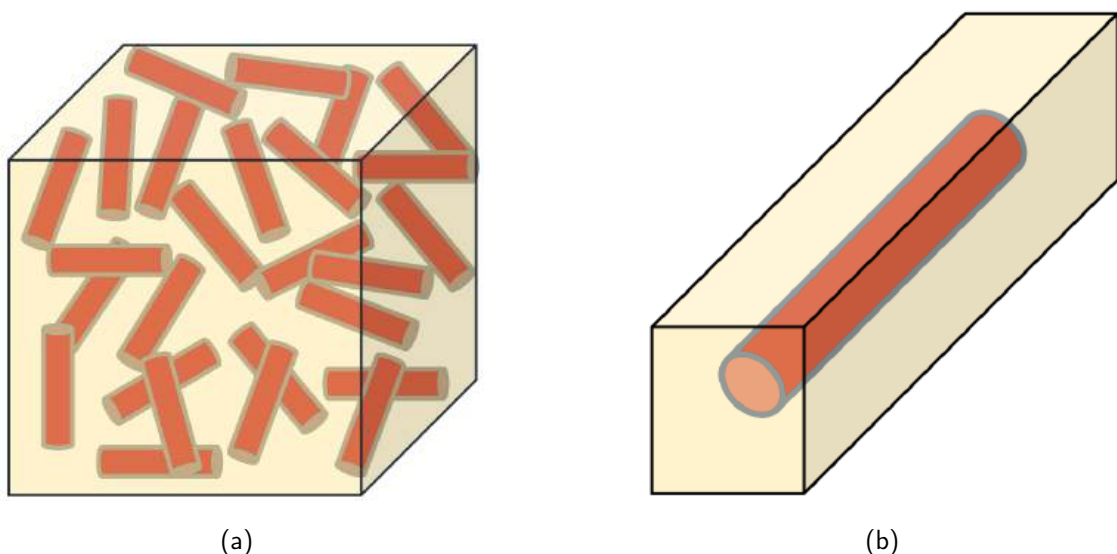


**Figure 3:** SFRP in (a) Macroscopic scale, (b) Microscopic scale [3]

### 2.1.2 Micro-mechanical Approach

On the other hand, the micro-mechanical approach, shown in Figure 3(b), utilises the concept of a representative volume element (RVE). It accounts for material microstructures, such as fibre orientation, through averaging procedures at each point of the macro-structure [20]. This approach was developed to predict composite mechanical properties based on constituent materials, which can also capture detailed energy dissipation mechanisms of both fibre and matrix due to microscale failure modes [21].

In the comparison of the two approaches, only the micro-mechanical approach is capable of capturing the detailed energy dissipation of the fibre and matrix individually. Therefore, this approach will be employed to investigate the energy dissipation mechanism of multi-axial stress state SFRPs, which is crucial for understanding the material's failure behaviour under various loading conditions. On the other hand, the macro-mechanical approach will be applied to the investigation of the EM, focusing on the global behaviour of the component without the need to generate individual fibre-matrix behaviour. This combination of both approaches will provide comprehensive insights into the mechanical properties and fracture behaviour of SFRPs.

### 2.1.3 Biaxial Behaviour

Composite materials used in different industries are regularly subjected to a combination of loads acting in multiple directions, resulting in a multi-directional stress state. Owing to their anisotropic nature, using uniaxial testing procedures does not often obtain the true strengths of these materials under multi-axially loaded conditions [15]. The ability to accurately simulate the multi-axial behaviour of composite ultimately depends on the choice of multi-axial failure criterion. However, accurate failure theories in predicting the behaviour of composites are yet to be determined.

Biaxial loading tests on composite materials can be divided into two major sub-classes: (i) single loading system and (ii) double or more loading system. A single loading system fixes the biaxial stress ratio on the basis of loading fixture configuration or specimen geometry [22], hence loading in one direction results in a material biaxial stress state. Test cases include cantilever beam bending [23], hydraulic bulge test [24], puncture test [7], etc. In multiple loading systems, the magnitude of the loading in each axis determines the biaxial loading ratio. Testing cases include tubular specimens with axial loading with internal/external pressure [25], cruciform specimens [15, 26] etc.

The World-Wide Failure Exercise (WWFE-I) [27] compared 19 different composite material failure theories with existing experimental data of continuous-fibre composite under a biaxial stress state. It was concluded that the most successful failure theory can only predict 75% of

the load cases for tubular specimens. A similar failure exercise WWFE-II [28] focused on the validation and benchmarking of unidirectional continuous-fibre composite lamina failure. Only a few failure theories were able to capture the composite behaviour within  $\pm 50\%$  correlation of test data. These exercises have shown a lack of reliable failure theories in predicting the multi-axial stress state of composites.

A. Rashedi et al. [15] investigated the fracture characteristics of a cruciform laminate under a double-loading system. Leveraging coupled injection-moulding and structural simulation, he demonstrated that failure occurs at a higher stress in a biaxial tensile-tensile loading scenario than in uniaxial failure, indicating a higher load-bearing capability under biaxial tensile-tensile loading. These findings suggest a need to examine the hypothesis that the discrepancies observed in puncture test simulations [4] are explained by lower fracture toughness in multi-axial loading.

#### 2.1.4 Puncture Tests and Simulations

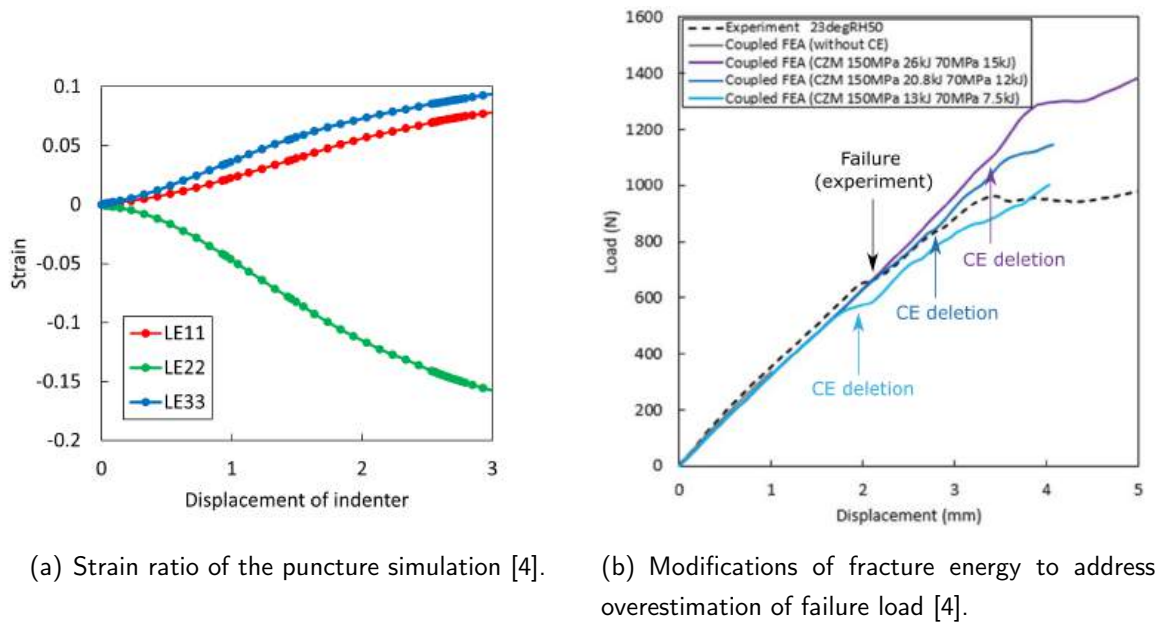
To investigate the failure mechanisms of SFRPs, Y. Fujita [4] performed an experimental puncture test on an IM PA66-GF50 specimen. For this purpose, a rectangular plate specimen was used to induce a multi-axial stress state using a single loading system, as depicted in Figure 4. Initially, a crack was initiated perpendicular to the fibre flow direction, indicating the brittle behaviour of the fibre due to a higher critical stress in the matrix compared to the fibre. The crack then propagated along the flow direction, driven by the increasing stress intensity in the matrix subsequent to fibre failure, resulting in the formation of a cross-shaped crack. The puncture test was deemed completed after the tub penetrated through the specimen in the thickness direction. Figure 5 illustrates the fracture failure process.



Figure 4: PA66-GF60 specimen puncture test [4].







**Figure 7:** Puncture test simulation results.

**Table 1:** CE failure properties for puncture test simulations [4].

	Experiment parameters	Modified parameters 1	Modified parameters 2
Critical stress (skin/core)	150MPa / 70MPa	150MPa / 70MPa	150MPa / 70MPa
Critical fracture energy (skin/core)	26kJ / 15kJ	20.8kJ / 12kJ	13kJ / 7.5kJ

In summary, although the coupled FEA correctly simulated the failure process and its location, there was a 50% overestimation of the failure load when employing the CZM with experimental properties, and a 50% underestimation when applying the Tsai-Hill criterion. More precise failure load predictions were achieved by modifying CE parameters 1 and 2, which involved utilising lower critical fracture energies.

Furthermore, it is noteworthy that despite the absence of a well-established failure theory to predict the multi-axial stress state of SFRPs, Fujita's research successfully demonstrated the potential of the CZM methodology in the context of uniaxial stress. This research will progressively investigate the phenomena observed in Fujita's methodology to predict the multi-axial behaviour of SFRPs.

### 2.1.5 Triaxiality

A profound number of research studies [14, 29–32] have been devoted to developing prediction models of fibre-reinforced polymers, relating their anisotropic material properties to the

mechanical, failure and fatigue behaviour. Camanho et al. [14] and Volger et al. [29] developed a transversely isotropic elastic-plastic constitutive equation for the prediction of fracture onset and propagation by considering the effect of stress triaxiality on the yield surface. L Quagliato et al. [17] later proposed monotonic increasing and decreasing functions, as shown in Equations 1, correlating the failure strain and the stress triaxiality in IM-SFRPs.

$$\begin{aligned} \text{for } 0.33 \leq \eta \leq 0.44 : \quad \epsilon_f &= 1.2836\eta - 0.4000 \quad (R^2 = 0.96) \\ \text{for } 0.44 \leq \eta \leq 0.60 : \quad \epsilon_f &= -0.3224\eta + 0.2956 \quad (R^2 = 0.95) \end{aligned} \quad (1)$$

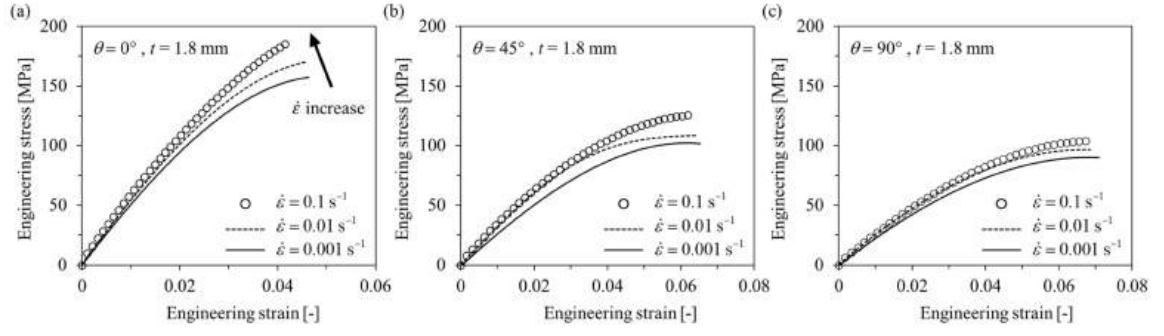
The functions above were obtained using a large data regression model by the mean of a notched tensile model in numerical simulations and laboratory experiments. They were known to be valid and accurate up to 6.8 % maximum error in predicting the failure strain in the range of  $0.33 < \eta < 0.60$ . These can be utilised as a failure criterion for complex geometries fabricated by IM-SFRPs, particularly during the design stage where direct testing is not viable.

During the result validation, L Quagliato et al. [17] concluded that a high value for stress triaxiality in IM-SFRPs is highly undesirable. The cause of high triaxiality is either introduced by a very complex stress concentration scenario, or the FO being developed in an almost random configuration. Regarding the prior issue, complex concentrations such as sharp radii are most likely to become the crack initiation location. The latter issue is caused by a random FOD arising in some regions of complex components, resulting in low mechanical performances regardless of the loading direction. In order to benefit from the high stiffness and strength properties of IM-SFRPs, the injection gates should be positioned to maximise the alignment between the FO direction and the loading direction, thus, reducing the triaxiality of the structural component.

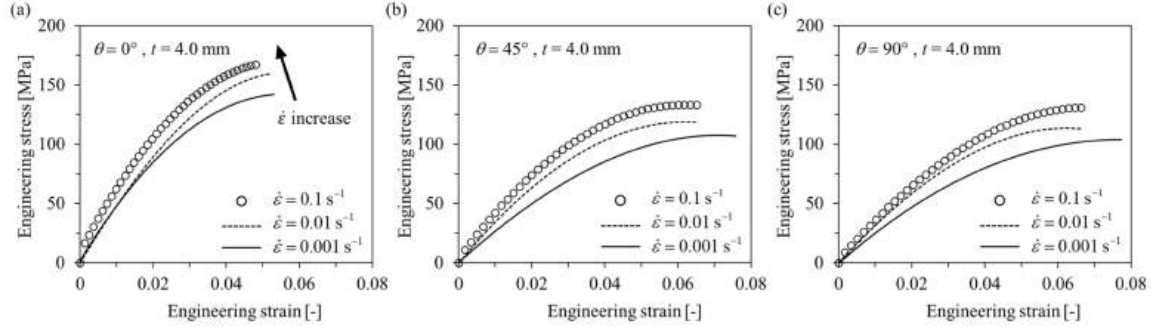
## 2.2 Compression Behaviour of SFRPs

While significant efforts have been devoted to experimentally characterising the mechanical behaviour of SFRP under various tensile loading conditions [4, 7, 12, 13, 33], the understanding of their compressive mechanical behaviour and failure mechanism remains an area that requires further investigation. In the context of Long Fiber Reinforced Plastics (LFRP), numerous studies [34–37] have been developed to explore their compressive mechanical behaviour, identifying the dominant failure mechanism as localised compressive buckling or kinking. However, the unique layered morphology of SFRP introduces anisotropic and heterogeneous material behaviour, significantly influencing their mechanical response and failure mechanism. Consequently, the knowledge derived from studies on LFRP cannot be directly extrapolated for SFRP.

J. Lee [5] recently conducted a series of tensile and compressive experiments on PA6-20CF dogbone specimens with thicknesses of  $t = 1.8\text{mm}$  and  $t = 4.0\text{mm}$ . These experiments were carried out with various FO specimens and under different strain rates. The results are presented in Figures 8 and 9.

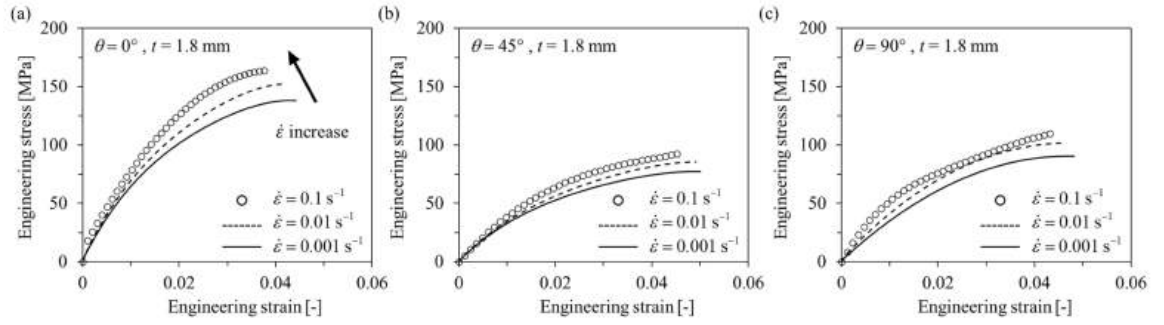


(a)  $t = 1.8\text{mm}$

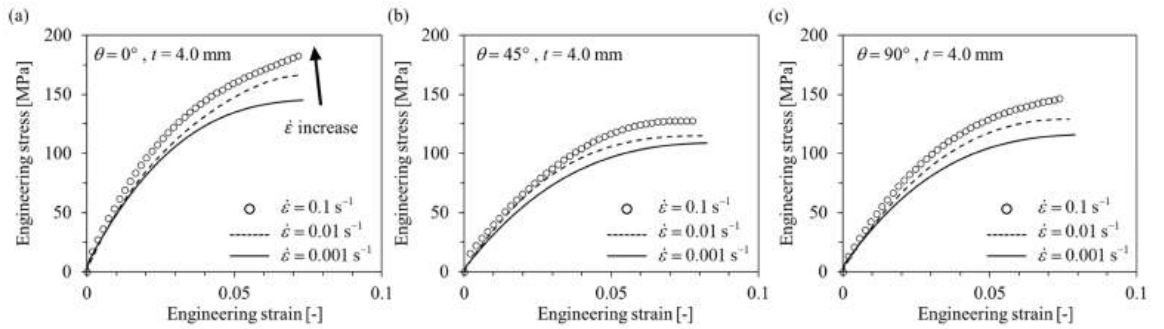


(b)  $t = 4.0\text{mm}$

**Figure 8:** Tensile Engineering stress–engineering strain curves of PA6-20CF specimens with different strain rates. (a) $\theta = 0^\circ$ , (b) $\theta = 45^\circ$ , (c) $\theta = 90^\circ$  [5].



(a)  $t = 1.8\text{mm}$

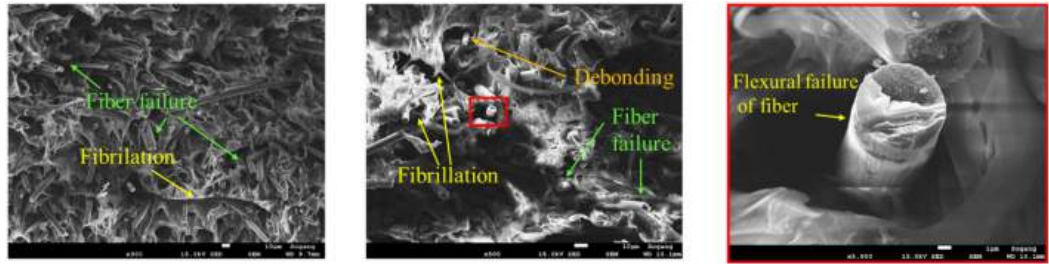


(b)  $t = 4.0\text{mm}$

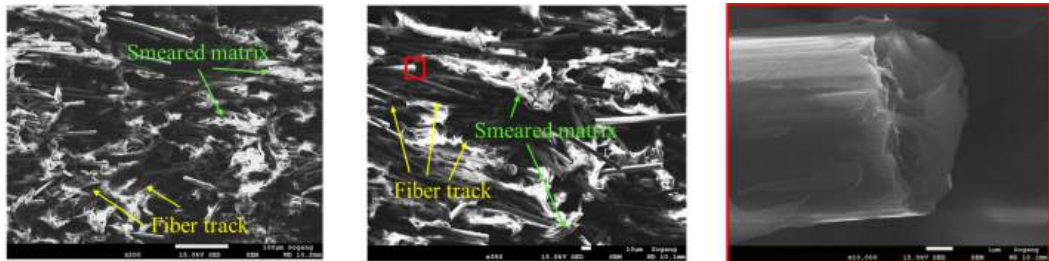
**Figure 9:** Compressive Engineering stress–engineering strain curves of PA6-20CF specimens with different strain rates. (a) $\theta = 0^\circ$ , (b) $\theta = 45^\circ$ , (c) $\theta = 90^\circ$  [5].

Notably, the SFRP specimen exhibited markedly distinct mechanical behaviours under tensile and compressive loading conditions. The lowest ultimate compressive strengths ( $\sigma_{UCS}$ ) were observed with  $\theta = 45^\circ$  FO specimens, and the corresponding ultimate tensile strain ( $\epsilon_{UTS}$ ) exhibited the highest magnitude at the same strain rate. In addition, the difference in ultimate tensile stress ( $\sigma_{UTS}$ ) between the  $t = 1.8\text{mm}$  and  $t = 4.0\text{mm}$  specimens was relatively small compared to the significant difference observed in  $\sigma_{UCS}$ . Furthermore, in the compression tests, the  $t = 4.0\text{mm}$  specimen demonstrated higher strength values across all FO when compared to the  $t = 1.8\text{mm}$  specimen. This observation leads to the conclusion that the mechanical properties of the SFRP are considerably influenced by the matrix properties, particularly in the compressive state. Such distinctions highlight the importance of understanding and considering the matrix material behaviour in the overall mechanical response of SFRP under different loading conditions.

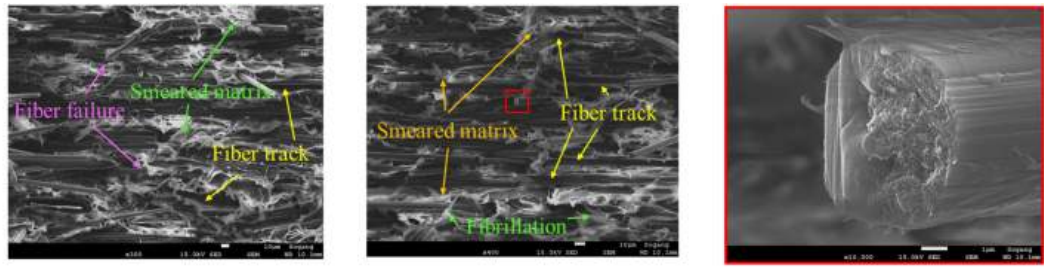
The results were subsequently analysed in detail through scanning electron microscope (SEM) image examination of the fracture surfaces of the compressive specimens, illustrated in Figure 10. In the case of the  $\theta = 0^\circ$  compressive specimen, the buckling of fibres was found to promote fibre breakage, accompanied by the occurrence of fibrillation induced by strong shear ductile damage. For both  $\theta = 45^\circ$  and  $90^\circ$  orientations, the presence of fibre tracks, smeared matrix near the fibres, and frequent fibrillation were observed. In specific, at  $\theta = 90^\circ$ , fibre failure was more prevalent compared to  $\theta = 45^\circ$ , while in the case of  $\theta = 45^\circ$ , greater matrix deformation was seen. These findings substantiate the observation that  $\sigma_{UCS}$  for  $\theta = 90^\circ$  is higher than  $\sigma_{UCS}$  for  $\theta = 45^\circ$ .



(a)  $\theta = 0^\circ$



(b)  $\theta = 90^\circ$



(c)  $\theta = 45^\circ$

**Figure 10:** SEM fracture mechanism observed for compressive specimens: (left) magnification:  $\times 200$ , scale:  $100\mu\text{m}$ , (middle) magnification:  $\times 350$ , scale:  $10\mu\text{m}$ , (right) magnification:  $\times 10,000$ , scale:  $1\mu\text{m}$  [5].

## 2.3 Fracture Toughness and Impact Behaviour

The critical strain energy release rate, also known as fracture toughness, is an important parameter to be considered when analysing the failure criteria of SFRP materials. The complexity of fracture failure is exaggerated due to their anisotropic properties and the presence of micro-scale stress concentration [38].

### 2.3.1 Methodologies for Measuring Fracture Toughness in SFRPs

The assessment of fracture toughness in SFRPs is complex and has been conducted through various approaches, such as single-edge notch (SEN) three-point bending tests [39–41], SEN impact tests [42, 43], single-edge notched tension (SENT) tests [44], Charpy tests [45–47], and Compact Tension (CT) tests [48–53]. They typically focus on measuring the initiation, peak load, or average values of fracture toughness. However, relying solely on initiation values can lead to an underestimation of the material's damage tolerance, resulting in over-designed components.

Understanding the full crack growth resistance curve (R-curve), which characterises how the fracture surface changes as a crack propagates, is crucial for gaining insights into both initiation and propagation values of fracture toughness. Notably, the propagation value is often significantly higher than the initiation value. To obtain the full R-curve, previous literature [52–54] has shown success in utilising CT tests in characterising full R-curves for continuous and discontinuous fibre-reinforced composites.

Two data reduction methods are commonly used to derive the full R-curve from CT tests, the FE-based compliance calibration method [52] and the proposed DIC-based J-integral method [55]. Fujita et al. [4] conducted comparisons between the two experimental reduction methods using PA66-GF50, with the fracture toughness comparisons shown in Figure 11.

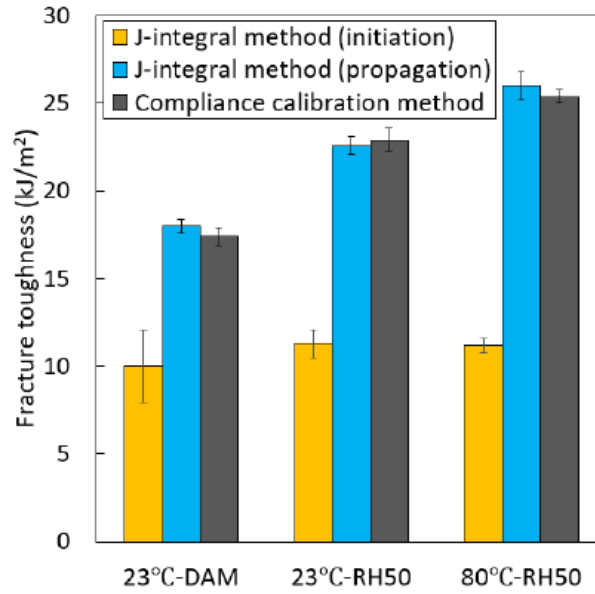


**Figure 11:** Initiation and propagation fracture toughness of 0° FO specimens calculated using the compliance calibration and J-integral methods. Error bars represent one standard deviation [4].

Although results demonstrated that both methods delivered consistent and accurate values for the propagation toughness, the compliance calibration method could not capture the initiation fracture toughness accurately. R-curves were repeatable amongst nominally-identical specimens for both methods. Moreover, solely the initiation fracture toughness was shown to be sufficient to predict the maximum load in the CT specimen. However, the propagation fracture toughness of the SFRPs was at least 80% higher than the initiation. This highlights the criticality of considering both initiation and propagation fracture toughness in Phase 1 of this study, accounting for the damage-tolerance and energy-absorbing mechanisms.

### 2.3.2 Numerical Implications of the Fracture Toughness

To substantiate the reliability of the fracture toughness values obtained from CT tests as well as to investigate its compatibility with FEA, Fujita et al. [4] incorporate these experimentally-measured values into CZM in the FE model replicating the CT test. Figure 12 illustrates the experimental load-displacement curves from the CT tests compared with those generated by the FE simulations. These simulations utilised three cohesive laws, a bilinear law using either (i) the initiation toughness or (ii) the propagation toughness, and (iii) a trilinear law calibrated with the experimental R-curves from the J-integral method.

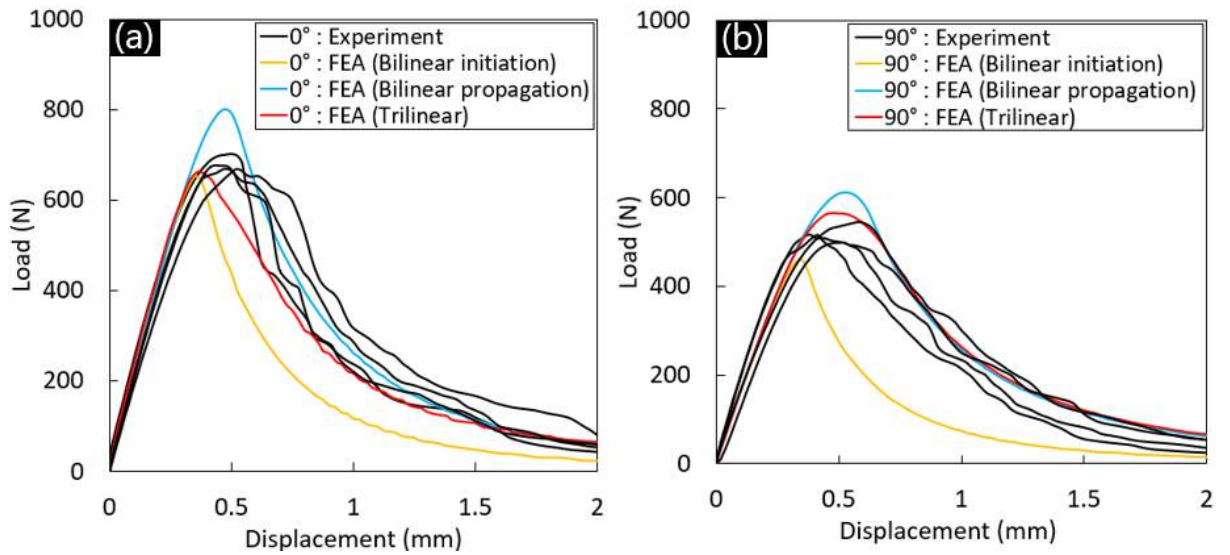


**Figure 12:** Load-displacement curves of CT specimens under 23°C-DAM conditions, comparing results from the experimental tests and FE simulation using bilinear and trilinear cohesive laws, for two machining angles: (a) 0° and (b) 90° [4].

The results demonstrated high compatibility between the experimentally obtained fracture toughness with CZM. Moreover, solely relying on the initiation fracture toughness was adequate for predicting the maximum load in the CT specimens. This insight particularly influences Phase 2 of this study for characterising the failure load. Thus, merely employing the initiation fracture toughness could be sufficient. Furthermore, the propagation fracture toughness must be considered to accurately forecast the energy mechanism during fracture, which is likely the governing design criterion for structures focusing on energy absorption, such as those in automotive applications.

## 2.4 Failure Prediction and Cohesive Zone Modelling

CZM is employed on mesh elements to integrate the failure properties of the material. Cohesive elements are typically only applied to a small section of mesh elements that have the most likelihood of failure initiation, which in turn reduces computational power. Dugdale [56] and Barenblatt [57] were the pioneers in the modelling of the process zone ahead of tip initiation, growth of macrocracks, and coalescence of microcracks simple traction-separation law. As opposed to fracture mechanics, cohesive zone models consider fracture as a gradual process where material separation occurs along an extended crack tip or cohesive zone that is opposed by cohesive tractions. Damage ahead of a crack tip is represented by a decrease in these cohesive tractions, reaching zero at the crack tip leading to a gradual softening behaviour.

### 2.4.1 Bi-linear Traction-Separation Law

The Traction-Separation Law has been investigated in various formulations, including bi-linear [58], tri-linear [33], linear-parabolic [59], linear-cubic [60], linear-exponential [61], exponential [62], and trapezoidal [63, 64]. Regardless of its specific form, the fundamental premise of the



Traction-Separation Law ensures that the total work per unit area of the element is equal to the experimentally derived critical fracture energy ( $G^C$ ) when the element is fully damaged [65].

This research primarily utilises the bi-linear Traction-Separation Law. The bi-linear model is commonly used for capturing the essential mechanical behavior while its simplicity offers efficient numerical implementation. In the bi-linear form, the elastic segment of the Traction-Separation Law is assumed to be linear, complemented by linear softening to govern the damage propagation process. The complete cohesive interface response is depicted in Figure 13. The relation between traction stress and separation is given as Equation 2.

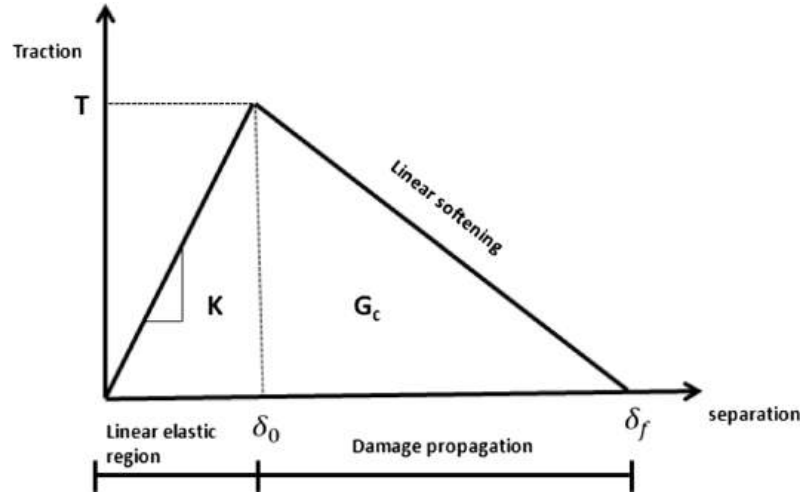


**Figure 13:** Typical traction separation behaviour when a fibre is pulled out from the matrix [6].

$$\begin{Bmatrix} T_n \\ T_s \\ T_t \end{Bmatrix} = \begin{bmatrix} K_{nn} & K_{ns} & K_{nt} \\ K_{ns} & K_{ss} & K_{st} \\ K_{nt} & K_{st} & K_{tt} \end{bmatrix} \begin{Bmatrix} \delta_n \\ \delta_s \\ \delta_t \end{Bmatrix} = [K] \delta \quad (2)$$

Where  $T_n, T_s$  and  $T_t$  are the traction stress in the normal (Mode I), first and second shear (Mode II, III) directions,  $[K]$  is the normal stiffness matrix,  $\delta$  is the displacement in the corresponding directions.

#### 2.4.2 Damage Initiation

Damage initiation refers to the beginning of degradation of the response of a material point. The process of degradation begins when the stresses and/or strains satisfy the chosen damage initiation criteria. Several damage initiation criteria are available, such as the maximum nominal stress, maximum nominal strain, quadratic nominal stress and quadratic nominal strain. This research utilises the maximum nominal stress (in Phase 2) and the quadratic nominal stress criterion (in Phase 1).



### Maximum Nominal Stress Criterion :

Damage is assumed to initiate when the maximum nominal stress ratio reaches 1, expressed in Equation 3.

$$\max \left\{ \frac{T_n}{T_n^0}, \frac{T_s}{T_s^0}, \frac{T_t}{T_t^0} \right\} = 1 \quad (3)$$

where  $T_n^0$ ,  $T_s^0$  and  $T_t^0$  denote the peak values of the nominal stress in Mode I, II and III.

### Quadratic Nominal Stress Criterion :

Damage is assumed to initiate when a quadratic interaction function involving the nominal stress ratio reaches 1, expressed in Equation 4.

$$\left\{ \frac{T_n}{T_n^0} \right\}^2 + \left\{ \frac{T_s}{T_s^0} \right\}^2 + \left\{ \frac{T_t}{T_t^0} \right\}^2 = 1 \quad (4)$$

#### 2.4.3 Damage Evolution

The damage evolution law describes the rate at which the material stiffness is degraded once the corresponding initiation criterion is reached. Damage evolution integrated in CZM can be defined as displacement-based or energy-based. For Phase 2 of this study, the energy-based mode-independent damage evolution approach was employed, while Phase 1 utilised the power law criterion. The power law criterion states that failure under mixed-mode conditions is governed by a power law interaction of the energies required to induce failure in the individual modes (normal, first and second shear directions). This interaction effectively quantifies the area  $G^C$  under the curve following  $\delta_0$  in Figure 13. The mathematical relationship is expressed as Equation 5.

$$\left\{ \frac{G_n}{G_n^C} \right\}^\alpha + \left\{ \frac{G_s}{G_s^C} \right\}^\alpha + \left\{ \frac{G_t}{G_t^C} \right\}^\alpha = 1 \quad (5)$$

Where  $G_n$ ,  $G_s$  and  $G_t$  are the fracture energy in the normal (Mode I), first and second shear (Mode II, III) directions. In the case of mixed-mode loading, the critical fracture energy is defined by Equation 6.

$$G^C = G_n + G_s + G_t \quad (6)$$

## 2.5 Existing Virtual Testing Methodology

There have been extensive research studies [3, 8, 12–18] on the numerical investigation of the mechanical response of IM-SFRPs. Many of them conducted a coupled structural simulation software by means of FEA with the injection moulding process simulation. An example workflow is illustrated in Figure 14.

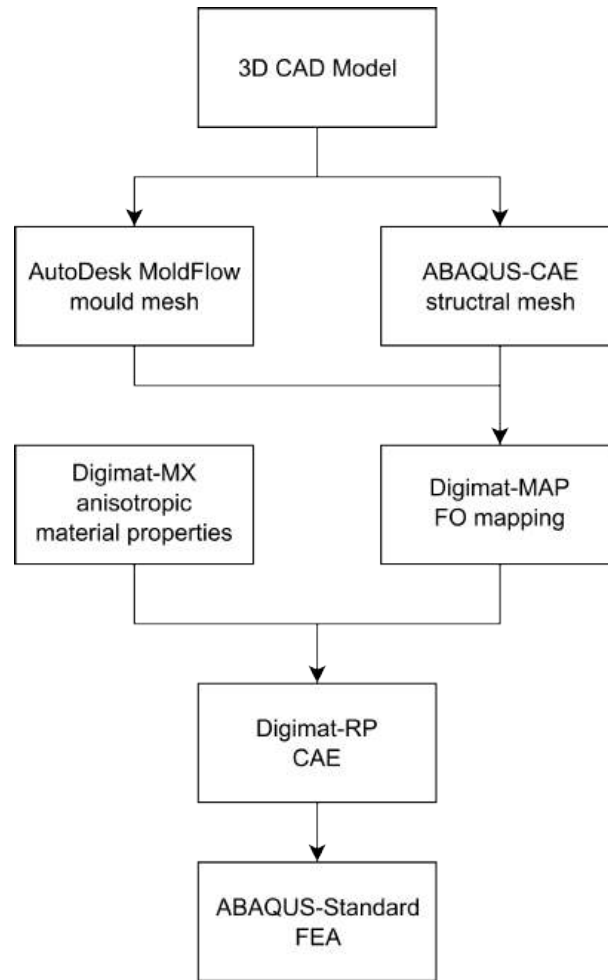


**Figure 14:** Flowchart of the direct transfer of the Moldflow simulation data to Abaqus analysis.

### 2.5.1 Manufacture Processing

The modelling procedure starts with the simulation of the injection-moulding process to define the material's FOD. The injection rate, number and location of the injection gates are defined as input at this stage. This prediction is done through a second-order orientation tensor using the Folgar-Tucker fibre orientation model [66]. This tensor is based on a probability distribution function [67], and represents the probability of fibre alignment along a specific direction. This method was proven to be accurate in several studies [68, 69].

### 2.5.2 Structure FEA Mapping

An identical structural mesh is first generated in the structural simulation software. Obtained orientation tensor results are then mapped into the mesh, popularly via the interfacial software, Digimat-MAP. During the mapping process of the FO, it is also required to input the material properties to the FEA solver. The material properties can be obtained by the prediction model offered by the inbuilt Digimat-MX package, namely the Mori-Tanaka (M-T) mean-field homogenisation theory [70]. This process consists of a two-step homogenisation method. First, each element in the mesh is divided into several 'grains' or packages with similar FO.

Subsequently, the M-T model is applied to calculate homogeneous material properties for each 'grain', where the local property of each element is obtained. However, this method is known to have a small error between generated tensile properties to experimental data [8, 18]. Therefore, calibrations of the model by applying true elasto-plastic properties can be done to increase prediction accuracies.

### **2.5.3 Coupled Simulations**

Once the orientation tensor with the inbuilt mesh element-based mechanical properties has been created and set up correctly in the FEA, boundary conditions are defined, and the coupled simulation is run by the Digimat-RP interface.

Coupled manufacturing processes and structural simulations have proven to be accurate and effective in estimating the mechanical properties of simple geometry SFRPs [8, 16–19]. Numerical investigations conducted in this research will therefore apply the same procedure illustrated in Figure 14.

### 3 Phase 1 - Investigation of the Failure of SFRP under Multi-axial Stress State

#### 3.1 Methodology

The FEM software ABAQUS is utilised to generate a single fibre matrix Representative Volume Element (RVE) under uniaxial, equi-biaxial and equi-triaxial strains. This process involves creating a geometry model, specifying boundary conditions, selecting a material model, creating a mesh and choosing an element type.

##### 3.1.1 Geometry of the Finite Element Model

The dimensions of the fibre were determined based on the data provided by Asahi Kasei. The diameter of the fibre  $2r$  was set at  $10\text{ }\mu\text{m}$ , and the length  $l_f$  was set to  $200\text{ }\mu\text{m}$ , as shown in Figure 15(a), 15(b). The polymer matrix surrounding the fibre was modelled as a cuboid. This approach enables the duplication of the single fibre matrix RVE and facilitates the application of multi-axial loading and sidewall constraints. To model discontinuous fibre, layers of matrices were created along the z-direction, the front and back of the fibre cross-section. The matrix thickness in the axial and transverse directions was initially defined as the variable  $t$ . The composite material, GF50-PA66, comprised an E-glass mass fraction of  $m_f = 50\%$  with a density of  $\rho_f = 2.540\text{ kg/m}^3$  and PA66 polymer with a mass fraction of  $m_m = 50\%$  and a density of  $\rho_m = 0.4367\text{ kg/m}^3$ . The volume fraction of the fibre  $V_f$  and the matrix  $V_m$  were calculated in Equation 7.

$$\begin{aligned}
 V_f : V_m & \quad (7) \\
 &= \frac{m_f}{\rho_f} : \frac{m_m}{\rho_m} \\
 &= \frac{1}{2.540} : \frac{1}{1.145} \\
 &= 0.1969 : 0.4367 \\
 V_f &= 31.08\% \quad V_m = 69.92\%
 \end{aligned}$$

Subsequently, the value of  $t$  was calculated in Equation 8.

$$\begin{aligned}
 V_f &= \frac{\pi r^2 l_f}{(2r + 2t)^2 (l_f + 2t)} \quad (8) \\
 0.3108 &= \frac{\pi (5)^2 (200)}{(2(5) + 2t)^2 (200 + 2t)}
 \end{aligned}$$

$$t_1 = -99.289\mu\text{m} \text{ (rejected)}, \quad t_2 = 2.8382\mu\text{m}, \quad t_3 = -13.549\mu\text{m} \text{ (rejected)}$$

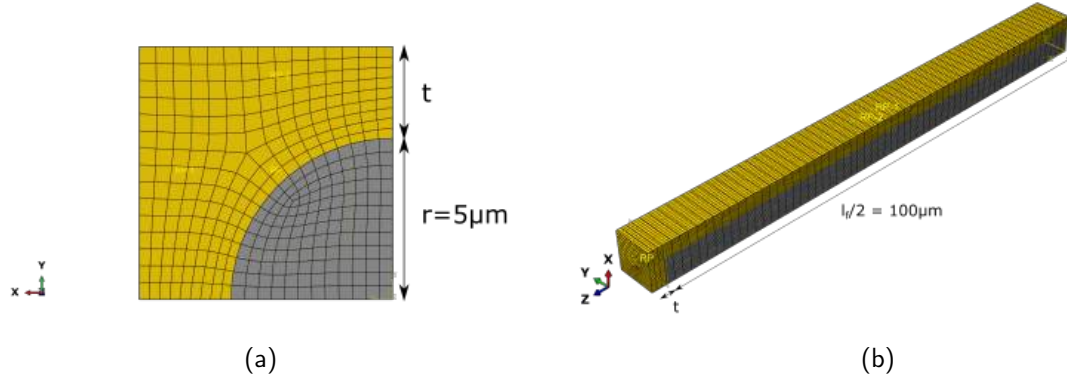


**Figure 15:** Single fibre matrix RVE geometry.

3D 8-node brick elements with reduced integration and hourglass control element (C3D8R) are used for both the fibre and the matrix. Previous studies [71–73] have shown this type of mesh element provides good accuracy at integration points for a low computational cost.

### 3.1.2 Boundary Condition

To simulate uniaxial, biaxial and triaxial loading conditions, reference nodes with tie constraints were first introduced at the centre of each loading surface, as shown in Figure 16. This allows the total reaction force of the loaded surface to be easily extracted during post-processing. Subsequently, displacements were applied to the reference nodes in the direction perpendicular to the loading surface. In the biaxial loading case, the transverse displacement was applied in a 1:1 strain ratio to the longitudinal displacement. Whereas, in the triaxial loading case, displacements were applied following a 1:-2:1 ratio, effectively emulating the loading conditions observed in the puncture test conducted by Y. Fujita [4], as seen in Figure 7(a).

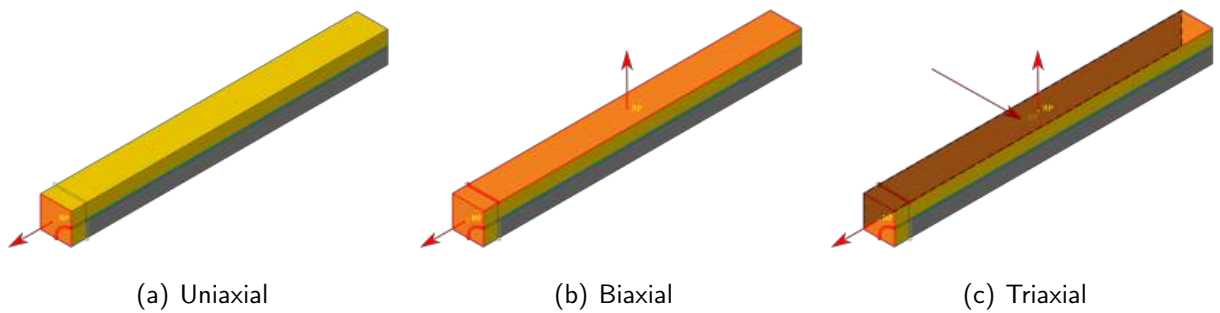


**Figure 16:** Loading boundary conditions.

Moreover, displacement constraints were imposed on the non-symmetrical surfaces (i.e. the exposed surfaces) to ensure a flat surface throughout the loading process. Symmetry boundary conditions were enforced on the inward-facing surfaces. This approach facilitated the replication of single fibre elements into multiple fibre elements, enabling the emulation of macro-scale SFRPs.

### 3.1.3 Material Properties without Failure Criteria

The FE model analysis was developed progressively with an increasing level of material complexity. Preliminary analyses were initially conducted with isotropic material properties, without including any plasticity or failure criteria under uniaxial loading. Isotropic linear-elastic material properties for E-glass and PA66 are presented in Table 2.

**Table 2:** Isotropic material properties of E-glass fibre and PA66 epoxy matrix.

Material	Young's Modulus (GPa)	Poisson Ratio (-)
E-glass fibre	72	0.22
PA66	3	0.35

Following the preliminary analysis, plasticity was introduced into the model. The simulation results of isotropic material properties without plasticity confirmed that the E-glass fibre did not exceed its yield strength of 3400 MPa under the maximum applied strain of 0.2. As a result, it is unlikely to exhibit plastic behaviour in this simulation. Consequently, only the PA66 material property was updated with the plastic strain data. The true stress-strain data from the Asahi Kasei database was used to obtain the plastic strain of PA66, with the elastic strain region being subtracted. Figure 17 illustrates the elastic and plastic regions, indicated by the portions before and after the yield point (point of plastic onset), respectively.

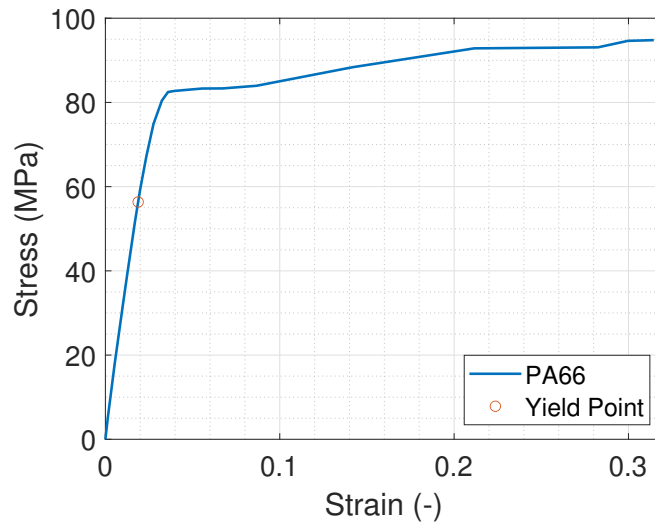


**Figure 17:** True stress-strain curve of PA66 [7].

### 3.1.4 Introduction of Cohesive Elements

The interfacial region between a fibre and its surrounding matrix is a critical component in facilitating stress transfer from the matrix to the fibre. This region, characterised by its flexibility, is capable of withstanding increasing amounts of shear stress under applied loading conditions until a maximum threshold is reached, known as the interfacial shear strength (IFSS) [74]. The behaviour of this interface can be modelled by Cohesive Elements (CE), with its material

behaviour defined by the traction-separation law, as previously outlined in the work of Camanho et al [75].

With consideration of the injection-moulding process, the adhesive material is sprayed onto the fibre which infuses with the thermoplastic. This interface layer was modelled as part of the volume of the PA66 matrix surrounding the circular fibre with a thickness of  $0.05 \mu\text{m}$ . The geometry of the CE is shown in Figure 18. The interfacial elements were discretised with 8-noded COH3D8 cohesive elements.

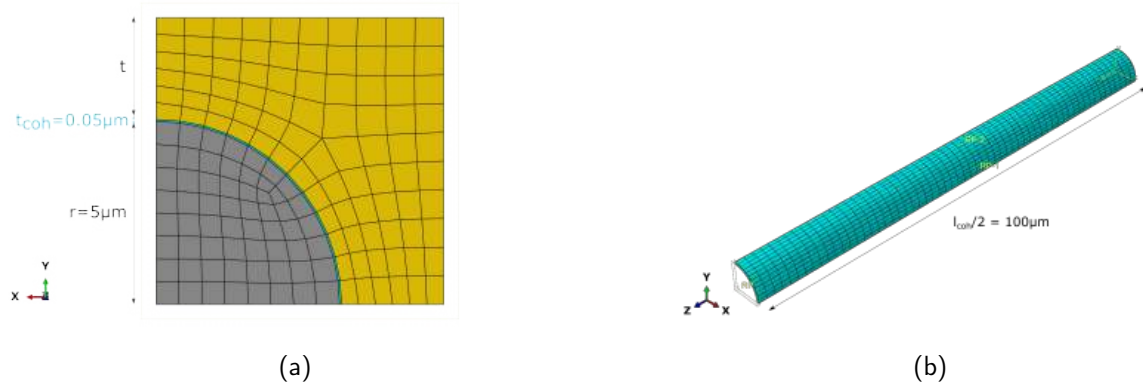


**Figure 18:** Geometry of the single fibre matrix RVE model with CZM.

Moreover, the contact region of  $0.5 \mu\text{m}$  between the fibre cross-section and the matrix was substituted with an empty gap without any elements, as shown in Figure 19. This decision was based on two fundamental factors. Firstly, this region was observed to reach the critical fracture energy in the early stages of the simulation, leading to an early termination of the simulation before reaching the experimental failure strain. Secondly, during the manufacturing process, the cross-section of the fibre is poorly coated with adhesive material. Consequently, removing the elements from this location provides a more realistic representation of the micro-scale SFRPs.

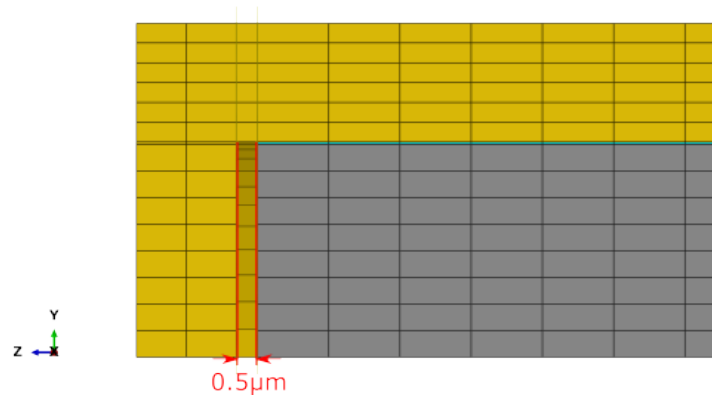


**Figure 19:** Bad adhesion region represented by an empty gap.

Regarding the failure mechanism of CE, the quadratic nominal stress criterion was adopted as the governing factor for damage initiation, while the damage evolution was modelled using the

2nd order power-law. The power-law damage evolution method incorporates the critical energy dissipated, denoted as  $G^C$ , prior to complete failure. The 2nd order exponent was selected to ensure a balanced representation of the cohesive behaviour across different scenarios. The power-law interaction between the energies required to induce failure in the Mode I, II and III directions is described in Equation 9.

$$\left\{ \frac{G_n}{G_n^C} \right\}^2 + \left\{ \frac{G_s}{G_s^C} \right\}^2 + \left\{ \frac{G_t}{G_t^C} \right\}^2 = 1 \quad (9)$$

The failure properties of the CE used to emulate the GF50 and PA66 interface are shown in Table 3.

**Table 3:** Failure traction stress and fracture energy for CE.

Failure parameter	Value	Author's Comment
Normal Traction Stress, $T_n$	94.6 MPa [4]	$T_n$ was obtained experimentally, and therefore this is a reliable parameter.
First direction Shear Traction Stress, $T_s$	20 MPa [76]	$T_s$ was obtained from past literature. However, the fibre diameter of 10 $\mu\text{m}$ required extrapolation. A parametric study conducted on $T_s$ is essential to determine its sensitivity to the results.
Second direction Shear Traction Stress, $T_t$	20 MPa [76]	$T_t$ was assumed to be identical to $T_s$ . Similar to $T_s$ , a parametric study conducted on $T_t$ is essential to determine its sensitivity to the results.
Normal Critical Fracture Energy, $G_n^C$	5.33 kJ/m <sup>2</sup> [48]	$G_n^C$ was calculated from the fracture toughness obtained from past literature and Young's Modulus of PA66. The literature parameters used were directly dedicated to the interfacial material property. Therefore, this is a reliable parameter.
First direction Critical Fracture Energy, $G_s^C$	5.33 kJ/m <sup>2</sup> [48]	$G_s^C$ was assumed to be identical to $G_n^C$ . However, shear fracture energy is a significant parameter employed in this study to examine the dissipation of damage energy when the interfacial property experiences shear loading. A parametric study conducted on $G_s$ is essential to determine its sensitivity to the results.
Second direction Critical Fracture Energy, $G_t^C$	5.33 kJ/m <sup>2</sup> [48]	$G_t^C$ was assumed to be identical to $G_s^C$ . Similar to $G_s^C$ , a parametric study conducted on $G_t^C$ is essential to determine its sensitivity to the results.



### 3.1.5 Mesh Convergence Study

To accurately capture the growth of damage, a sufficient mesh density is necessary. Therefore, this mesh convergence study was conducted by developing five FE models with varying numbers of mesh elements ranging from approximately 1000 to 57000. The parameter utilised to govern the convergence is the composite critical total strain, denoting the point at which 0.3 equivalent plastic strain in the matrix is attained. This strain was considered as the true point of failure because experimental data from tensile tests [4] indicated that specimens with fibre orientation aligned with the loading direction failed at this strain. The effect of the mesh refinements is illustrated in Figure 20, indicating that a stable result is achieved with around 12300 elements. Further refinement of the mesh grid has a negligible impact on the accuracy of the simulation. To compromise between computational cost and simulation accuracy, the model with 12300 mesh elements was employed for all the simulation results presented in phase 1 of this paper.

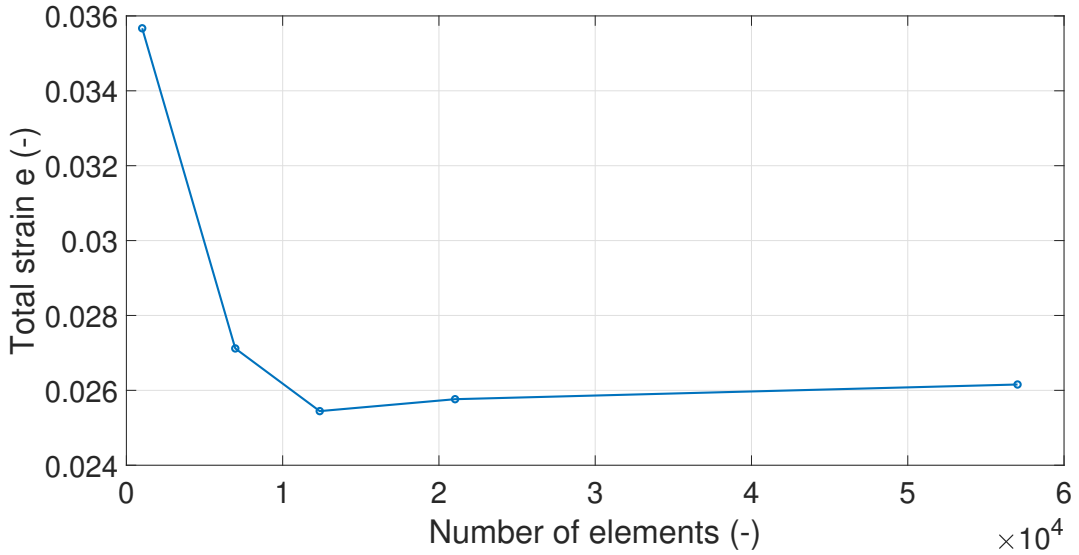


Figure 20: Mesh convergence study on 0.3 PEEQ.

## 3.2 Results

### 3.2.1 Effect of Cohesive Elements

The Plastic Strain (PE) of the single fibre matrix RVE was first analysed in two uniaxial loading simulations, one without CE shown in Figure 21(a) and the other with CE implemented to model the interface between the fibre and matrix shown in Figure 21(b). The simulation frames shown are both at the composite strain  $e = 0.02$ . It was observed that the model without CE exhibited significant distortion, particularly in the interface. This shear distortion was attributed to the absence of failure features indicating the damage initiation stress had been exceeded. Furthermore, the model without CE does not characterise failure. Loads exceeding the input material stress-strain curve are extrapolated.

In contrast, the model with CE implemented successfully captured the interfacial adhesion failure. The model aborted at  $e = 0.032$  when the stiffness degradation reached 1, and CE began to vanish. This demonstrates the importance of CE in accurately modelling real-life failure phenomena. Consequently, the following results will primarily focus on the simulations with CE implemented.

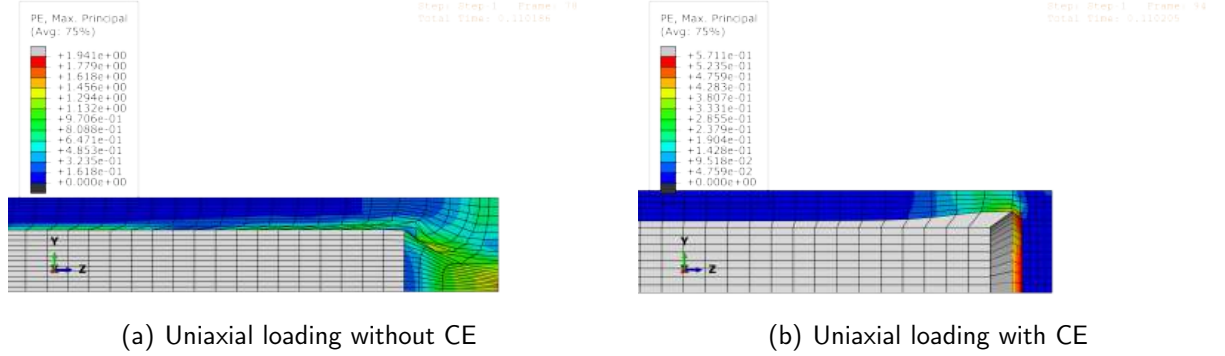


**Figure 21:** Plastic Strain at total strain  $e = 0.02$ .

### 3.2.2 Effect of the Geometrical Gap

In the FE model geometry mentioned in Section 3.1.4, solid elements between the fibre cross-section and the matrix were substituted with an empty gap in order to avoid early simulation abortion. The effect of this gap is further explored here in uniaxial loading conditions. Firstly, an FE model excluding the gap was considered and compared with the FE model with the empty gap. These models were subsequently compared in relation to a tensile experiment performed on the FO tensor  $a_{11}=0.9$  specimen as well as the Halpin-Tsai model in Equations A.1 and A.2 in Appendix A.1. The stress-strain curves' comparison is depicted in Figure 22. Notably, the FE model with an empty gap exhibited an underestimation of Young's modulus for the PA66-GF50 aligned fibre condition, reporting a simulation value of 15.01 GPa, which deviates from both the experimentally-measured 19.08 GPa and the Halpin-Tsai model's prediction of 20.10 GPa. Conversely, the FE model without the gap displayed a more accurate prediction, approximating the material's Young's modulus at 20.01 GPa. However, this improvement in accuracy is accompanied by the drawback of early simulation abortion due to divergence.

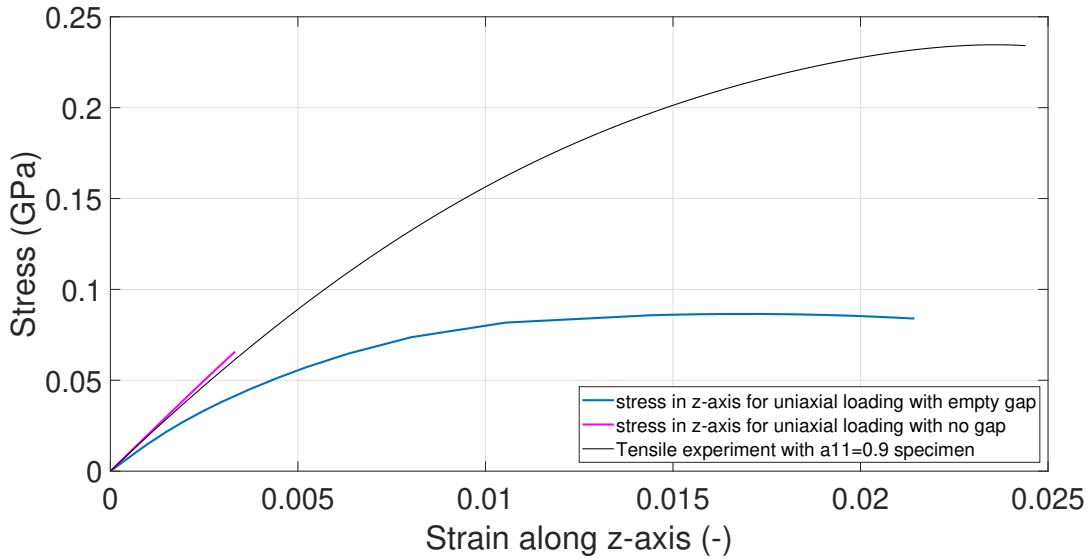


**Figure 22:** Comparison of Stress-Strain Curves: FE Model with gap vs. FE Model without gap, in relation to experimental test curve for FO tensor  $a_{11}=0.9$ .

To alleviate simulation divergence, a stabilisation scheme involving damping factor control based on dissipated energy fraction was introduced to the FE model without the gap. Specifically, a damping energy fraction of 0.0002 was incorporated, notably greater than typical values. The impact of this damping stabilisation is illustrated in Figure 23. An artificial increase in the modulus was observed due to the effect of damping. Despite these efforts, the model continued to struggle with convergence.

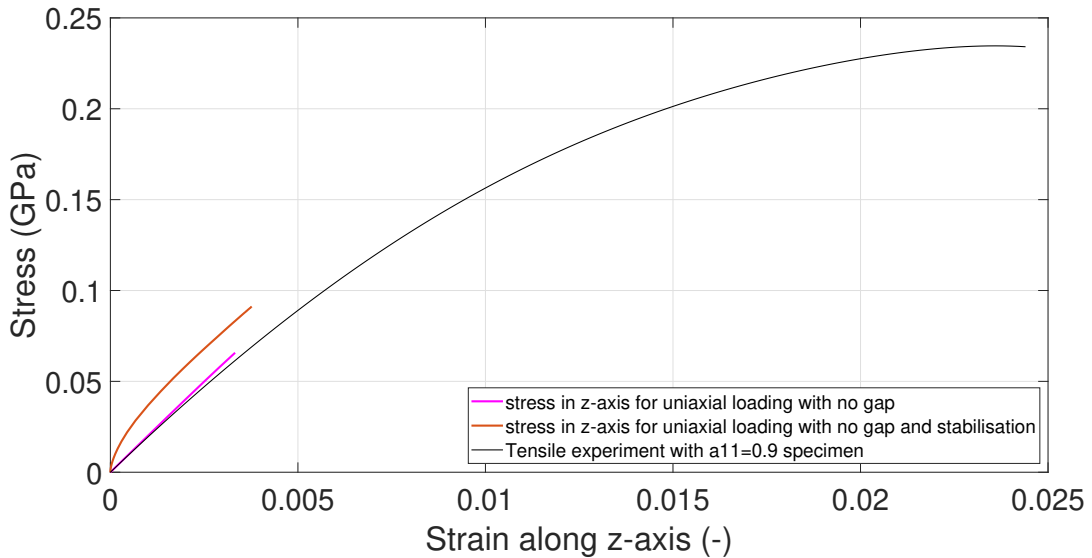


**Figure 23:** Comparison of Stress-Strain Curves: FE Model without gap vs. FE Model without gap and with stabilisation, in relation to experimental test curve for FO tensor  $a_{11}=0.9$ .

The analysis of the the FE model without the gap has validated its overall geometry of the RVE FE model was able to accurately represent the aligned fibre conditions. Nonetheless,

to achieve convergence in simulations involving higher strain, the inclusion of the empty gap remains a necessary modification to the FE model.

### 3.2.3 Validation of the Hypothesis

#### Uniaxial, Biaxial and Triaxial Stress-Strain Relation :

In Figure 24, the stress-strain curves for uniaxial loading in the z-direction (longitudinal), biaxial loading in the z-direction (longitudinal) and y-direction (transverse), and triaxial loading in the z-direction (longitudinal) and x, y directions (transverse) are presented. The comparison of the longitudinal and transverse directions in the biaxial and triaxial loadings revealed a significant difference between Young's Modulus values, which were characterised by their gradients. Specifically in the biaxial case, the transverse loading exhibited a Young's Modulus of 7.83 GPa, while the longitudinal direction exhibited a Young's Modulus of 18.55 GPa. This observation can be explained by the difference in the fibre orientation causing a difference in the ratio of fibre and matrix in the direction of loading. Since the PA66 matrix stiffness was significantly lower than that of the glass fibre, it was expected that the transverse direction would exhibit a lower Young's Modulus.

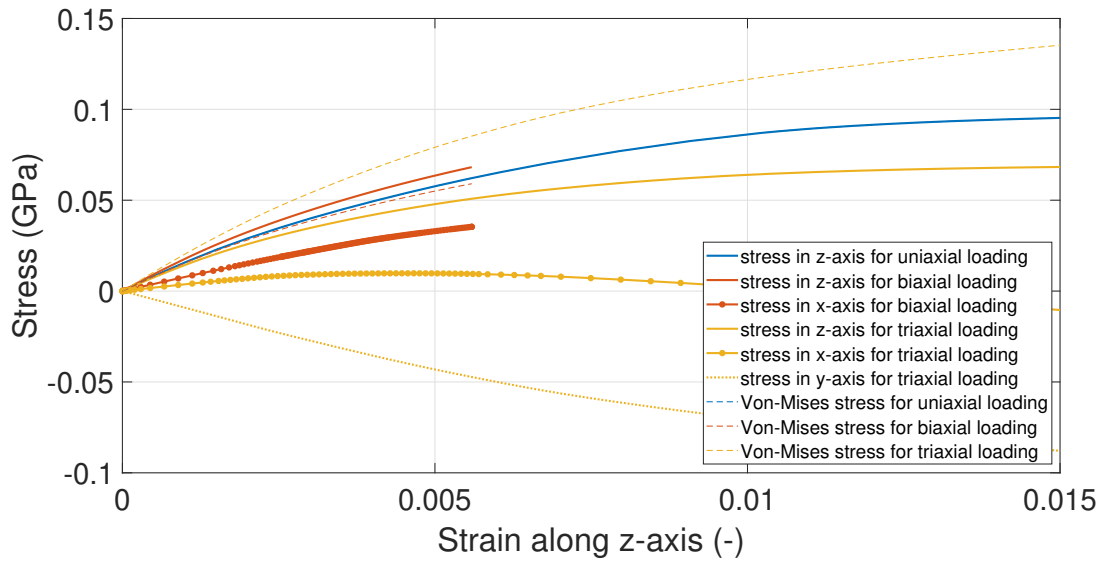


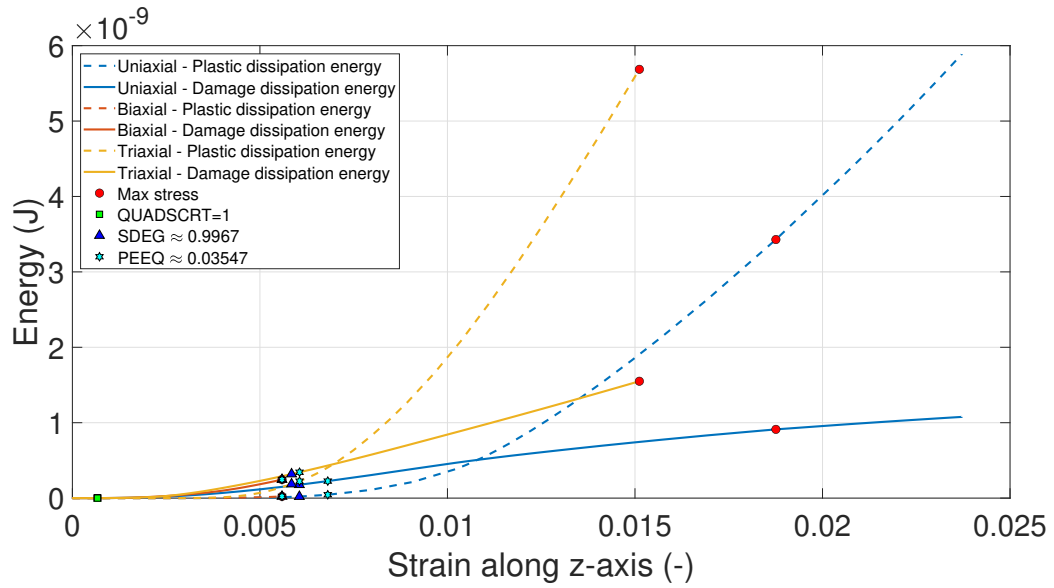
**Figure 24:** Stress-strain curve of longitudinal uniaxial loading (blue), longitudinal biaxial loading (orange) and transverse biaxial loading (yellow).

Moreover, a comparison of the longitudinal direction of uniaxial, biaxial and triaxial loading showed that biaxial loading resulted in the highest Young's Modulus of 18.55 GPa, followed by uniaxial loading of 16.46 GPa and triaxial loading of 15.06 GPa. Poisson effects were the contributing factors behind this. During the loading process, the transverse tensile loading in the biaxial case imposed compressive stress in the longitudinal direction, which opposed the longitudinal loading and effectively reduced the reaction force in the longitudinal direction. This phenomenon enabled the model to be loaded to a higher stress per unit strain, explaining

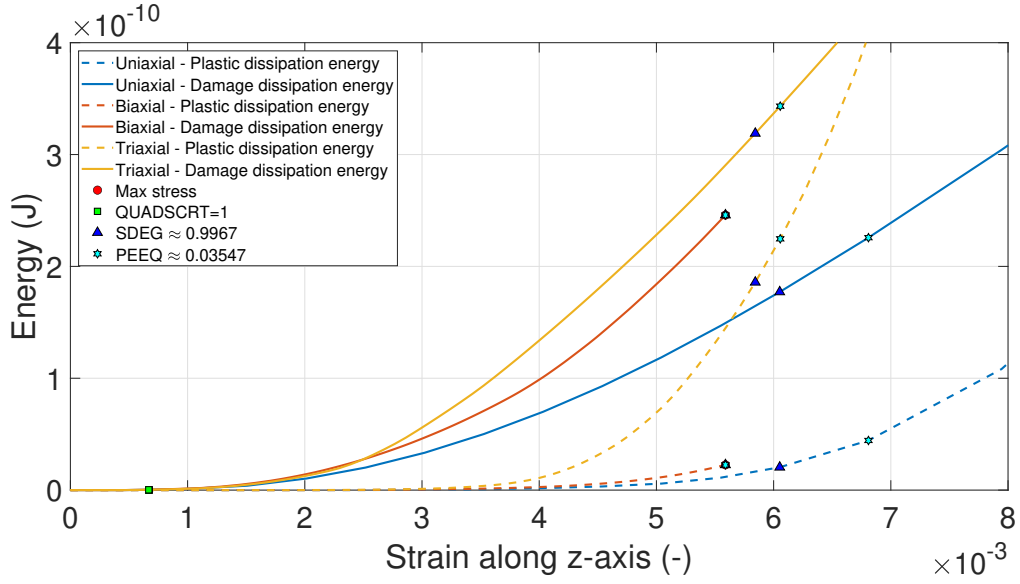
the higher Young's Modulus observed in biaxial loading. On the contrary, the triaxial loading consists of transverse compressive loading in the y-direction that has doubled the strain of its transverse tensile loading in the x-direction, producing an overall tensile stress, and promoting the reaction force in the longitudinal direction.

### Energy Dissipation :

Figure 25 illustrates comparisons of the plastic and damage energy dissipation of the uniaxial, biaxial and triaxial cases during the loading process. The simulation instance at maximum stress, quadratic nominal stress damage (QUADSCRT) = 1, stiffness degradation (SDEG) = 0.9967 and plastic strain equivalent (PEEQ) = 0.03547 were highlighted in each simulation to compare the dissipated energy in equivalent frames. Results show that the SFRPs reached maximum stress and higher PEEQ at a lower total composite strain in the biaxial case than in the uniaxial and triaxial cases. Moreover, the sum of plastic and damage dissipated energy in the triaxial loading is greater than the biaxial loading, followed by the uniaxial loading in all four highlighted instances. This indicates that more unrecoverable energy is used to deform the SFRP in triaxial loading than in biaxial loading and, subsequently, uniaxial loading. This implies the highest fracture toughness and fracture energy is achieved in the triaxial stress state, followed by the biaxial and the uniaxial stress state.



(a)



(b) Zoomed-in.

Figure 25: Energy dissipation of the uniaxial, biaxial, and triaxial loading per unit cell.

### 3.2.4 Parametric Study

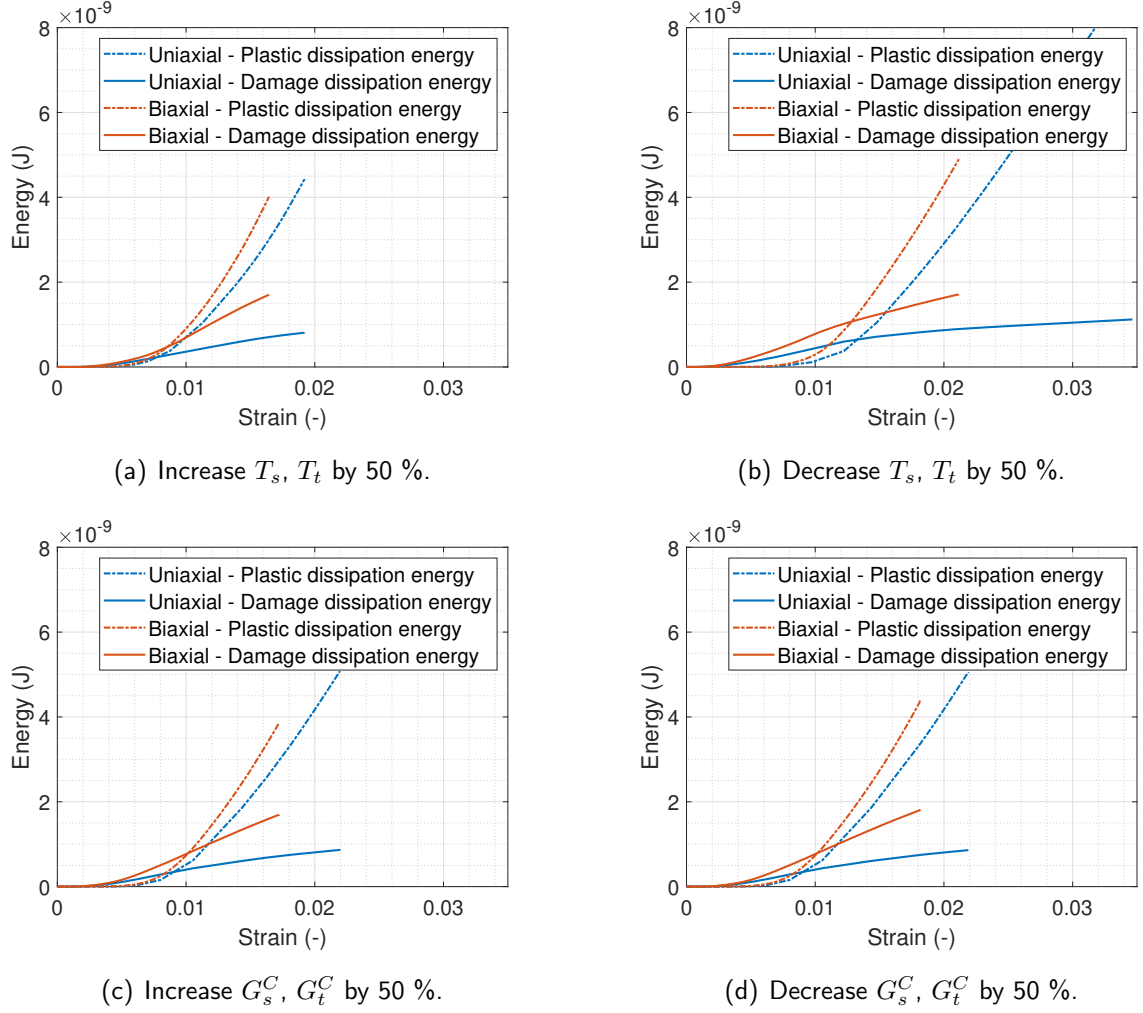
Parametric investigations were undertaken on CE parameters that lacked empirical validation, specifically the Mode II and III traction stresses,  $T_s$  and  $T_t$ , and the Mode II and III critical fracture energies,  $G_s^C$  and  $G_t^C$ . These parameters were systematically varied by  $\pm 50\%$ , representing an approximation of the potential extremities in fibre and matrix interface characteristics. The specific values employed in the experimentation are detailed in Table 4.

Table 4: Parametric study on failure parameters.

CE failure parameters	Value
Original Mode II, III traction stresses, $T_s$ and $T_t$	20 MPa
$T_s$ and $T_t$ +50%	30 MPa
$T_s$ and $T_t$ -50%	10 MPa
Original Mode II, III critical fracture energy, $G_s^C$ and $G_t^C$	5.33 kJ/m <sup>2</sup>
$G_s^C$ and $G_t^C$ +50%	8.00 kJ/m <sup>2</sup>
$G_s^C$ and $G_t^C$ -50%	2.67 kJ/m <sup>2</sup>

The energy dissipation curves in the uniaxial and biaxial loading cases for the parametric study are shown in Figure 26. A discernible difference is shown when comparing the two cases where  $T_s$  and  $T_t$  are varied. Evidently, increasing  $T_s$  and  $T_t$  by 50 % results in increased energy requirements for RVE plastic deformation, while simultaneously absorbing more energy by the CE during the crack initiation process. Furthermore, the biaxial loading case exhibits greater plastic and damage dissipation energies than the uniaxial loading case at any simulation instance across all four parametric study scenarios. This substantiates the finding that the biaxial

stress state yields higher fracture toughness and fracture energy than the uniaxial stress state, regardless of the approximated CE parameters incorporated in this investigation. Given this trend, it is reasonable to speculate that similar outcomes would be observed in the triaxial stress state, therefore, the parametric study concerning the triaxial stress state was deemed unnecessary.



**Figure 26:** Comparative energy dissipation curves for Mode II and III traction stresses ( $T_s, T_t$ ) and critical fracture energies ( $G_s^C, G_t^C$ ) in the parametric study.

### 3.3 Discussion

#### 3.3.1 Criticality of CZM

Phase 1 of this project focuses on the investigation of the energy dissipation mechanisms of SFRP under multi-axial loading. Through the process of modelling the single fibre matrix RVE, the necessity of CZM was demonstrated. The comparison between the model with and without CE revealed that the use of CE is crucial in simulating the failure mechanism of SFRPs, as well as in modelling the behaviour of fibre and matrix interface.

### 3.3.2 Validation of the Hypothesis

The objective of this phase was to investigate the overestimation observed in the puncture test simulations conducted by Y. Fujita [4], based on the hypothesis that the fracture toughness of SFRPs reduces in the multi-axial stress state which caused overestimations of critical failure load. Results of the energy dissipation curves indicate that the single fibre matrix RVE model under a multi-axial stress state exhibits higher plastic and damage dissipation energy than the uniaxial axial stress state. This implies that a greater amount of recoverable energy is absorbed by the material up to matrix failure strain, which results in a higher fracture toughness and energy in the multi-axial stress state.

Although the results demonstrated in this report do not provide a definitive explanation for the overestimation in failure load observed in the puncture test simulations, they do suggest that lower fracture toughness in the multi-axial stress state is not likely to be the reason behind it. These findings highlight the importance of further investigation into the energy dissipation mechanisms of SFRPs under multi-axial loading, which can provide valuable insights for the design and optimisation of SFRPs. The progress made in this phase lays the groundwork for the subsequent phases of this research project, aiming to build upon these results and further advance the understanding and modelling of the behaviour of SFRPs.



## 4 Phase 2 - Simulation of IM-SFRP EM using coupled FEA

### 4.1 Methodology

In this phase of the investigation, an in-depth analysis was carried out on the mechanical response and failure mechanism of EM specimens produced through the use of a single injection port IM-SFRP under the Dry-As-Moulded (DAM) condition at 23°C. To achieve this, a comprehensive approach combining FE simulations and injection-moulding process simulations was employed. Results obtained from these simulations were then compared against the tensile experimental data obtained from the EM specimen conducted by Y. Fujita [4], as shown in Figure 27.

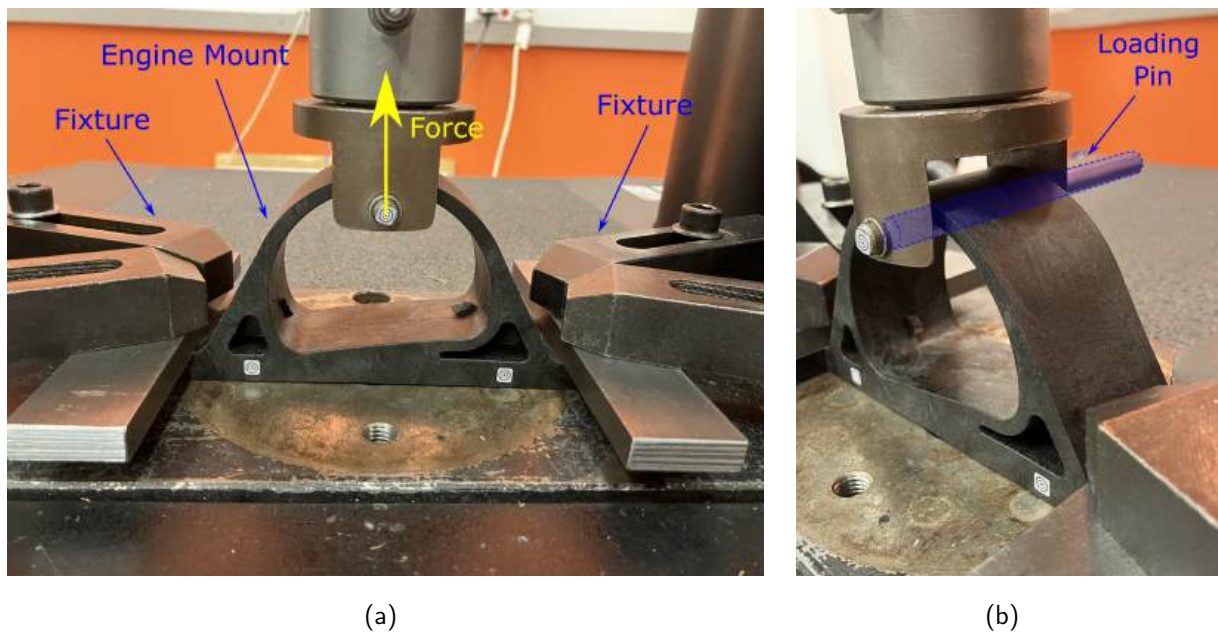


**Figure 27:** Tensile test setup for the IM-SFRP fabricated EM.

#### 4.1.1 Geometry of the Finite Element Model

The workflow of the coupled simulation begins with the creation of the EM geometry, maintaining the same dimensions as the physical EM specimen. Initially, a 2D cross-section of the EM, provided by Asahi Kasei, served as the foundation. Subsequently, this 2D cross-section was extruded to construct a 3D solid component, followed by the addition of intricate details to the geometry, such as the incorporation of two mounting holes on the flat section. The technical drawing showcasing the detailed geometry of the EM is found in Figure 28.

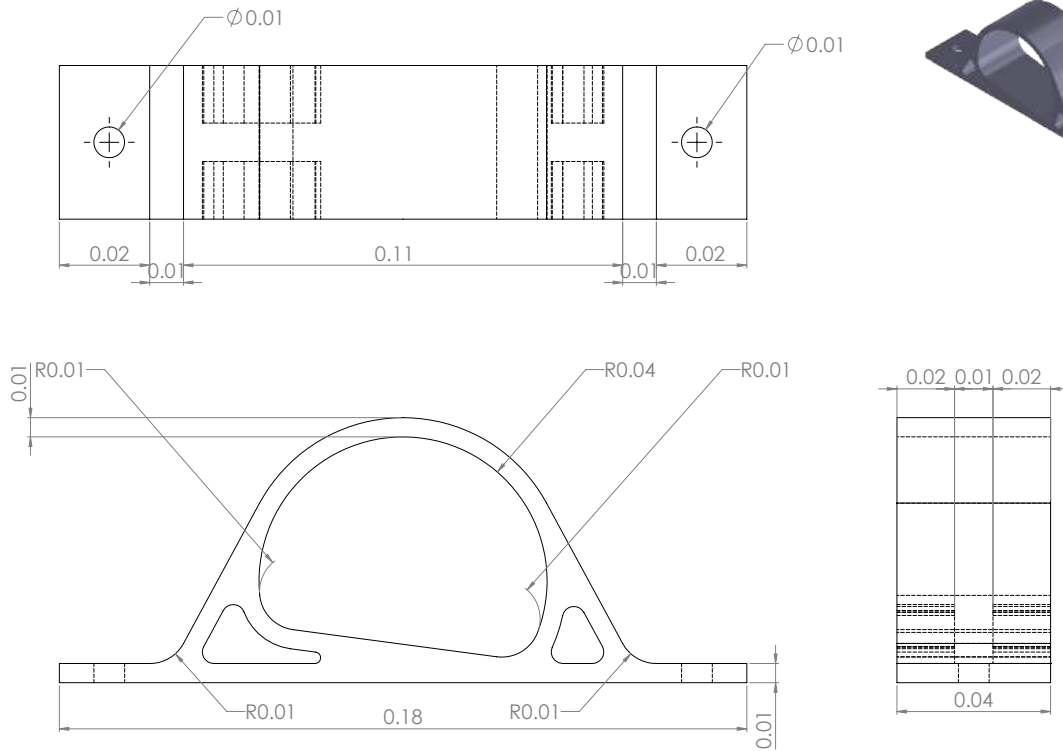


**Figure 28: 3D geometry of the EM.**

#### 4.1.2 Boundary Conditions

In order to enhance simulation efficiency and reduce computational time, five boundary conditions discussed in the following were explored to simplify the EM loading model. Each boundary condition scheme was assigned with isotropic material properties, and the resulting simulation outcomes in the form of load-displacement curves were compared with the baseline model.

##### I. Baseline Model (EM with Legs + Top and Bottom Fixtures + Solid Pin)

The baseline model comprises two top fixtures and a platform, all modelled as analytical flat rigid shells. These rigid shells are grounded (encastred) and in contact with the EM via a viscous friction coefficient of 0.2, effectively simulating the frictional contact between the fixture plates and the testing platform with the EM. This friction coefficient value has been validated to effectively capture the frictional contact between IM-SFRP specimens and the fixtures in prior puncture test simulations [4]. Moreover, to account for the steel loading pin deformation and the subsequent non-uniformly distributed contact interface, the pin was modelled as a solid element cylinder. It is non-conformally in contact with the EM and aligned with the EM's x and y axes centerline, utilising the same friction coefficient of 0.2. Displacement-controlled upward loading (positive z-direction) is applied to the pin, while only

rotations in the x and z axes are constrained to allow for rotation of the pin around the y-axis due to uneven loading. The schematic of the baseline boundary condition, which is also the most complex boundary condition, is shown in Figure 29.

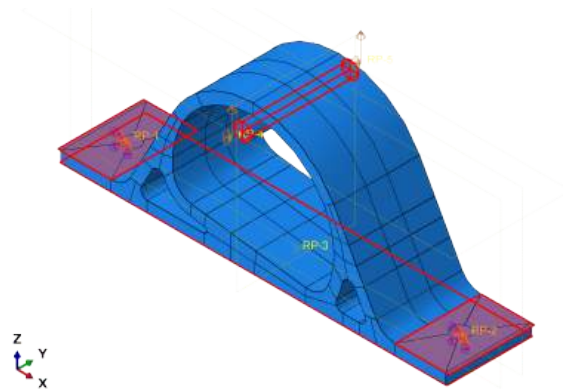


**Figure 29:** Schematic of the baseline FE model.

## **II. Analytical rigid shell pin (EM with Legs + Top and Bottom Fixtures + Analytical Rigid Pin)**

Assuming that the steel pin deformation is negligible compared to the EM deformation due to the much greater Young's modulus of the steel than PA66GF50, the steel loading pin is represented as a cylindrical rigid shell in this boundary condition. This boundary condition reduces computation power by neglecting steel pin deformation. The schematic of the analytical rigid pin boundary condition is shown in Figure 30.

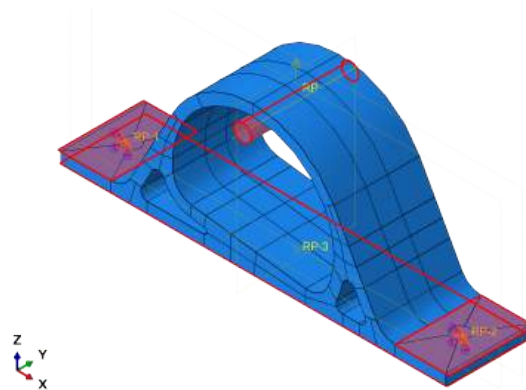


**Figure 30:** Schematic of the 'analytical rigid pin' FE model.

## **III. Bottom Constraint (EM with Legs + Top Fixtures + Solid Pin)**

In this boundary condition scheme, the platform rigid plate is removed, with the bottom surface of the EM fully constrained (encastred). While this simplification effectively disregards any potential sliding and friction between the test platform and the EM, it leads to a noticeable

reduction in computational cost. The schematic of the bottom constraint boundary condition is shown in Figure 31.

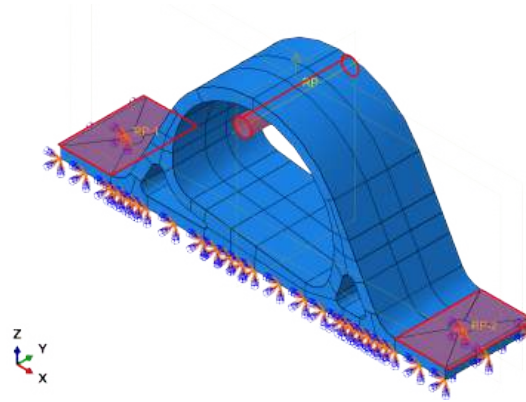


**Figure 31:** Schematic of the 'bottom constraint' FE model.

#### IV. Fixture Constraint (EM with Legs + Bottom Fixture + Solid Pin)

The fixture constraint utilises a similar simplification to the bottom constraint. The two top fixture plates are removed, and the top flat side sections of the EM are fully constrained (encastred), neglecting possible sliding and friction between the top fixture and the EM. The schematic of the fixture boundary condition is shown in Figure 32.

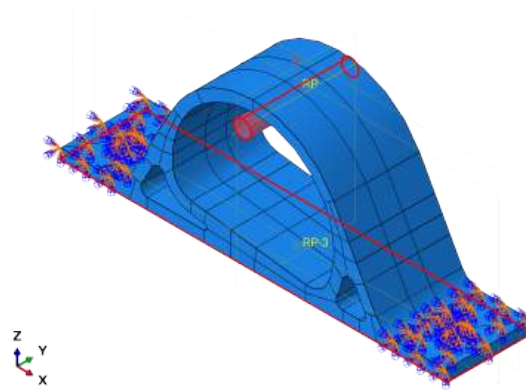


**Figure 32:** Schematic of the 'fixture constraint' FE model.

#### V. Without Legs (EM without Legs + Bottom Fixture + Solid Pin)

One possible solution to reduce computational cost is by removing the legs (two flat side sections) of the EM. Assuming the two flat side sections were tightly clamped in the tensile test, thus no slipping occurs during the test, and they effectively serve as part of the 'wall', which can be removed. The fully constrained condition can instead be implemented on the cut-off surface. The schematic of the model without legs is shown in Figure 33.

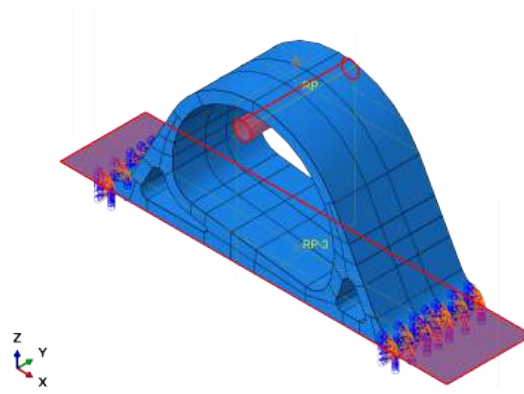


**Figure 33:** Schematic of the 'without legs' FE model.

## **VI. Without Legs with Bottom Constraint (EM without Legs + Solid Pin)**

This boundary condition scheme is a further simplified version of the 'Without Legs' scheme. The platform rigid shell is replaced by the direct full constraint on the bottom surface of the EM. The schematic of this model is shown in Figure 34.

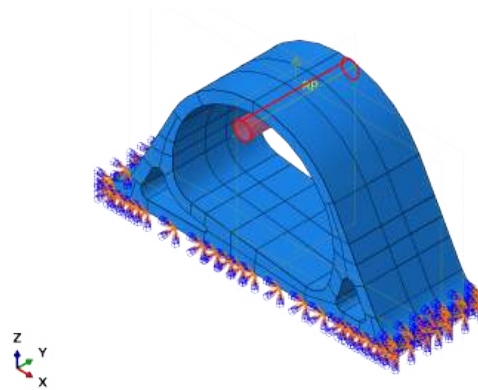


**Figure 34:** Schematic of the 'without legs with bottom constraint' FE model.

### **4.1.3 Material Properties**

The FE model analysis was developed progressively with an increasing level of material complexity, beginning with employing isotropic material properties, followed by the introduction of CE and the subsequent partitioning of CE.

#### **4.1.3.1 Isotropic material properties without cohesive elements**

Initial assessments were conducted on the EM with isotropic material properties at 23 °C DAM condition, without including any plasticity or failure criteria. The isotropic linear-elastic material properties adopted for the EM, fabricated using PA66-GF50, and the loading pin, composed of steel, were provided by Asahi Kasei, presented in Table 5.

**Table 5:** Isotropic material properties at 23 °C DAM condition of the EM and loading pin.

Material	Young's Modulus (GPa)	Poison Ratio (-)
PA66-GF50	10	0.35
Steel	210	0.33

#### 4.1.3.2 Introduction of Cohesive Elements

Incorporating failure prediction within the FE model necessitated the definition of CE at critical failure-prone locations. The first designated location for CE insertion was the top of the circular arc in the EM. This region experiences the greatest stress concentration due to the contact between the EM and the loading pin, as confirmed by the isotropic material property FE simulation. The second region where CE was introduced was the weldline resulting from the injection-moulding simulation. This specific weldline formation occurs during single injection port manufacturing. The precise location of the weldline was determined through injection-process simulation and subsequently verified by measuring the weldline in the EM specimen, as depicted in Figure 35.

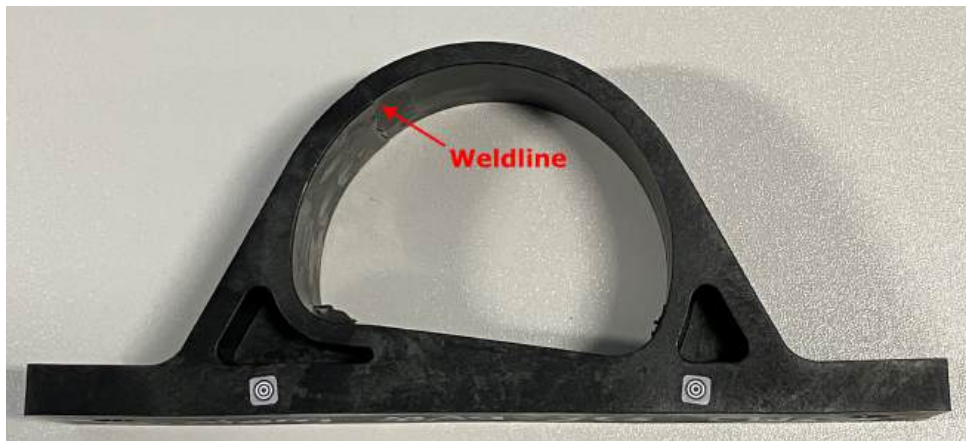


**Figure 35:** After-test EM specimen indicating the weldline location.

In the EM FE model, CE were implemented with a width of 0.1 mm, a value determined to be sufficiently small for consistent failure predictions (as evidenced by the mesh convergence study in Section 4.1.4). The schematic diagram illustrating the locations of the CE is shown in Figure 36. It is noteworthy that the two CE regions were defined in separate FE models due to a limitation in the ABAQUS software, which permits only one cohesive zone to be discretised with a single layer of CE through the thickness.



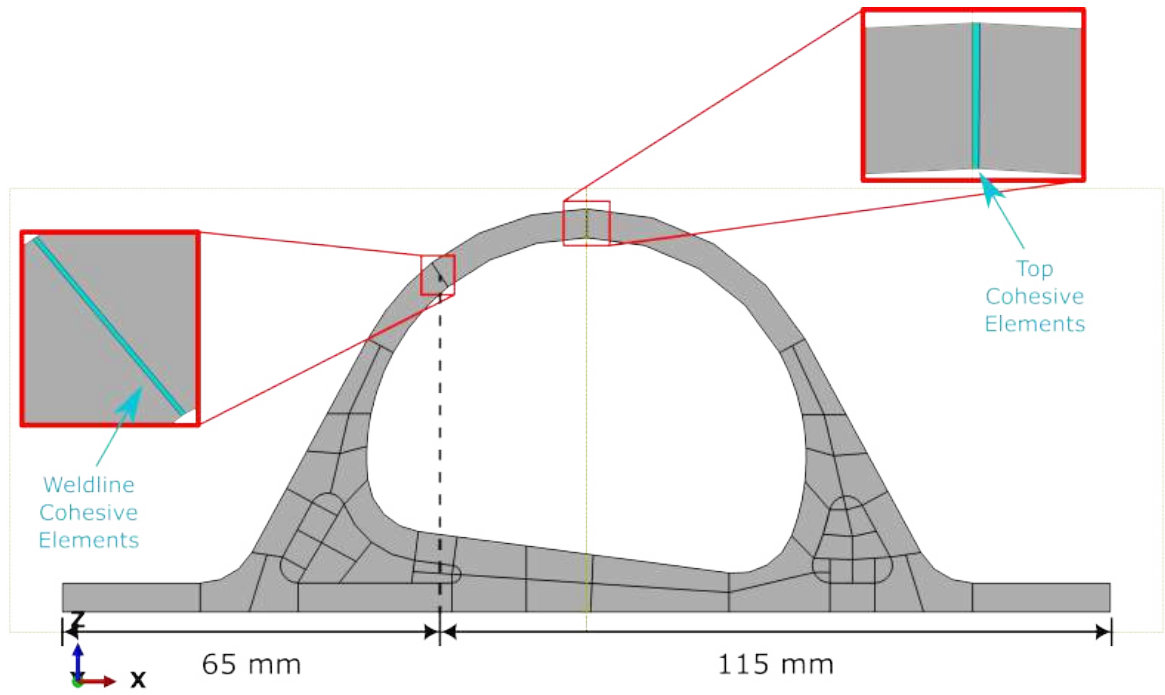


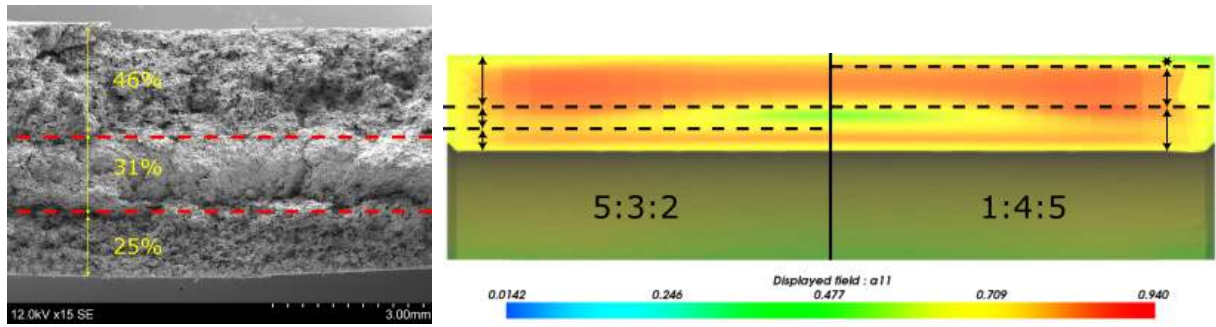
**Figure 36:** Locations of the CE in the EM cross-section.

Regarding the failure mechanism of CE, this phase employs the maximum nominal stress criterion, as outlined in Section 2.4.2, to govern the onset of damage. Subsequent damage evolution is then characterised through the use of a mode-independent energy-based criterion, as detailed in Section 2.4.3.

#### 4.1.3.3 Partitioning of Cohesive Elements

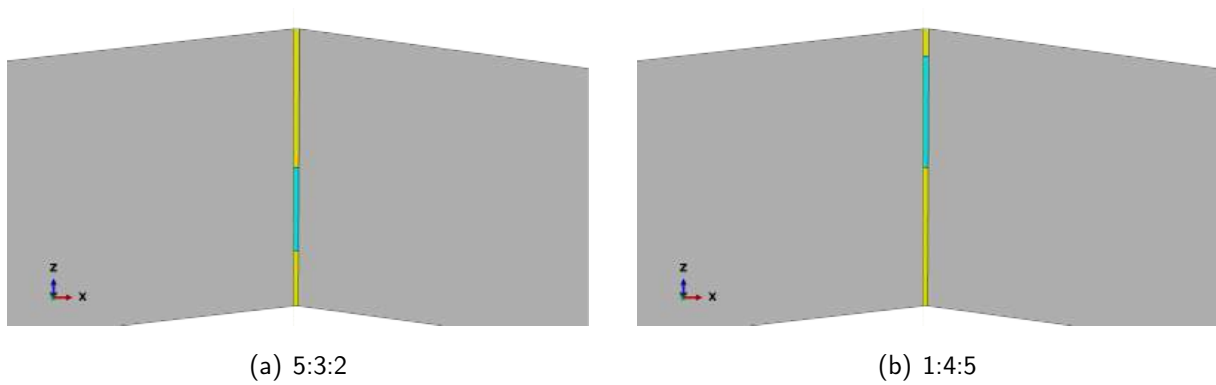
As mentioned in Section 1, IM-SFRP components exhibit a layered morphology characterised by varying FO across the thickness of the component. However, integrating CE material properties through Digimat's mapping process presents a software limitation, preventing the direct inclusion of CE material properties. Consequently, the injection-moulding simulation results for the CE region cannot be seamlessly mapped into the FE model mesh. It becomes necessary to manually partition the CE at the top-of-the-arc in the FE model to accurately simulate the layer morphology, which is bypassed during the mapping process. On the contrary, the weldline CE does not require partitioning, as the properties of the weldline are assumed to be isotropic.

Based on the injection-moulding simulation in conjunction with the fractography on the fracture surfaces shown in Figure 37, conducted by F. Yuki [4], several partition schemes consisting of different skin-core ratios and different material properties were proposed, illustrated in Figure 38 and Table 6. To compromise between precision and computational efficiency, the maximum number of partitioned layers for the CE was capped at three.



(a) SEM image of the fracture surface. (b) Moldflow a11 FO tensor contour of the EM fracture surface.

**Figure 37:** Injection-moulding simulation and SEM image illustrating skin-core ratio.



(a) 5:3:2

(b) 1:4:5

**Figure 38:** Partitioning schemes for the top-of-the-arc CE.

**Table 6:** CE material properties for different partitioning schemes.

Partition scheme & a11 FO Tensor	Young's Modulus (GPa)	Poisons Ratio (-)	Critical Stress (MPa)	Critical Fracture Energy (kJ/m <sup>2</sup> )
Top - 5:3:2 0.85/0.50/0.85	17/10/17	0.35/0.35/0.35	210/120/210	19/15.5/19
Top - 5:3:2 0.80/0.50/0.80	16/10/16	0.35/0.35/0.35	190/120/190	18/15.5/18
Top - 1:4:5 0.70/0.80/0.70	14/16/16	0.35/0.35/0.35	165/190/165	17/18/17
Weldline -	2.4	0.35	95	5.33

The first and second scheme employs a partitioned CE structure, resembling a skin-core layered configuration. The CE is partitioned to mimic the FOD of the a11 component observed in the



injection-moulding simulation (in Figure 37(b)) and the fractography of the failure surface (in Figure 37(a)). Analysis of both the contour map and the fracture surface indicates that the thickness ratio of the skin-core layers can be approximated as 48%:29%:23%, where the  $a_{11}$  component varies from  $a_{11}=0.80$  to  $a_{11}=0.85$  in the skin layers and 0.50 in the core layer. In a 10-layer element mesh, the partitioning is accomplished by a ratio of 5:3:2 through the thickness. The first scheme employs isotropic material properties with  $a_{11}=0.85$  in the skin layers, while the second scheme uses  $a_{11}=0.80$ . Both schemes consist of a core layer with isotropic properties characterised by  $a_{11}=0.50$ .

The third scheme employs a partition ratio of 1:4:5, wherein the skin layer possesses an FO tensor  $a_{11}=0.7$ , and the core layer has an FO tensor  $a_{11}=0.8$ . This partitioning accounts for a thin top layer with a lower  $a_{11}$  FO tensor. As a result, the core layer is represented by a greater  $a_{11}$  alignment of 0.8, spanning across four mesh layers. To simplify this scheme to three layers while considering the thin top layer, the entire bottom half of the cross-section is assumed to be the bottom skin core, featuring an average FO tensor  $a_{11}=0.7$ .

The weldline case involves an unpartitioned CE with isotropic material properties defined by previously conducted tensile tests on the weldline properties of PA66-GF50 [7]. In specific, the absence of fibre in the weldline yields the suitability for applying the critical fracture energy  $= 5.33 \text{ kJ/m}^2$ , corresponding to the properties of PA66 polymer. In order to facilitate faster convergence, the virtual thickness of the CE was increased by a factor of five, effectively reducing its Young's modulus from 12 GPa to 2.4 GPa. This virtual reduction in stiffness was validated by comparing it to the model without the virtual thickness increase, revealing an error within 0.53 % in the failure displacement. This substantiates the reduction of CE stiffness is a well-founded strategy, as it induces an acceptable deviation in the true failure behaviour while significantly enhancing convergence speed.

#### 4.1.4 Discretisation & Mesh Convergence Study

The discretisation of the FE model plays an important role in the EM analysis. Given the inherent complexity of the EM's geometry, adopting a structural mesh becomes essential to achieve both high simulation accuracy and efficiency. In this regard, the pentagon meshing technique [77] was implemented for the 2D EM cross-section. It requires dividing the EM's geometry into 4-5-sided 2D regions exclusively. For regions with curved sides, the pentagon meshing technique necessitates the specification of at least 10 intervals (2 per side) along the curves representing the surface perimeter. Moreover, the sum of intervals on any three connected sides must exceed the sum of intervals on the remaining two sides by at least two. Figure 39 provides an illustration of the EM geometry following the application of the pentagon partition technique.

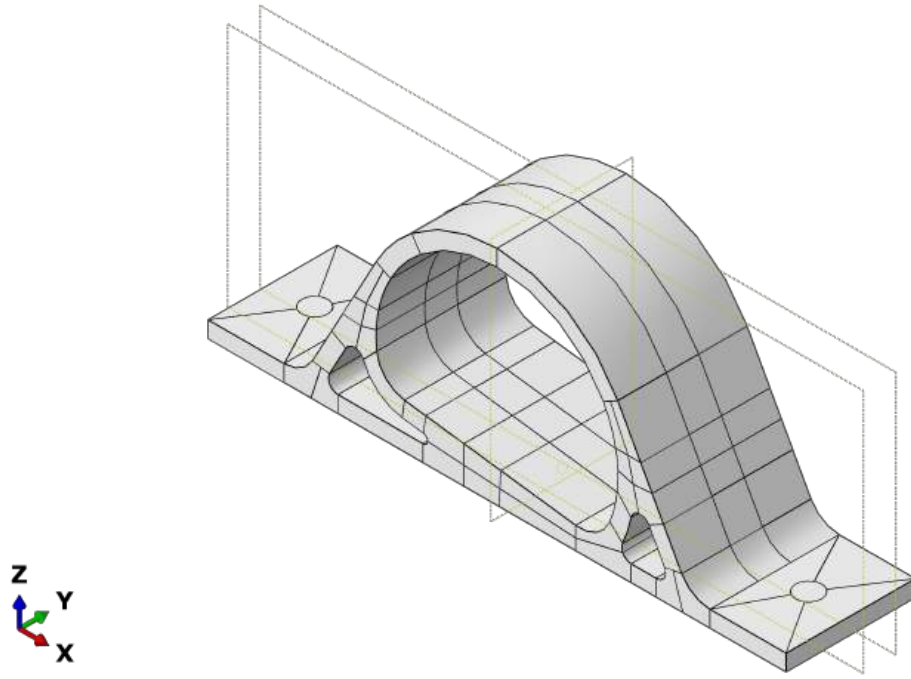


**Figure 39:** EM partitions illustrating the pentagon meshing technique.

Once the EM was partitioned, a structured mesh of the entire EM geometry was assigned using ABAQUS, shown in Figure 40(a). Additionally, mesh refinement was employed in two specific regions where failure was anticipated: the top-of-the-arc and the weldline, illustrated in Figure 40(b). Both single and double logarithmic bias mesh refinements were implemented to the circular arcs, ensuring a minimum element width of 0.4 mm. Notably, the minimum-sized elements were situated neighbouring to the CE. This selection of the minimum size elements was based on observations from several simulation trials, revealing that the CE's neighboring elements must possess a width at least three times greater than that of the CE. Any further refinement would lead to CE hourglass behavior, consequently tempering the crack initiation of the CE. The EM overall consists of 40,397 C3D8R type elements and 230 COH3D8 type elements.

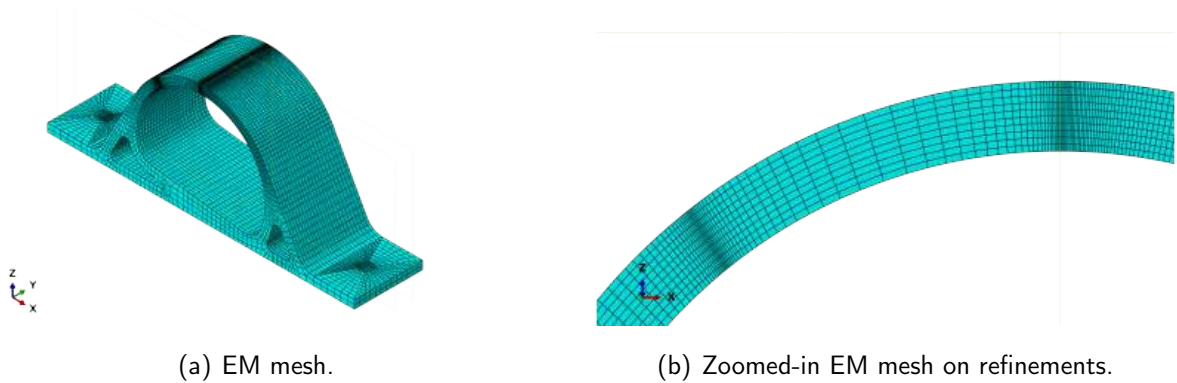


**Figure 40:** Meshing of the EM.

The discretisation of the loading pin also influences the simulation results. It was ensured that a sufficient number of elements were used to represent the surface curvature. The mesh of

the loading pin is shown in Figure 41. The loading pin overall consists of 8,640 C3D8R type elements.

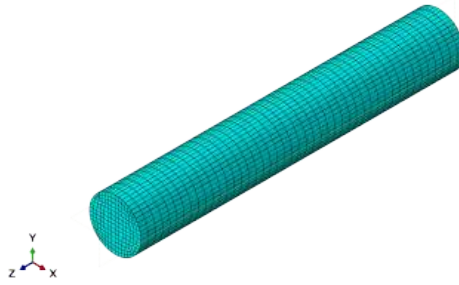


**Figure 41:** Meshing of the loading pin.

#### 4.1.4.1 Mesh Convergence Study on the Number of Layers

To accurately simulate the damage mechanism, sufficient layers of elements at the anticipated failure location are necessary. To fulfil this requirement, this mesh convergence study was conducted by developing four FE models with isotropic material properties, while varying the number of mesh layers in the arc, ranging from 4 to 15 layers. Convergence was determined using the maximum experienced load of the EM as the governing criterion. The effect of the number of layers is illustrated in Figure 42, where it is observed that convergence is achieved with 10 layers. Further increasing the number of layers has a negligible impact on the accuracy of the simulation.

Moreover, employing 10 layers of elements provides ample space to accommodate various CE ratio partition schemes. Striking a balance between computational cost and simulation accuracy, the model with 10 layers was selected for all the simulation results presented in Phase 2 of this research.

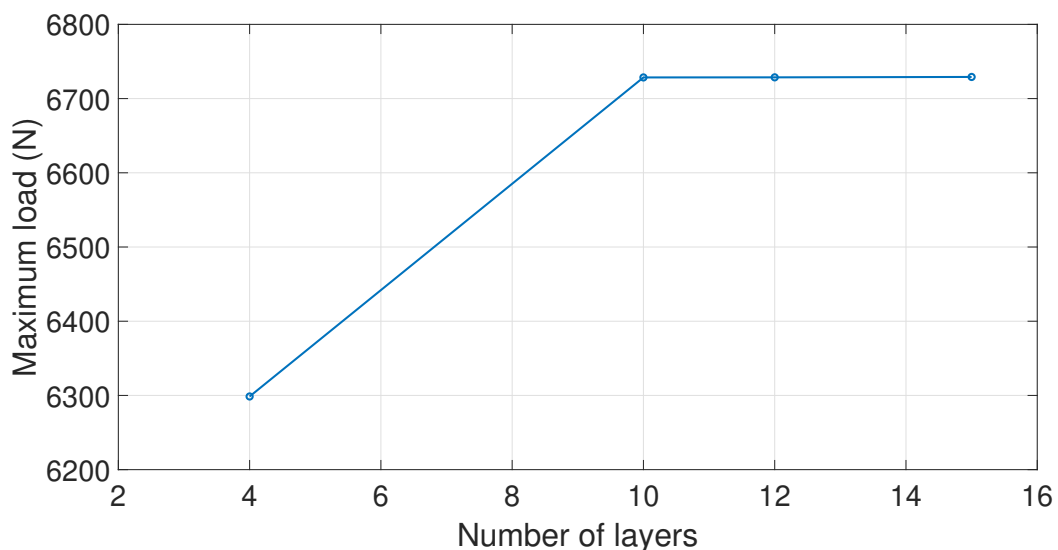


**Figure 42:** Mesh convergence study on the number of mesh layers.

#### 4.1.4.2 Mesh Convergence Study on the CE Size

Another important feature requiring a mesh convergence study is the width of the CE. Four FE model setups with isotropic material properties were developed, with various CE widths ranging from 0.05 mm to 0.40 mm. The maximum experienced load was used again as the governing criterion. The effect of the width of the CE is illustrated in Figure 43. Notably, it is observed that models employing CE widths smaller than 0.2 mm only experience minor fluctuations, thereby remaining within acceptable bounds. To maintain consistency with previously conducted simulations on the sub-component [19], 0.1 mm width CE were used for all the simulations conducted in Phase 2.

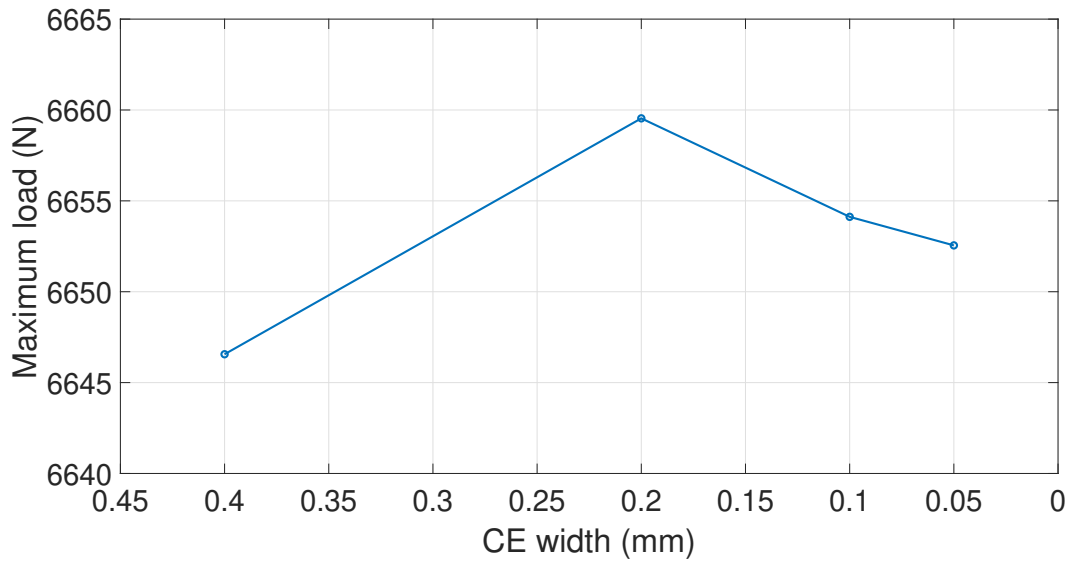


Figure 43: Mesh convergence study on the CE sizes.

#### 4.1.5 Coupled FE Analysis

Once the FE model setup has been created, coupled FEA with the injection-moulding process simulations were conducted, with the workflow outlined in the flowchart shown in Figure 14.

##### 4.1.5.1 Injection-Moulding Process Simulation

Autodesk Moldflow was employed by Y. Fujita [4] to perform the injection-moulding simulation of the EM specimen. The EM specimen investigated in this study makes use of a single injection port located as depicted in Figure 44(a), and the injection time was set to 3 seconds. The result of the injection-moulding simulation provided the FOD across the entire structure based on a probability distribution function. Figure 44(b) illustrates the computed  $a_{11}$  component of the FO tensor within the structure.

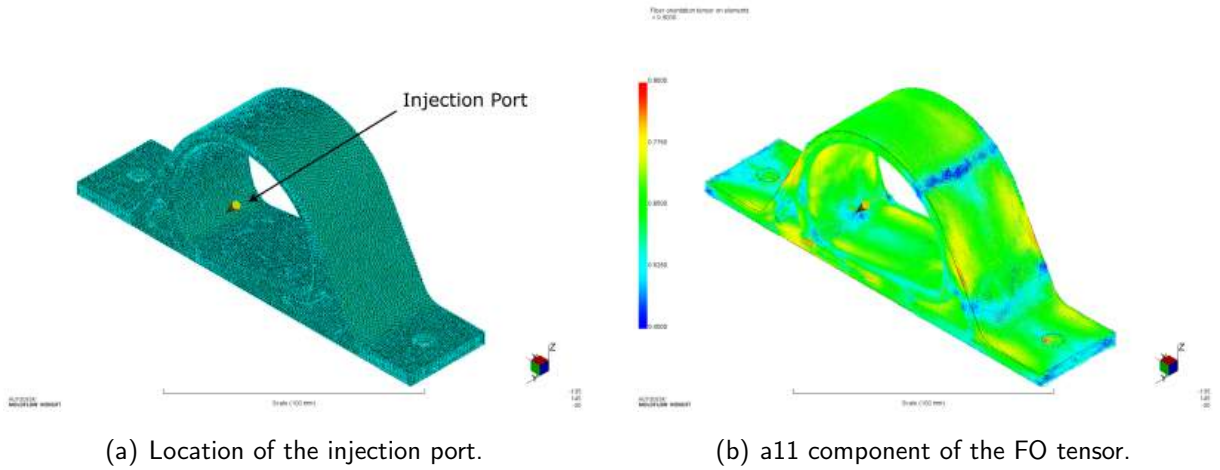


**Figure 44:** Moldflow injection-moulding simulations.

#### 4.1.5.2 Fibre Orientation Mapping

The output .xml file obtained from Moldflow, which contains the FO information, along with the .pat file containing the mesh adopted in the injection-moulding simulation, are subsequently imported into Digimat-Map as the donor mesh. In the next step, the FOD data is mapped onto the FE model mesh as the receiving mesh by defining the nodal fibre orientation tensor at each integration point of the FE model. This mapping procedure generates a new output .dof file, encompassing the mapped FO data within the FE model mesh. As mentioned in Section 4.1.3, due to the limitation of Digimat-Map, the FO is mapped to the entire EM specimen except for the region of the CE. Figure 45 illustrates the a11 component of the FO tensor after being mapped into the FE model mesh.

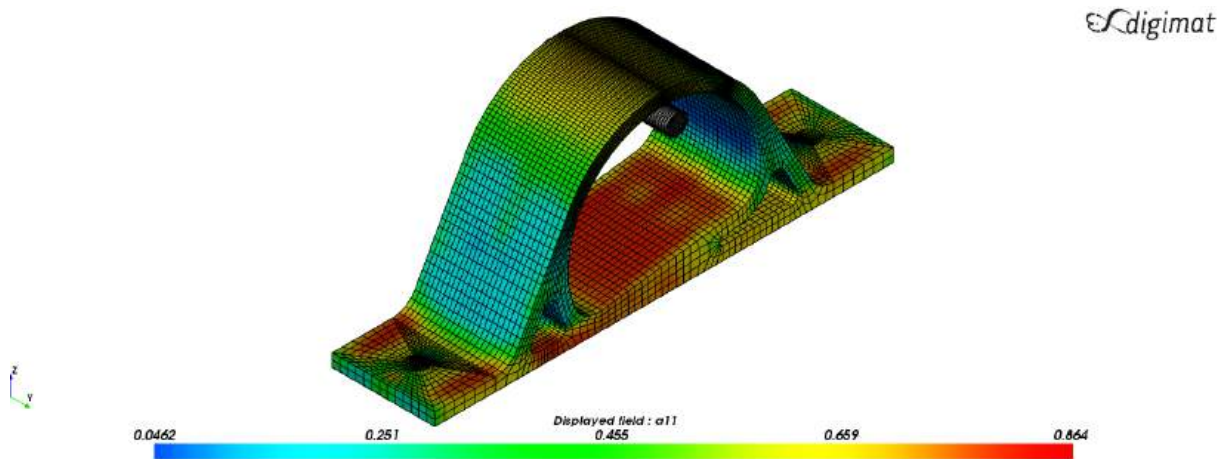


**Figure 45:** Mapping of fibre orientation in Digimat-MAP.

#### 4.1.5.3 Coupled Simulation

In the final step of the coupled simulation procedure, the ABAQUS input .inp file and the FOD mapped .dof file are both imported into Digimat-RP. Prior to the coupled simulation,

a material property .daf file is generated with Digimat-MX for the PA66-GF50 composite under 23°C DAM condition, containing its anisotropic behaviour within the 0° - 90° FO range. The construction of this material property file is based on previously conducted tensile tests reported by Yuki et al. [7]. Following this preparatory step, the material information is integrated into every node in the FOD mapped EM mesh according to the predicted fibre orientation. Notably, the material information effectively overwrites the isotropic material properties previously defined in ABAQUS, except for the CE, where the material properties are directly transferred from ABAQUS. Finally, a coupled injection-moulding simulation and FE analysis are executed via the Digimat-RP interface.

## 4.2 Results

### 4.2.1 Determining Optimal Boundary Conditions Configuration

The load-displacement curves corresponding to the five boundary condition simplification cases, simulated using isotropic material properties as discussed in Section 4.1.2, are presented in Figure 46. Evidently, all considered simplifications, including the analytical rigid pin, bottom constraint, fixture constraint, and the model without legs, lead to an impractical increase in stiffness compared to that in the baseline boundary condition, which consists of solid element pin, fixtures and platform modelled as a plate with friction. This insight underscores the suitability of the baseline boundary condition to be the most suitable for the subsequent coupled simulations.

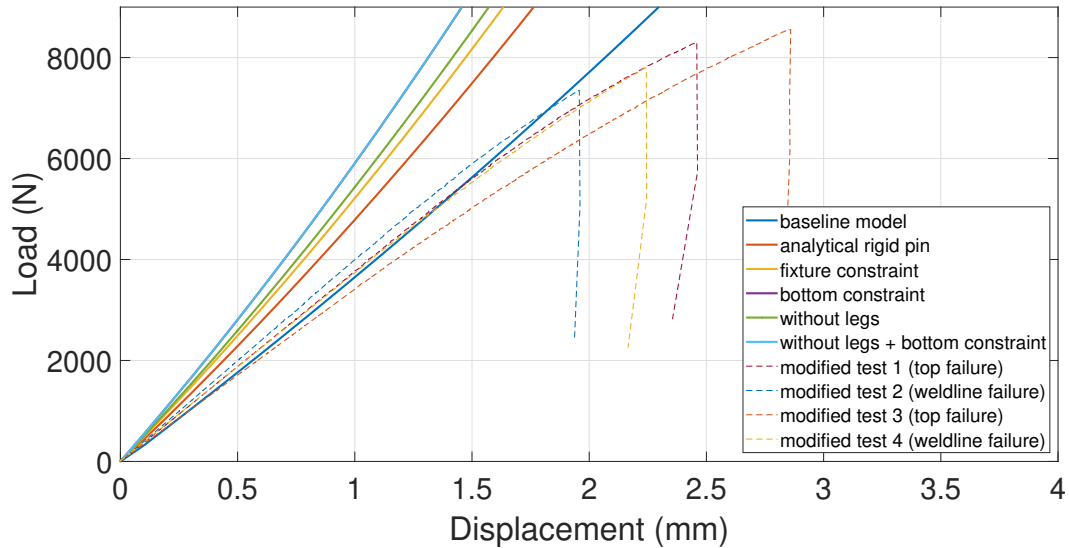


**Figure 46:** Load Displacement curves of various boundary conditions with the modified experiment results (explored in Section 4.2.2).

### 4.2.2 Experiment Data Modification for the Initial Stiffening Effect

Figure 47 showcases the load-displacement curves for the four EM specimens under investigation. Notably, failures were observed at the top-of-the-arc in two specimens, while the remain-

ing two exhibited weldline failures. Although the failure loads at the top-of-the-arc seemingly surpass those at the weldline, it is important to note that all four specimens displayed scattered failure loads. This variability can be attributed to inconsistencies in manufacturing, the presence of defects, and minor discrepancies in experimental calibration. Moreover, it is worth highlighting the emergence of stiffening effects at an approximate displacement of 0.3 mm. Initially, all four specimens demonstrated consistent stiffness as characterised by the curve's slope. However, beyond the 0.3 mm displacement mark, there was a noticeable divergence as stiffness increased across all specimens by varying degrees.

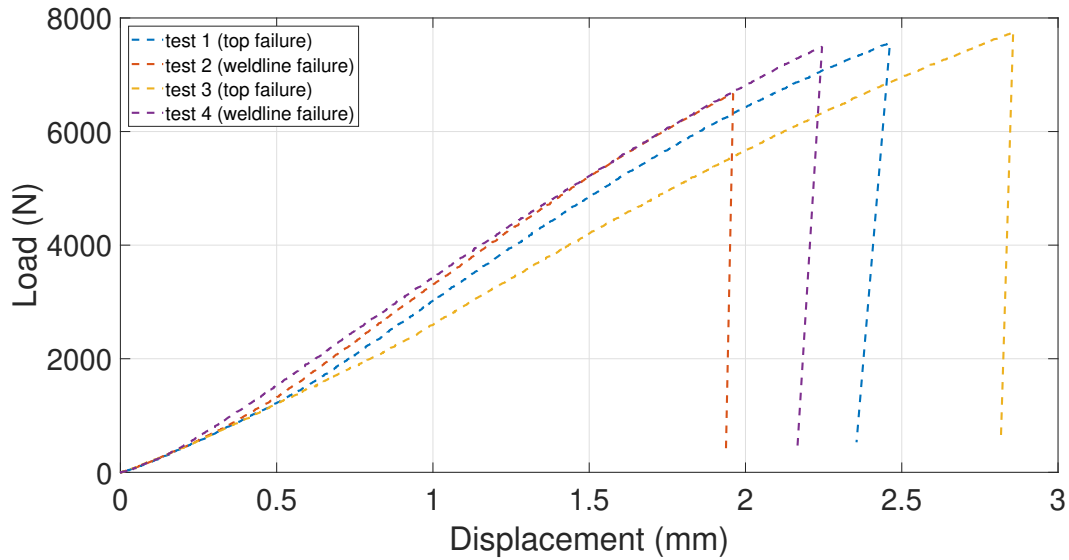


**Figure 47:** Load-Displacement curves of the tensile experiments.

Regarding this stiffening effect, four possibilities were explored in the following.

### I. Sliding of the EM

Firstly, the EM could experience horizontal sliding in the x-direction during the tensile loading process. To verify this, the horizontal displacements of the two side trackers recorded by the video extensometer shown in Figure 48 were investigated. However, there was no clear evidence showing a simultaneous occurrence of sliding and stiffening. Load-displacement curves in the horizontal direction can be found in Appendix A.2.

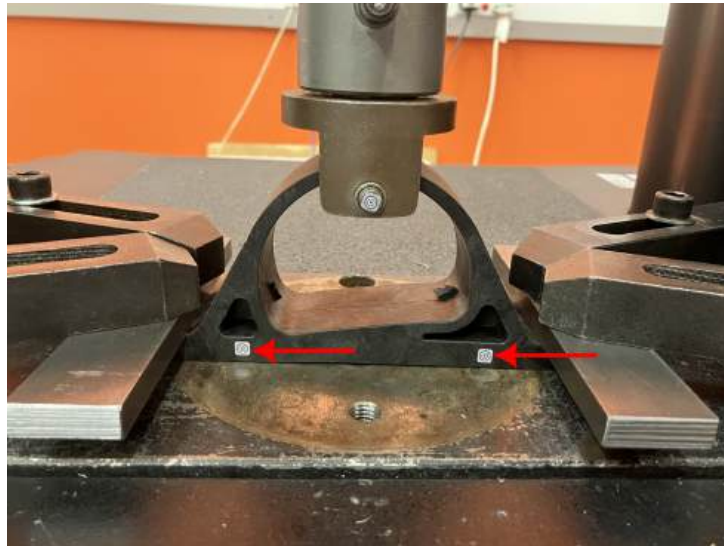


**Figure 48:** Side trackers on the EM in tensile experiments.

## II. Tilting of the Loading Pin

Another plausible explanation considered was the potential tilt of the loading pin, leading to differing z-positions at the pin's opposing sides. Initially, the pin and EM shared a point contact, transitioning to line contact upon EM deformation. The accumulating load imbalance in the system could contribute to the observed stiffening effect. Variations in arc thickness on either side could similarly induce a stiffening effect when combined with a tilted loading pin. To assess this, measurements of specimen average thickness on both sides of the arc revealed minor differences of 0.15 mm, which may contribute to the stiffening phenomenon. Since conducting a more comprehensive FEA validation would require the reconstruction of the entire EM geometry, it was deemed overly complex and time-consuming, and thus was not pursued.

## III & VI. Pin Misalignment in the x and y Directions

Moreover, pin misalignment was considered as another potential factor leading to stiffening. During the test setup, manual positioning of the pin inevitably introduced slight misalignments in the x-direction. This misalignment could initiate pin rotation and subsequent positional adjustments until moments balancing the pin's rotation were achieved in both directions. A validation simulation of shifted pin positions in the x-direction was conducted, wherein the pin was intentionally offset by 5 mm in the x-direction, as depicted in Figure 49.



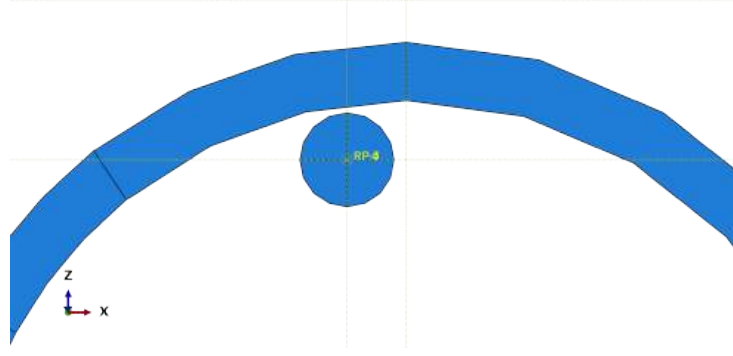


**Figure 49:** Schematic of pin offset by 5mm in the x-direction.

Additionally, the length of the loading pin was longer than the depth of the EM. To maintain a consistent test setup each time, tensile tests were performed with the EM positioned to nearly touch the front of the loading pin jig, leaving a longer pin length at the back of the EM. Given that the pin is not perfectly rigid, this setup could result in a non-uniform load distribution across the EM. To explore this hypothesis, another simulation was conducted with the pin shifted in the y-direction, such that its front aligned with the EM's front surface, as shown in Figure 50.

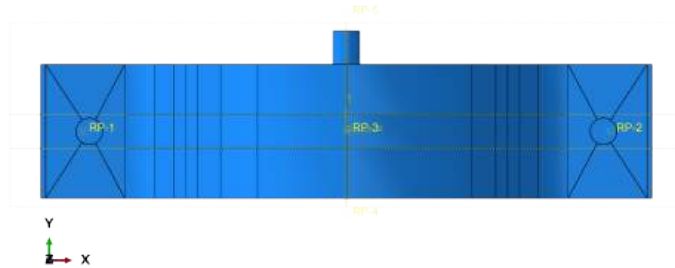


**Figure 50:** Schematic of pin offset in the y-direction.

The load-displacement curve of the shifted pin simulation in the x and y directions is shown in Figure 51. The load-displacement curve clearly indicates that a pin misaligned in the x-direction induces stiffening within the 0 to 0.2 mm displacement range. While this confirms the existence of a stiffening effect, its magnitude varies from what was observed in the actual tensile tests. Meanwhile, a pin misaligned in the y-direction only exhibited a minor stiffening impact. In light of these results, x-directional pin misalignment appears to be the more significant contributor to stiffening, while y-directional misalignment has a lesser effect.

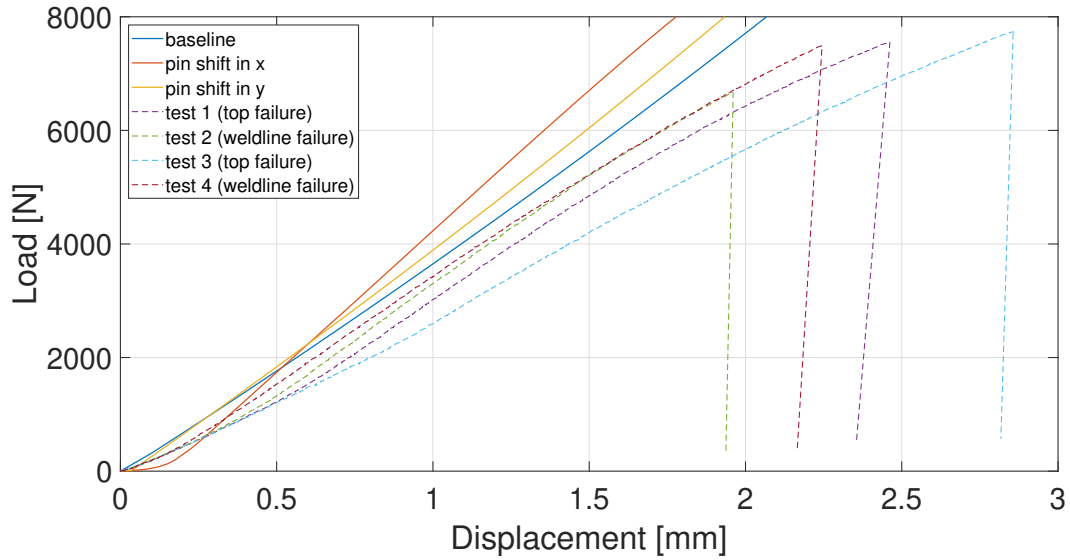


**Figure 51:** Load-Displacement curves of pin shift simulations versus without pin shift.

To ensure equitable comparisons between test and simulation curves in later result sections, test curves were manually calibrated to exclude the effect of stiffening. This involved substituting regression lines up to the initial stiffening point and subsequently shifting the starting point of each curve to zero displacements and zero loads. The resultant modified test curves are illustrated in Figure 52.

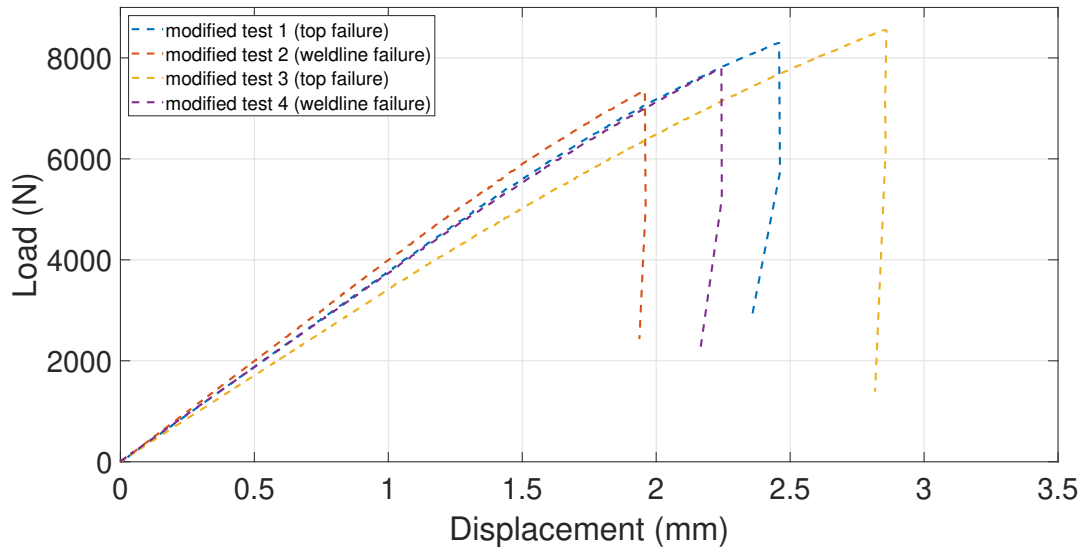


**Figure 52:** Modified Load-Displacement curves of the tensile experiments.

#### 4.2.3 Coupled FE Analysis with CZM

As elaborated in Section 4.1.3, three simulations incorporated the three different CE partitioning schemes for the top-of-the-arc failure, whereas, the unpartitioned CE scheme was incorporated for the weldline failure. Figures 53 and 54 present the load-displacement curves of the coupled injection-moulding and FE simulations conducted on the EM upon the top-of-

the-arc and weldline failures respectively. Their corresponding initial stiffness and failure loads are detailed in Tables 7 and 8.

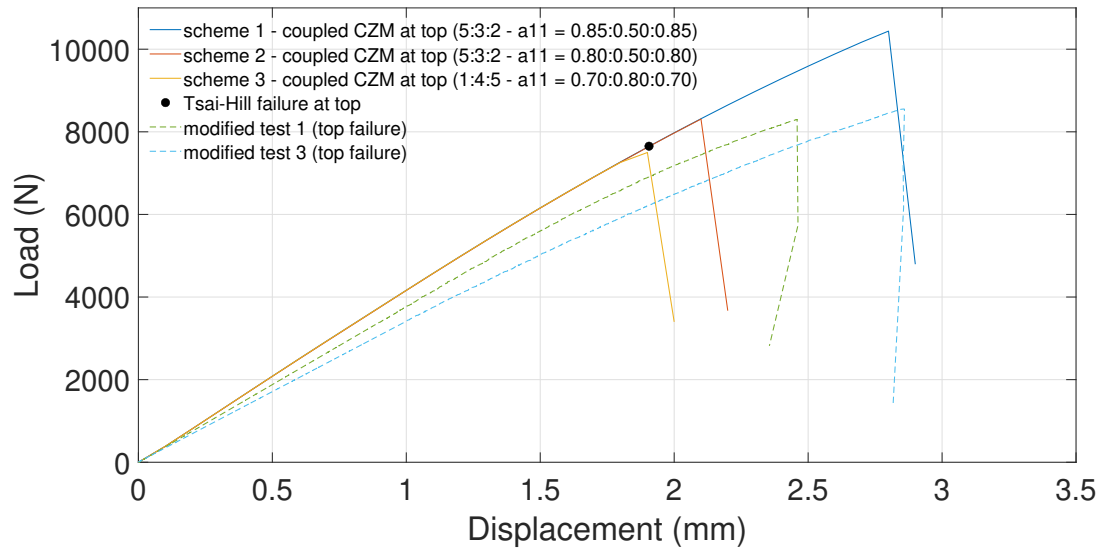


**Figure 53:** Load-Displacement curves of the coupled FE analysis with CE for top-of-the-arc failures.

**Table 7:** Initial stiffness and failure loads of the modified tests and coupled FE simulations for top-of-the-arc failures.

No.	Test/ Simulation Details	Initial Stiffness (N/mm)	Failure Load (N)	Accuracy (%)	
				Test 1	Test 3
Test 1	Top failure	3774.6	8275.2	-	-
Test 3	Top failure	3408.2	8549.6	-	-
Tsai-Hill	Top failure	-	7652.0	92.5	89.5
Scheme 1	Coupled Top CE, 5:3:2, $a_{11}=0.85/0.50/0.85$	4161.1	10438.4	73.9	77.9
Scheme 2	Coupled Top CE, 5:3:2, $a_{11}=0.80/0.50/0.80$	4157.9	8308.6	99.6	97.2
Scheme 3	Coupled Top CE, 1:4:5, $a_{11}=0.70/0.80/0.70$	4160.6	7498.8	90.6	87.7

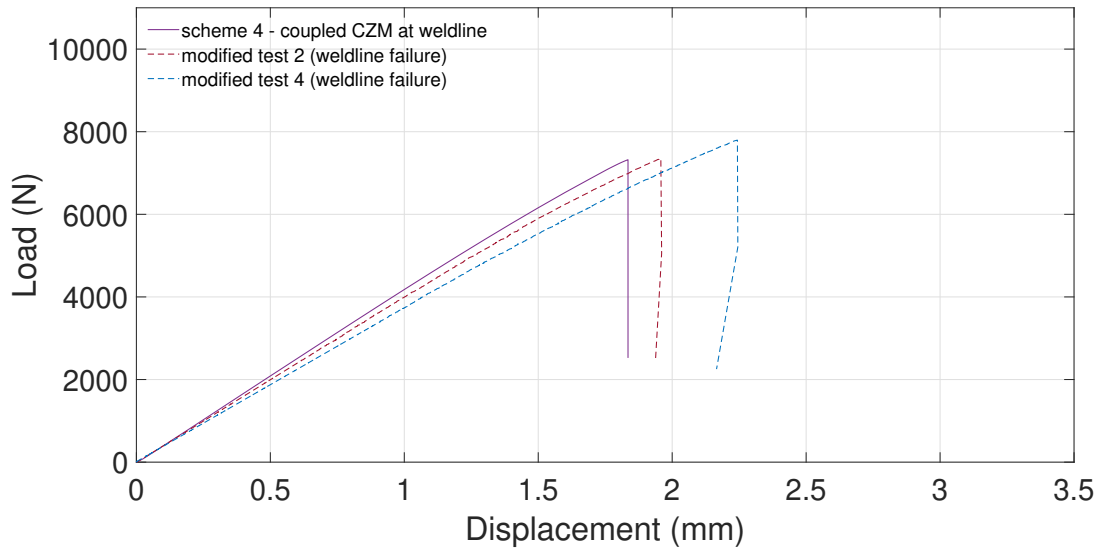


**Figure 54:** Load-Displacement curves of the coupled FE analysis with CE for weldline failures.

**Table 8:** Initial stiffness and failure loads of the modified tests and coupled FE simulations for weldline failures.

No.	Test/ Simulation Details	Initial Stiffness (N/mm)	Failure Load (N)	Accuracy (%)	
				Test 2	Test 4
Test 2	Weldline failure	4002.4	7318.6	-	-
Test 4	Weldline failure	3732.0	7759.4	-	-
Scheme 4	Coupled Weldline CE	4179.2	7321.1	99.9	94.4

The observed stiffness across the four coupled simulations remains consistent, with only minor deviations attributed to variations in CE properties. A comparison with the stiffness values derived from the tensile tests reveals marginal overestimations in the coupled simulations by varying degrees. The cause of overestimations originated from manufacturing defects within the EM specimens. For instance, test 2 consists of an initial stiffness of 4002.4 N/mm, while test 3 exhibits a stiffness of 3408.2 N/mm. This demonstrates the EM specimens' potential to attain stiffness levels of at least 4002.4 N/mm, with limitations stemming from manufacturing defects. Despite these minor discrepancies, the strong concordance in stiffness values suggests that the injection-moulding process simulations successfully captured the FO characteristics of the EM specimens.

For the top-of-the-arc failure simulations compared to tests 1 and 3 (Figure 53 and Table 7), it shows that Scheme 2 resulted in the most accurate failure load prediction with an average

accuracy of 98.4 %, despite observing a slight underestimation in failure displacement than those in the tests. It is followed by Scheme 3, demonstrating an average accuracy of 89.2 % with underestimations in both failure load and displacement. For Scheme 1, while yielding the closest failure displacement to that observed in test 1, it obtained an overestimation in the failure load with the lowest average accuracy of 75.9 %. Overall, the partitioning scheme of 5:3:2 with FO tensor  $a_{11}$  of 0.80/0.50/0.80 offers the best replication of the skin-core morphology of the top-of-the-arc fracture plane.

In the case of weldline failure simulations (Figure 54 and Table 8), compared to tests 2 and 4, Scheme 4 shows a high average accuracy of 97.2 %, while also showcasing a slightly earlier failure displacement. This simulation well characterises the weldline failures observed in the EM specimens.

Focusing on the Tsai-Hill failure criterion relative to Scheme 2, significant underestimations of failure loads and displacements were observed across all top-of-the-arc failure simulations. These underestimations in failure loads ranged from 7.5 % to 10.5 % compared to tests 1 and 3. Meanwhile, the Tsai-Hill failure criterion failed to predict weldline failure.

## 4.3 Discussion

Phase 2 of the project investigates the applicability of a virtual testing methodology for simulating both the mechanical behaviour and failure properties of EM. Results indicate that the methodology involving coupled injection-moulding and FE analysis with CE offers accurate predictions for the stiffness behaviour as well as the failure load of EM under tensile testing.

### 4.3.1 Boundary Condition Analysis

Prior to the execution of coupled simulations, various boundary condition schemes were evaluated to simplify the EM loading model and thereby reduce computational time. However, all the modifications proposed resulted in an impractical increase in stiffness compared to the baseline condition. This outcome highlighted the presence of over-constraints in each altered model. For example, the use of encastre boundary conditions instead of plates with friction negated the effect of sliding of the EM, resulting in increased stiffness. It was also found that analytical rigid shell pins were inadequate for accurately modelling the tensile loading scenario. During the tensile test, the load is applied on the two sides of the pin, and a non-uniformly distributed load contact interface is formed following the pin deformation. Consequently, solid element pins were deemed necessary for a realistic representation of unevenly distributed load contact. The investigation thus concludes that the optimal boundary condition for the EM simulations requires complex setup configurations, and computational time cannot be reduced by simplifying the loading model.

### 4.3.2 Stiffness Comparisons

Following the determination of appropriate boundary conditions, coupled simulations were carried out. The FO tensor was mapped onto the FE mesh to account for the anisotropic properties of IM-SFRP. CE were applied to integrate failure properties into the EM model. Although the simulations led to slight overestimations in stiffness, the scattered stiffness data recorded in the four tensile tests shown in Figure 47 suggests the likelihood of inconsistencies in specimen preparation. For instance, a small variation in injection time can potentially lead to significant FO differences, as the layer morphologies of IM-SFRP are produced from the shear effect induced by the velocity profile. In addition, the PA66 matrix in SFRP is highly influenced by the temperature and moisture content of the surroundings. The moisture content of the EM specimens tested was likely to be slightly higher, varying from specimen to specimen, rather than maintaining its original DAM condition. Given that the simulations assume ideal manufacturing and testing conditions, the extent of the overestimation in stiffness is considered to be expected.

### 4.3.3 Failure Predictions

Despite variations in observed failure loads, attributed to the aforementioned inconsistencies in specimen preparation, the coupled simulation with CZM showed promising alignment with experimental data, as seen in Figures 53 and 54. Specifically, the 5:3:2 partitioning scheme and the FO tensor of  $a_{11}=0.80/0.50/0.80$  yielded a predicted failure load of 8308.6 N. This prediction falls between the observed failure loads of 8275.2 N and 8549.6 N, which were associated with top-of-the-arc failures. Similarly, in the weldline failure simulation, the predicted failure load was 7321.1 N, falling within the range of the two observed weldline failure specimens at 7318.6 N and 7759.4 N. These findings validate the capability of the coupled simulations to offer accurate failure load predictions for IM-SFRP EM. However, the 5:3:2 partition scheme with  $a_{11}=0.85/0.50/0.85$  and 1:4:5 with  $a_{11}=0.70/0.80/0.70$  led to over-predictions and under-predictions on top-of-the-arc failure respectively. This highlights failure predictions of IM-SFRP structure are highly dependent on the CE properties. Due to the limitation of Digimat, layer morphology and material failure properties can only be implemented by manually partitioning and inputting failure properties into the CE. This emphasises the criticality of selecting appropriate partitioning schemes as well as failure properties for CE.

On the other hand, simulations reveal significant underestimations of failure loads when using the conventional failure criterion, namely the Tasi-Hill failure criterion which solely relies on the failure initiation as a governing criterion. Moreover, the Tsai-Hill failure criterion does not consider weldline failure, which is a common failure location for components fabricated by

SFRPs. This outcome is in line with prior studies [7, 19], reinforcing the importance of adopting CZM for SFRP materials. CZM leverages both failure initiation and propagation, presenting itself as a more comprehensive and accurate choice for simulating the failure behaviour of SFRP materials.

#### **4.3.4 Investigation of Stiffening Effect**

Prior to planning future experimental tests, FE simulations were conducted to provide theoretical explanations for the stiffening effect observed in prior test data. Four hypotheses were considered: horizontal sliding of the EM, imbalanced loadings due to pin tilt or thickness variations, and pin misalignment in the x and y directions. Horizontal sliding was ruled out based on the finding that the sliding occurred at a later instance than the initially introduced stiffening. The second hypothesis was substantiated through after-test measurements, revealing accountable thickness differences at the top-of-the-arc in the EM specimens. Regardless of whether this thickness difference was present due to manufacturing defects or a tilted positioned pin, it serves as a contributing factor towards stiffening. Finally, FE simulations replicating pin misalignment in the x-direction in Figure 51 showed notable stiffening, which in combination with the rotating motion of the pin, was considered the primary cause of the observed stiffening in tensile tests. Future studies could delve deeper into the actual extent of pin misalignment during tensile tests.

## 5 Phase 3 - Experimental investigation of compressive properties of IM-SFRP

### 5.1 Experimental Methods and Specimen Manufacture

The primary objectives of the experiment are to determine the ultimate compressive strength and compressive modulus of PA66-GF50 material. The experiment is conducted in accordance with the ASTM D695-15 standard [78]. The data obtained from these compressive tests are subsequently compared to the results of tensile tests, as conducted by Y. Fujita [7]. To ensure consistency, the test conditions employed in the compressive tests closely mirrored those utilised in the tensile tests, as outlined in Table 9.

**Table 9:** Key test information.

	<b>Tension</b>	<b>Compression</b>
<b>Material</b>	PA66-GF50	PA66-GF50
<b>Thickness</b>	2 mmt	2 mmt
<b>Strain rate</b>	$1 \times 10^{-3}$	$1 \times 10^{-3}$
<b>Machining angles</b>	0°, 45°, 90°	0°, 45°, 90°
<b>Number of tests (in each FO)</b>	5	3
<b>Environmental conditions</b>	23°C-DAM	23°C-DAM

Specimens were divided into three batches, each consisting of one 0°, 45° and 90° FO specimen. Compression tests were conducted in the sequence of batch 1, batch 2 and batch 3.

#### 5.1.1 Test Apparatus

Table 10 summarises the apparatus selected for the experiment.



**Table 10:** Summary of apparatus selected for compressive test.

Apparatus	Name	Notes
Compression machine and Load indicator	Instron 3369	Type: Electromechanical Capacity: 50 kN Accessories: Compression platens, extension arms
Strain indicator	Imetrum Universal Video Extensometer	-
Supporting jig	Thin specimen supporting jig and base	Accessories: 2 mm and 3 mm steel plates for specimen elevation
Clamping instruments	2 x G-clamps	-
Measuring instruments	Micrometre and Vernier calipers	-

### 5.1.2 Specimen Preparation

Dogbone-shaped coupons were cut at 0°, 45° and 90° with respect to the flow direction. A single specimen was selectively machined from each plaque, consistently extracted from the centre of the plaque, to ensure a high degree of uniformity in FOD across the entire thickness of all specimens. Figure 55 indicates the corresponding locations and orientations with respect to the injection flow direction. The specimens were prepared by employing water jet cutting to extract sections from the material plates. It was ensured that the specimen achieved the desired tolerances and surface finish. Specifically, specimen batch 3 was subjected to further machining to have smooth, flat parallel surfaces with sharp, clean edges, with a maximum deviation of 0.025 mm perpendicular to the longitudinal axis of the specimen (as specified in D695-15). Dimensions for the compression specimens are shown in Figure 56.

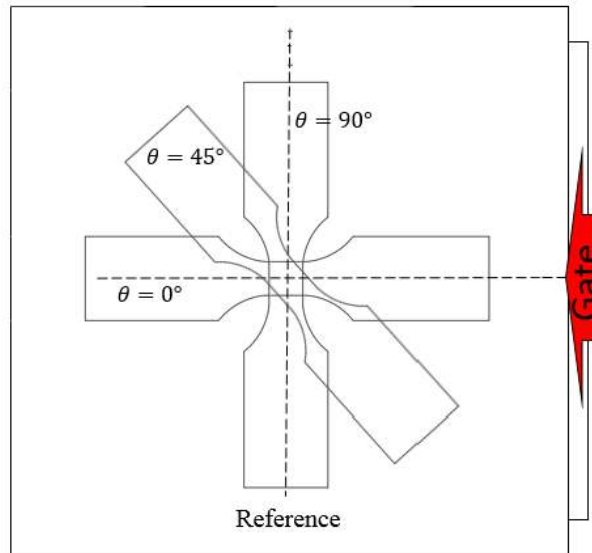


**Figure 55:** Direction and location of specimens cut from injection moulded plaques (arrows indicate the injection moulding direction and the dashed areas are discarded materials) [8].

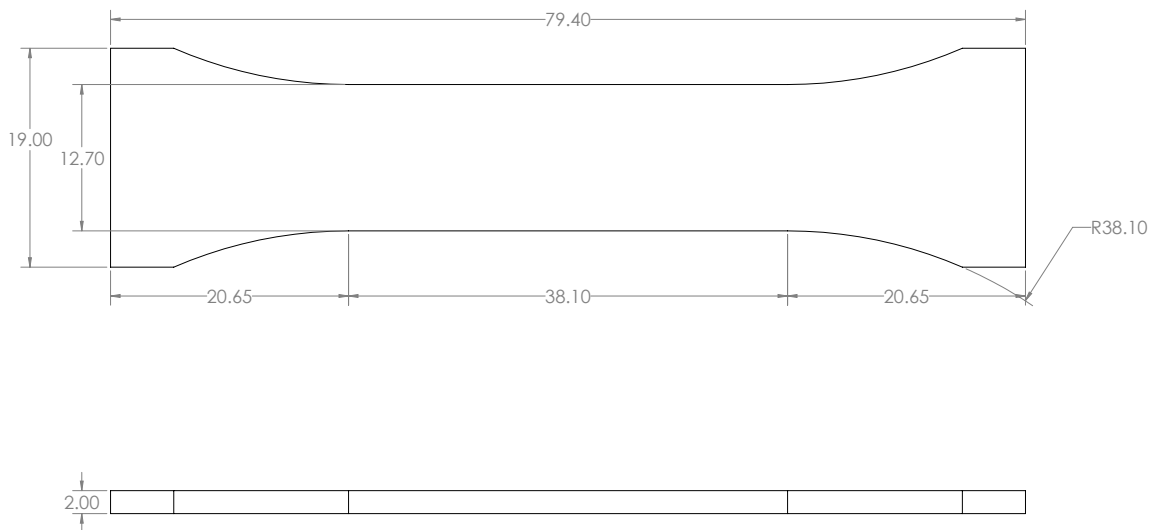
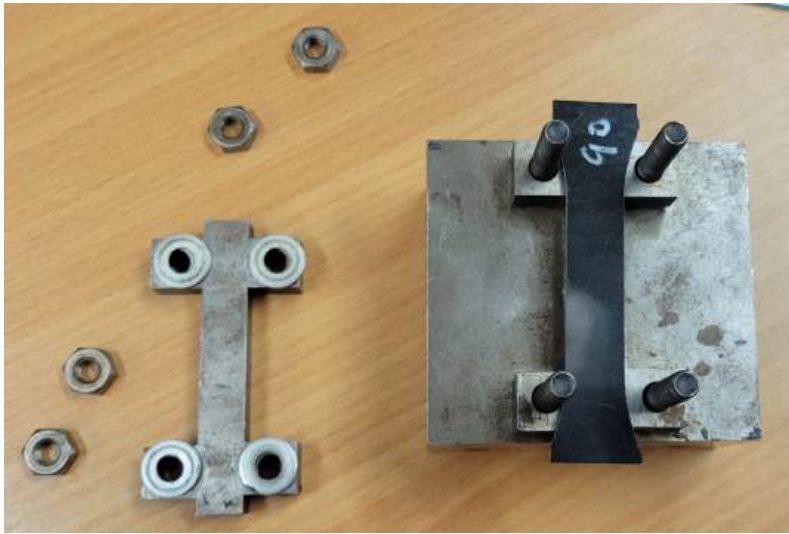


**Figure 56:** Dogbone specimen dimensions for compressive testing.

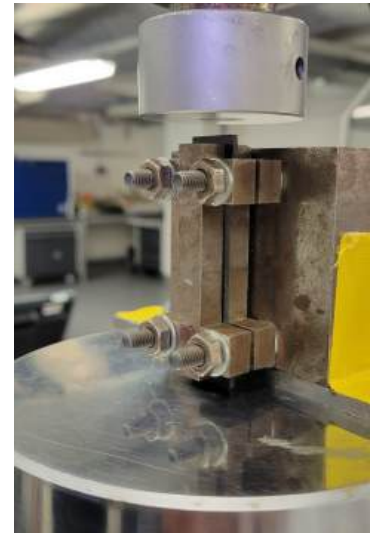
### 5.1.3 Experimental Setup

Figure 57 depicts the experimental setup and the compression jig designed for testing thin specimens. The jig was firmly secured to the lower compression plate using a pair of G-clamps, ensuring unobstructed access to the sample. This apparatus arrangement facilitates

a clear view for the acquisition of strain measurements through the use of a video gauge extensometer.



(a) Thin specimen compression jig.



(b) Compressive test setup.

**Figure 57:** Compressive test configurations.

#### 5.1.3.1 Conditioning

The experiments are conducted under dry-as-moulded (DAM) conditions, at a controlled temperature of 23°C. Since the specimens are consistently stored under the designated test conditions, there is no need to implement conditioning procedures prior to conducting the tests.

#### 5.1.3.2 Departure from Standard

The compression jig employed in the compressive experiments has a fixed displacement length of 3.5 mm, corresponding to the portion of the specimen exposed above the jig. It was observed that the PA66-GF50 dogbone specimens batch 1 did not achieve failure within this predefined displacement range. To accommodate this, steel plates of 2 mm and 3 mm thickness were placed under the specimens in batches 2 and 3, effectively extending the available displacement lengths to 5.5 mm and 6.5 mm, respectively.

#### 5.1.4 Experimental Procedure

The experimental procedures follow the D695-15 standard [78], as shown below.

1. Measure the width and thickness of the specimen to the nearest 0.01 mm at three locations along its gauge length. Register the three values and calculate the average specimen thickness. Calculate and record the minimum value of the cross-sectional area. Measure the length of the specimen and record the value.

2. Place the test specimen between the surfaces of the compression tool. Align the centre line of its long axis with the centre line of the plunger and to ensure that the ends of the specimen are parallel with the surface of the compression tool. Adjust the crosshead of the testing machine until it just contacts the top of the compression tool plunger.
3. Place thin specimens in the jig as shown in Figure 57(a) and 57(b), so that they are flush with the base and centre. The nuts or screws on the jig shall be finger tight. Place the assembly in the compression tool.
4. Setup a video extensometer to measure the compressive strain on the specimen. Define the gauge length to be used.
5. Estimate a load-time and displacement-time curve.
6. Set the speed control at 1.3 mm/min and start the machine.
7. Record the complete load-deformation curve.
8. Record load level and strain level at discontinuities.
9. After the yield point has been reached, continue to run the machine until the sample reaches complete failure.
10. Take photographs of the samples with scale.
11. Store the samples safely for further analysis.

## **5.2 Results**

### **5.2.1 Stress-Strain Curves**

Figure 58 displays the compressive stress-strain curves for the tested nine specimens, grouped in batches of three for each orientation:  $0^\circ$ ,  $45^\circ$ , and  $90^\circ$  FO. It's important to note that specimen batches 1, 2, and 3 were subjected to displacements of 3.5 mm, 5.5 mm, and 6.5 mm, respectively. Particularly, only the  $0^\circ$  FO specimens in batches 2 and 3 reached the point of failure. The remaining specimens did not reach failure due to the limited clearance between the jig and the exposed length of the specimen. Towards the end of the loading process, the sudden stress increase corresponds to the top loading platen's impact with the jig. The dogbone specimens can no longer be compressed further at this stage, owing to the restricted clearance.

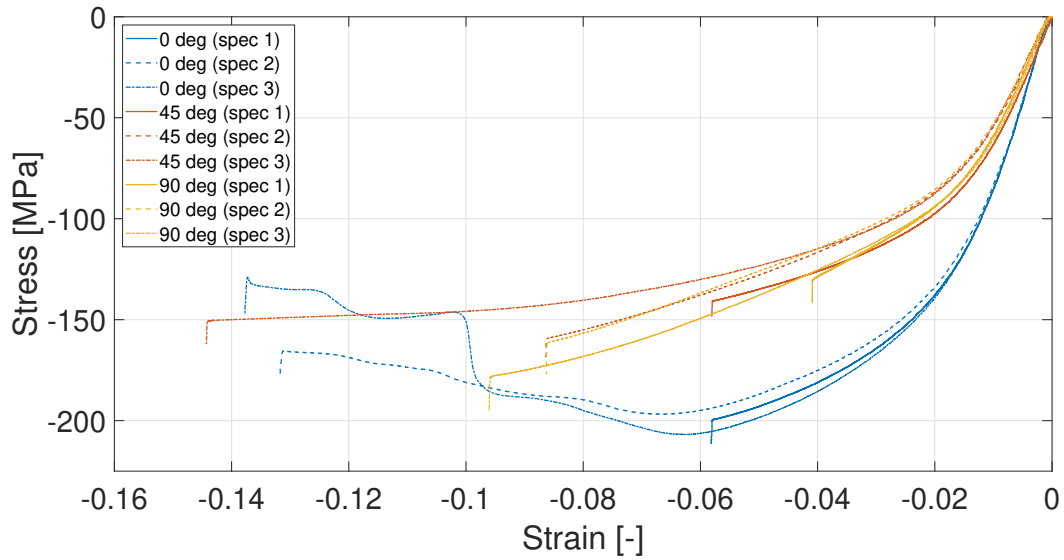
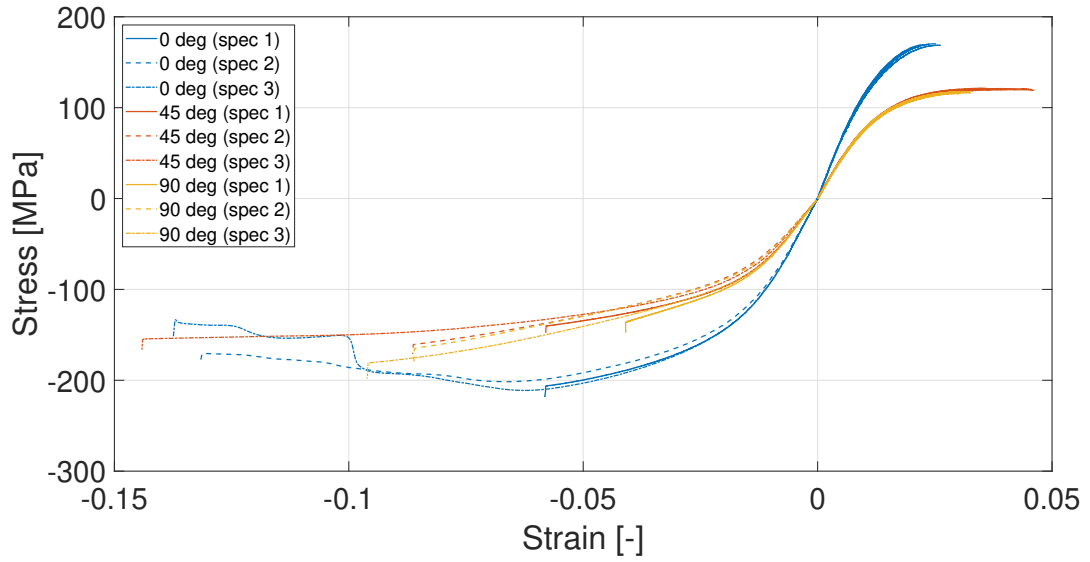


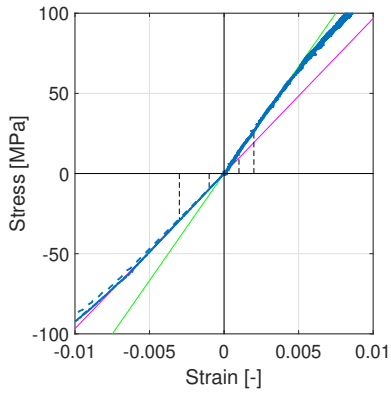
**Figure 58:** Compressive stress-strain curves for IM-SFRP dogbone specimens.

Minor non-linearity is evident in the stress-strain curves at low strains across all specimens, which could be attributed to uneven specimen loading. Notably, it is observed that the three 0° FO specimens show consistent compressive modulus. In contrast, the 45° and 90° FO specimens exhibit scattered compressive modulus values. Furthermore, 0° FO specimens possess a higher compressive modulus when compared to those in the 45° and 90° FO orientations. Focusing on the failure behaviour of 0° FO batches 2 and 3, both specimens reached their ultimate compressive strengths ( $\sigma_{UCS}$ ) of 196.78 MPa and 206.84 MPa respectively at the approximate strain = -0.065. Subsequent reductions in stress were indicative of specimen kinking, and the distinctive stress-strain characteristics of these two specimens following the load drop suggested potential evidence of differing failure mechanisms.

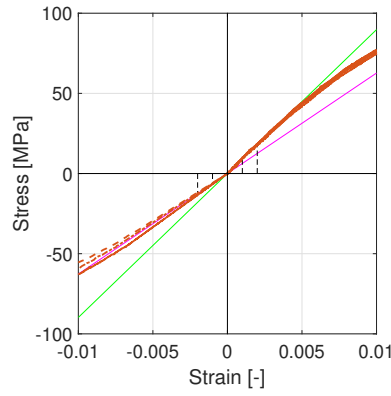
For a broader context, Figure 59(a) incorporates stress-strain curves under both compressive and tensile loading from the study by Y. Fujita [4]. Additional Figures 59(b), 59(c), and 59(d), showcase differences in tensile and compressive moduli at 0°, 45°, and 90° FO, respectively, by featuring tangents of average initial slopes. Numerical values of Young's moduli are presented in Table 11.



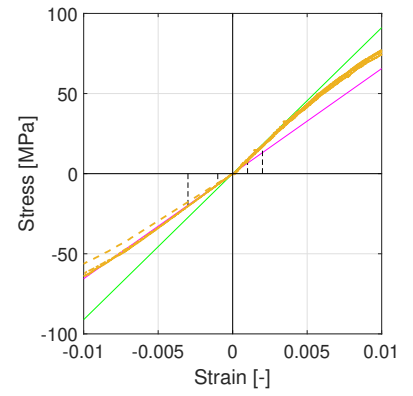
(a)



(b) 0° specimen zoomed-in, with average tensile modulus = 13.35 GPa (green), and average compression modulus = 9.67 GPa (pink).



(c) 45° specimen zoomed-in, with average tensile modulus = 8.98 GPa (green), and average compression modulus = 6.27 GPa (pink).



(d) 90° specimen zoomed-in, with average tensile modulus = 9.11 GPa (green), and average compression modulus = 6.56 GPa (pink).

**Figure 59:** Tensile and compressive stress-strain curves for IM-SFRP dogbone specimens.

**Table 11:** Tensile and compressive modulus of IM-SFRP dogbone specimens in 0°, 45°, and 90° FO.

FO, Specimen	Tensile Modulus (GPa)	Compressive Modulus (GPa)
0deg, specimen 1	13.3468	9.7509
0deg, specimen 2		9.4638
0deg, specimen 3		9.8100
45deg, specimen 1	8.9771	6.7361
45deg, specimen 2		5.8996
45deg, specimen 3		6.1700
90deg, specimen 1	9.1127	6.8188
90deg, specimen 2		5.9488
90deg, specimen 3		6.9070

Tensile tests of the SFRP specimens demonstrated its repeatability with consistent stress-strain curves in each FO, while compressive tests yielded more dispersed data. However, the trend of higher tensile modulus relative to compressive modulus was consistent across all FO. Furthermore, the tensile and compressive modulus values for 45° and 90° FO specimens were largely similar. Another key observation was that the SFRP specimens under compression lose their stiffness at a comparatively earlier strain relative to tension.

With the available 0° FO specimens data, comparative analysis between tensile and compressive loading revealed greater  $\sigma_{UCS}$  values at a higher strain than  $\sigma_{UTS}$  values. Although 45° and 90° FO specimens did not reach  $\sigma_{UCS}$ , the maximum strains and corresponding stresses achieved under compressive tests for batches 2 and 3 already surpassed  $\sigma_{UTS}$  and  $\epsilon_{UTS}$  recorded in tensile tests. This evidence indicates that IM-SFRP specimens generally exhibit higher  $\sigma_{UCS}$  than  $\sigma_{UTS}$  at higher strains.

### 5.2.2 Specimen Scans

Following the testing phase, a comprehensive analysis was conducted to investigate the failure mechanisms exhibited by the samples. Figures 60 and 61 portray the front scans of sample batches 2 and 3 respectively after compression. It's worth reiterating that specimen batch 2 was subjected to a displacement of 5.5 mm without grinding, while batch 3 was machined to ensure flat parallel surfaces and sharp, clean edges before being subjected to displacements of 6.5 mm.

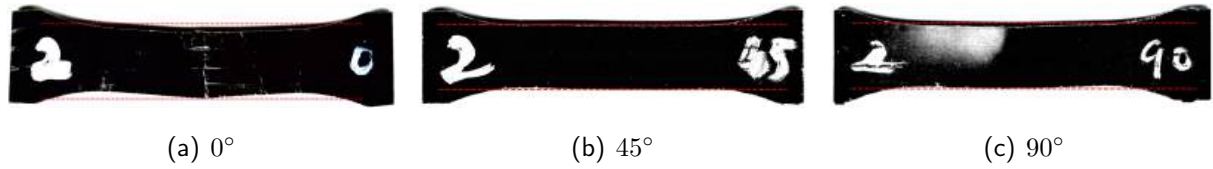


**Figure 60:** After-test scans of specimen batch 2.

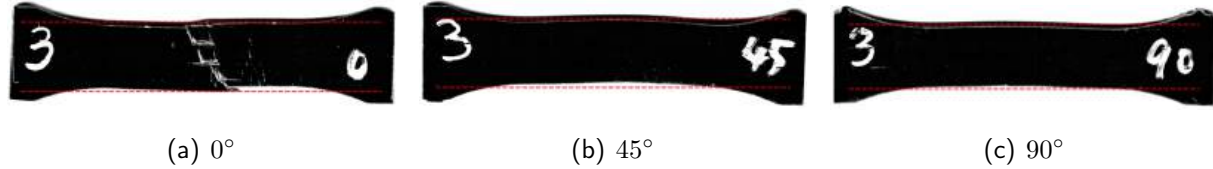


**Figure 61:** After-test scans of specimen batch 3.

Notably, lateral buckling is visible in the  $0^\circ$  FO specimen of batch 2 and all three FO specimens within batch 3. Although specimens batch 3 were subjected to edge grinding, this phenomenon is more pronounced in specimen batch 3 compared to batch 2. This discrepancy can be attributed to the longer loading displacement, resulting in a greater extent of compression within the specimens of batch 3 compared to batch 2. In addition, the absence of visible dents on any specimen edges implies that the specimens likely experienced evenly distributed loading, and the observed buckling were not likely to be introduced by surface finishing or unsymmetrical specimen cutting at the edges.

### 5.2.3 $0^\circ$ Specimen Failure Cycle Analysis

In order to gain a better understanding of the failure in  $0^\circ$  specimens, the  $0^\circ$  specimens in batch 1 were loaded in three cycles. In cycle 1, a displacement of 3.5 mm was applied, revealing no visible crack formation. In cycle 2, the same specimen was loaded until the initial load drop manifested. In cycle 3, the same specimen was subjected to a displacement of 6.5 mm, concluding with complete failure.

Figure 62 illustrates the stress-strain curves of the three loading cycles of the  $0^\circ$  specimens in batch 1. Concurrently, Figure 63 captures the specimen's front scans after cycles 2 and 3. During loading cycle 1, the specimen did not reach its ultimate compressive strength, hence no load drop was observed. Nevertheless, it exceeded its elastic limit. This scenario was confirmed in cycle 2, where the compressive modulus reduced compared to cycle 1, and the load drop occurred at a strain lower than the maximum strain of cycle 1. The specimen scan of cycle 2 reveals the initiation of a localised kink band approximately positioned at the midpoint of the gauge length, with no clear indication of global buckling. In loading cycle 3, the compressive modulus registered a further decline, signifying additional plastic strain accumulation from the second cycle. Following the first load drop in cycle 3, the specimen's strength displayed a degree of recovery, typically due to the strain-hardening behaviour of the polymer matrix. The



specimen scan of cycle 3 highlights the occurrence of global lateral buckling at the midpoint of the gauge length. In summary, the maximum load of  $0^\circ$  specimens in batch 1 appears to be primarily governed by localised failure, which was apparent from the crack initiation during cycle 2 and the subsequent global buckling manifested during cycle 3.

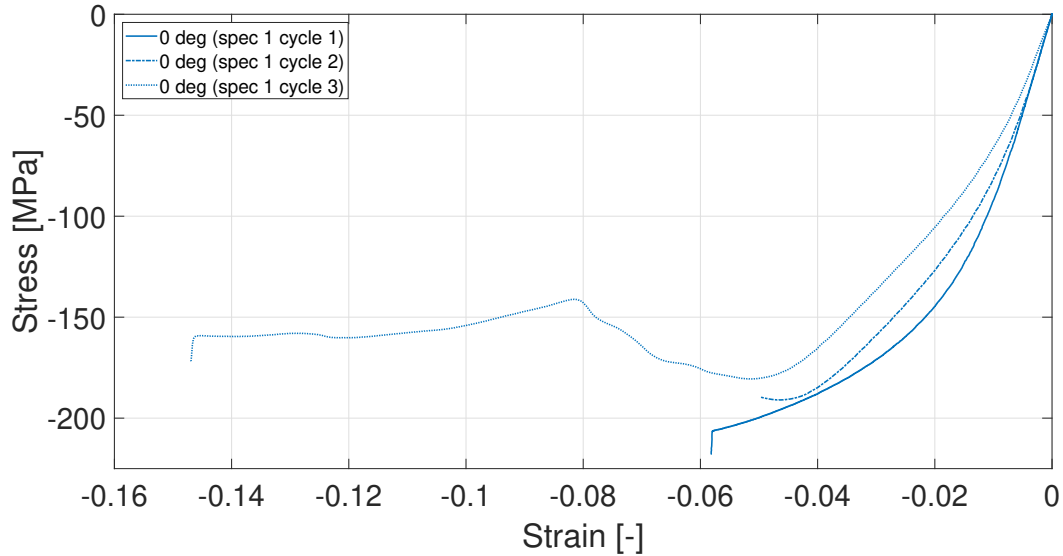


**Figure 62:** Compressive stress-strain curves for IM-SFRP dogbone specimens undergone three loading cycles.

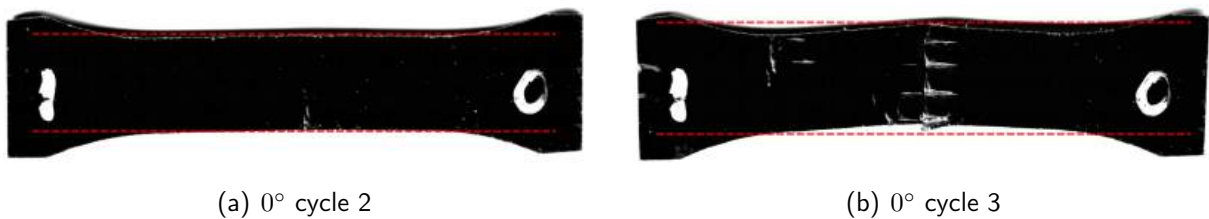


**Figure 63:** After-test scans of  $0^\circ$  specimen cycle 2 and 3.

## 5.3 Discussion

### 5.3.1 Preliminary Compressive Properties

#### Effect of Fibre Orientation :

In Figure 58, the compressive behaviour of SFRP specimens demonstrated varying modulus and consistency across different fibre orientations ( $0^\circ$ ,  $45^\circ$ ,  $90^\circ$  FO). Specifically,  $0^\circ$  FO specimens exhibited a more consistent and higher compressive modulus compared to those in  $45^\circ$  and  $90^\circ$ . This is because fibres aligned parallel to the loading direction ( $0^\circ$  FO) resist deformation more effectively than  $45^\circ$  and  $90^\circ$  FO. Thus, fibres in  $0^\circ$  FO bear a greater proportion of the load compared to the matrix, leading to higher compressive modulus. In contrast, the  $45^\circ$  and  $90^\circ$  FO specimens showed more scattered modulus values, potentially due to the more complex stress distribution in these orientations.

### **Young's Modulus in Compression vs Tension :**

The recorded compression modulus of the SFRP specimens was consistently lower than their tensile modulus, as compared in Figure 59. Theoretical considerations would suggest that for SFRP, the compressive and tensile moduli should be approximately equivalent, given that both properties are intimately linked to the material's inherent mechanical behaviour. However, the observed lower compression modulus suggests potential uneven loading of the specimen during compression, which cannot be visualised in the after-test specimen scans. Specifically, one corner of the specimen might have deformed prior to the other corners. Such localised behaviour could create an apparent lower material stiffness, thereby reducing the measured compressive modulus.

Another noteworthy observation is that SFRP specimens under compression lost stiffness at an earlier strain compared to tension. This is likely to be attributed to buckling phenomena, prominently observed in the specimens from batch 3 illustrated in Figure 61. In the case of tensile loading, the main failure mechanisms include fibre breakage and pull-out, both of which tend to occur at higher strains. In contrast, compressive failure is more commonly associated with kinking and buckling mechanisms, which typically manifest at comparatively lower strains.

### **Strength in Compression vs Tension :**

The compressive behaviour of SFRP resulted in higher ultimate compressive strengths ( $\sigma_{UCS}$ ) compared to ultimate tensile strengths ( $\sigma_{UTS}$ ). One possible explanation for this divergence lies in the nature of the fibre-matrix interaction under different loading conditions. During tensile loading, microcracks frequently initiate at the junctions between the matrix and fibre ends, primarily due to weak adhesion, as previously mentioned in Section 3.1.4. These microcracks then propagate through the shearing of the fibre-matrix interface, which facilitates fibre pull-out or breakage. Conversely, under compressive loading, forces are more directly transferred from the matrix to the fibre ends, preventing the promotion of microcracks. This direct transfer of load effectively enhances the composite's overall strength under compression.

### **5.3.2 Limitations of the Current Compression Test Methodology**

One of the important findings of Phase 3 is the limitation imposed by the current compression test methodology, which becomes particularly evident when considering the compressive behaviour of IM-SFRP specimens. Notably, the limited clearance between the jig and the specimen restricted further compression, especially for the 45° and 90° FO specimens. This restriction ended the loading process earlier than anticipated, disrupting a full exploration of the compressive failure mechanisms for these orientations. The sudden increase in stress corresponding with the platen's impact with the jig further confirms this limitation.

### **Inconsistency in Stress-Strain Curves :**

In Figure 59, the inconsistency observed in the compressive modulus for the 45° and 90° FO specimens is an additional point of concern. Such variation is absent in tensile testing conducted by Y. Fujita [4]. The dispersion in the data indicates that the current method may not provide an adequately representative characterisation of the compressive properties of these orientations. The 0° FO specimens, despite being more consistent, still presented a discernible difference in  $\sigma_{UCS}$  in specimen batches 2 and 3, which is not likely to be attributed to the grinding surface finish in batch 3.

### **Failure Mechanism and Buckling :**

Further complications arising from the visible lateral buckling in the scanned specimens are evidenced in Figures 60 and 61. The presence of buckling implies that the specimens might not have failed purely under compressive loading conditions. This buckling phenomenon, which was more pronounced in batch 3 due to the longer loading displacements, can distort the experimental data and thus compromise the integrity of the stress-strain curves.

The failure cycle analysis of the 0° FO specimens in Section 5.2.3 revealed a local-to-global failure mechanism from cycle 1 to cycle 3. In specific, the maximum load of the 0° specimen in batch 1 is likely to be governed by localised failure, which was evident by the initiation of a localised kink band in cycle 2, followed by the global buckling in cycle 3. Nonetheless, 45° and 90° specimens might not have experienced the same failure mechanisms since lateral buckling was observed before failure could occur. The inconsistency between specimens further reinforces the idea that the current compression test methodology is insufficiently robust for a comprehensive understanding of the failure mechanisms in IM-SFRP materials.

## **6 Conclusion**

The aim of this research was to improve the understanding and modelling of the mechanics of IM-SFRP and its fabricated components. It was structured into three main phases, each contributing to the overarching objective. Overall, it has helped identify crucial factors and considerations for future work regarding the applications of IM-SFRPs in the automotive industry.

### **6.1 Summary of Key Findings**

**Phase 1:** The first phase investigated the failure mechanisms of SFRPs under multi-axial loading. With the use of the single fibre matrix RVE, the following conclusions were deduced:

- Energy dissipation curves indicate that lower fracture toughness is not likely to be the reason behind the overestimation of critical failure load observed in previously conducted

puncture test simulations by Y. Fujita [4].

- The application of CZM is indispensable for realistically simulating the fibre-matrix interface and accurately capturing the failure mechanisms of SFRPs.

**Phase 2:** This phase explored the feasibility of virtual testing methodologies for the EM, specifically focusing on tensile testing simulations. With the use of coupled injection-moulding and FE simulations, the following revelations were made:

- IM-SFRP fabricated components with complex geometry can be accurately simulated by the coupled injection-moulding and FE simulations with CZM.
- Complex boundary conditions are required for realistic simulations, and simplifications of the loading model could lead to over-constraints and introduce overestimations of failure load.
- Existing software limitations in Digimat emphasise the criticality of appropriate skin-core morphology partitioning in CE and failure parameter selection.

**Phase 3:** The final phase provided insight into the compressive properties of SFRP specimens at different FO. Leveraging the compressive test data, this phase discovered:

- SFRP under compression exhibited different modulus and critical failure strength in all  $0^\circ$ ,  $45^\circ$  and  $90^\circ$  FO compared to those under tension.
- The current compression test methodology presented limitations, particularly for  $45^\circ$  and  $90^\circ$  FO in fully capturing the compressive failure mechanisms.
- The complexity and inconsistencies in the compressive behaviour of SFRPs suggest room for improvement in testing methodologies.

## 6.2 Implications

This research brings several contributions to the field of composite materials, particularly in the study of IM-SFRP. Firstly, the research validated the accuracy of virtual testing methodologies, particularly for the automotive industry. By successfully employing coupled injection-moulding and FE simulations to analyse the IM-SFRP fabricated EM, this research paves the way for scalable and efficient testing procedures in industrial contexts. The validated methodologies could save both time and resources, enabling quicker iterations in product development cycles and fostering innovation. Secondly, this research provides a preliminary exploration into the compressive properties of SFRP specimens, which fills a crucial gap in the current literature. This foundational knowledge is important for industries that heavily rely on materials with varied compressive and tensile strengths, such as automotive or aerospace engineering. Furthermore, the identification of limitations in existing compressive test methodologies sets the stage for more thorough and robust approaches to material testing in future studies.

## 7 Future Work

### 7.1 Phase 1

#### **Cohesive Element Thickness :**

The thickness of the fibre-matrix interface, which was represented by CE, was approximated to be 0.05  $\mu\text{m}$ . Parametric studies should be conducted to explore the impact of varying the CE thickness on the model's predictions.

#### **Strain Rate Effects on PA66 :**

In this study, the strain rate of the PA66 polymer matrix was assumed to be sufficiently low to not significantly affect the results. However, strain rate can affect the material properties. A review of the relevant literature and further simulations should be carried out to validate or adjust for the influence of the strain rate on PA66.

#### **Size Effect :**

The results of Phase 1 in this study, while insightful, do not conclusively account for the overestimation observed in the puncture tests. One possible area of research is the size effect inherent in composite materials like SFRPs. Notably, the strength of SFRPs can be expected to reduce with an increasing volume of the material tested. This behaviour can be attributed to the increased probability of encountering defects or inhomogeneities within a larger material sample, which can act as stress concentrators and initiate failure. Subsequent research should explore how the dimensions of the IM-SFRP specimen plate in puncture tests affect the composite's macroscopic characteristics. Particular attention should be given to disparities in energy dissipation and fracture toughness when comparing experimental results to coupled simulations.

#### **Spatial Variability :**

Another possible area for future research is exploring the spatial variability within the micro-scale RVE model. The current single-fibre matrix element model simplifies the interface interactions, ignoring the possibility that fibres are closely positioned to each other. In SFRPs, it is known that the fibre-matrix interface, characterised by the IFSS, is typically the weakest region, and has the most likelihood of failure initiation. When fibres are closely packed, the interfacial bonding between adjacent fibres can be even weaker than that between fibre and matrix, resulting in lower IFSS. For instance, if the IM-SFRP plate used in the puncture test is defective in a way that the impact region consists of fibres that are distributed very close together, this could potentially explain the overestimations observed in the simulation when compared to puncture test results. To investigate this effect more thoroughly, future work should develop RVE models with multiple fibres and varied spatial distributions.

## 7.2 Phase 2

### **Refinement of Layer Morphologies :**

A critical direction for future research in Phase 2 is the precise modelling of layer morphologies within the CE. One approach to consider is the addition of more partition layers. Instead of relying on the simplistic skin-core-skin configuration, a more intricate layout accommodating EM's complex geometry should be explored. This includes potential vertical partitioning at sidewalls and further refinement of horizontal partitions. While this approach is likely to offer a more accurate representation, it will also increase the computational demands due to the added complexity of material properties within the CE. Despite the accurate predictions obtained through the current partitioning methodology, the virtual testing methodology would also benefit from a more automated process to reduce errors associated with manually defining CE properties.

### **Industrial and Environmental Relevance :**

This study focused on EM produced using a single injection port and maintained at a DAM condition at 23 °C. However, it is typical in industrial settings to utilise multiple injection ports to optimise weldline locations for various loading scenarios. Future work could extend the present methodology to investigate different manufacturing configurations of IM-SFRP, enhancing its industrial relevance. Additionally, future research should employ the developed methodology to examine EM under varying environmental conditions such as temperature and moisture levels. This will yield insights into the EM's real-world performance throughout its lifecycle, which is invaluable for practical applications.

### **Experimental Validation of Stiffening Effect :**

Lastly, the theoretical explanations for the observed stiffening effect, primarily attributed to pin misalignment, require experimental validation. Conducting tensile tests with intentionally exaggerated pin misalignments could offer empirical evidence. If a more pronounced stiffening effect is observed in these tests compared to those without intentional pin misalignment, it would substantiate the current hypothesis.

## 7.3 Phase 3

### **Alternative Test Setups :**

The limitations in the current ASTM D695 test setup point towards the necessity of exploring alternative test setups that could allow for a more comprehensive evaluation of compressive properties. ASTM D3410 [79] and ASTM D6641 [80], as illustrated in Figures 64(a) and 64(b), are two possible alternatives. One significant advantage of both ASTM D3410 and

ASTM D6641 is that they allow the use of the entire gauge length of the specimen in compression tests. Thus, 45° and 90° FO specimens can be subjected to longer loading displacements, achieving specimen failure. However, both ASTM D3410 and ASTM D6641 involve unsupported gauge lengths, which introduces the risk of out-of-plane and in-plane buckling of the specimens. Additional modifications are required to restrain specimens from buckling behaviour. Furthermore, these test setups tend to be more complex in their requirements for specialised fixtures, which could potentially escalate both the cost and time needed for testing.

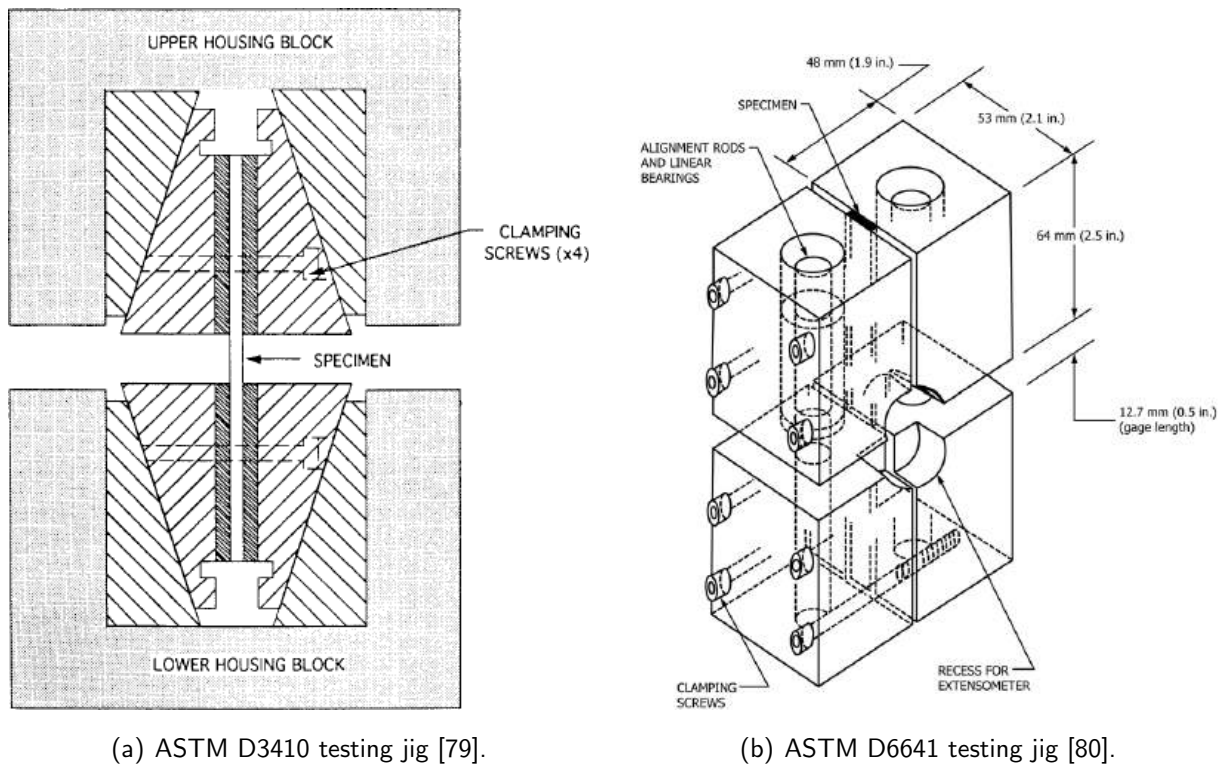


**Figure 64:** Alternative test standards for compressive properties.

### Longer Specimens :

The restricted clearance between the jig and the specimen in the current setup was identified as a major limitation. One straightforward approach to address this issue is to employ longer specimens. By extending the loading sections of the specimen, it becomes feasible to obtain stress-strain curves that span a broader range, thereby capturing the full scope of failure mechanisms in 45° and 90° specimens.

### Wider Specimens :

The presence of in-plane buckling, particularly in specimens of batch 3, raises concerns about the data's validity. Wider specimens could be used in future experiments to mitigate this phenomenon. Increasing specimen width can provide better in-plane stability under compressive loads, reducing the risk of lateral buckling, thus, generating more reliable data.

### Smaller Radius in Dogbone Specimen Curves :

The dogbone shape, commonly used in tensile testing, was employed in the current study for compressive testing. However, the results indicate that the current design may not be entirely suitable for compression tests, especially considering the dissimilar failure mechanisms of IM-SFRP under tensile and compressive loads. Reducing the radius in the curves of the dogbone design could lead to a shorter neck section, resulting in more concentrated energy and load distribution within the gauge length. This adjustment could offer insights into different aspects of failure mechanisms under compression.

## 7.4 Integration Across Phases

### Tensile and Compressive Behavior :

The findings across Phases 1, 2, and 3 consistently point towards the need to differentiate between tensile and compressive material properties in future work. Phase 3 specifically highlighted the variation in modulus, strength, and failure stress and strain when PA66-GF50 is subjected to tensile versus compressive loading. It is considered that Phase 1 identified a multi-axial stress state involving compression in the SFRP during puncture tests, and Phase 2 noted regions of compressive stress under tensile tests, as seen in Figure 65. Therefore, an isotropic material property approximation for each component (fibre, matrix, and CE) in Phase 1 and the general PA66-GF50 material model created with Digimat-MF is a limitation in the current modelling approach.

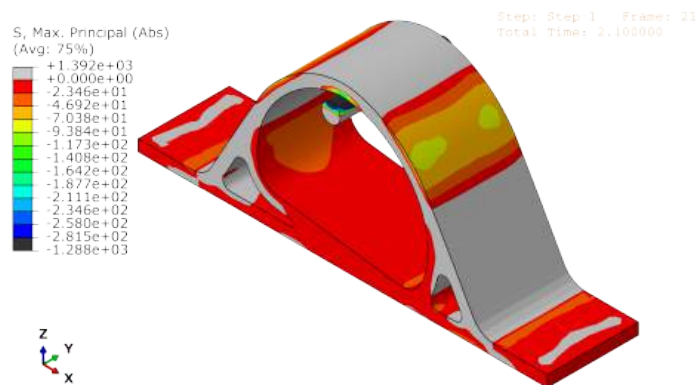


**Figure 65:** Regions of the EM under compressive stress state.

To enhance the accuracy and predictive capability of the simulations, future research should integrate the tensile and compressive material properties of PA66-GF50 obtained from Phase 3 into the computational models of Phases 1 and 2. For instance, Phase 1's single fibre matrix element RVE and Phase 2's EM could be refined to include tension-compression anisotropic material properties. Such an integrated approach would not only improve the model's validity but also a better understanding of the material's behaviour under complex loading conditions.



## References

- [1] Somjate Patcharaphun and Gunter Mennig. Prediction of tensile strength for sandwich injection molded short-glass-fiber reinforced thermoplastics. *Journal of metals, materials and minerals*, 17(2), 2007.
- [2] Asahi kasei engineering plastic applications. [https://www.asahi-kasei-plastics.com/en/case\\_category/automotive/#modal6](https://www.asahi-kasei-plastics.com/en/case_category/automotive/#modal6)[accessed: 2023-01-04].
- [3] SM Mirkhalaf, EH Eggels, TJH van Beurden, F Larsson, and M Fagerström. A finite element based orientation averaging method for predicting elastic properties of short fiber reinforced composites. *Composites Part B: Engineering*, 202:108388, 2020.
- [4] Yuki Fujita. Proc. analysing and predicting failure of injection-moulded short-fibre composite components. *Proc. Composites Meet Sustainability, 20th European Conference on Composite Materials, ECCM20. 26-30 June, 2022, Lausanne, Switzerland, 2022*.
- [5] Joonhee Lee, Hyungyi Lee, and Naksoo Kim. Fiber orientation and strain rate-dependent tensile and compressive behavior of injection molded polyamide-6 reinforced with 20% short carbon fiber. *Polymers*, 15(3):738, 2023.
- [6] S Daggumati, A Sharma, A Kasera, and N Upadhyay. Failure analysis of unidirectional ceramic matrix composite lamina and cross-ply laminate under fiber direction uniaxial tensile load: cohesive zone modeling and brittle fracture mechanics approach. *Journal of Materials Engineering and Performance*, 29:2049–2060, 2020.
- [7] Yuki Fujita. Proc. failure prediction of injection-moulded short-fibre composite components using cohesive zone modelling. *Proc. 10th International Conference on Composites Testing and Model Identification, Lille, 2021, 2021*.
- [8] YA Lizama-Camara and Pinna. Effect of the injection moulding fibre orientation distribution on the fatigue life of short glass fibre reinforced plastics for automotive applications. *Procedia CIRP*, 85, 2019.
- [9] Matmatch pa66-gf50 material properties. <https://matmatch.com/materials/mbas135-polyamide-66-reinforced-with-50-glass-fibers-pa66-gf50->[accessed: 2022-11-05].
- [10] Matmatch aisi1020 cold-rolled material properties. <https://matmatch.com/materials/smcs007-aisi-1020-cold-rolled>[accessed: 2022-11-05].
- [11] Rhoda Miel. Nissan rogue tailgate-garners top spe award, Nov 2014. <https://www.plasticsnews.com/article/20131107/NEWS/131109941/nissan-rogue-tailgate-garners-top-spe-award#:~:text=The%20tailgate%20won%20Nissan%20both,6%20in%20Livonia.>[accessed: 2022-11-05].

- [12] M De Monte and Moosbrugger. Influence of temperature and thickness on the off-axis behaviour of short glass fibre reinforced polyamide 6.6–cyclic loading. *CPA: Applied Science and Manufacturing*, 41(10), 2010.
- [13] M De Monte, E Moosbrugger, and Marino Quaresimin. Influence of temperature and thickness on the off-axis behaviour of short glass fibre reinforced polyamide 6.6–quasi-static loading. *Composites Part A: Applied Science and Manufacturing*, 41(7):859–871, 2010.
- [14] M Vogler, R Rolfes, and PP Camanho. Modeling the inelastic deformation and fracture of polymer composites–part i: Plasticity model. *Mechanics of Materials*, 59:50–64, 2013.
- [15] A Rashedi, I Sridhar, and KJ Tseng. Fracture characterization of glass fiber composite laminate under experimental biaxial loading. *Composite Structures*, 138:17–29, 2016.
- [16] A Dean, N Grbic, R Rolfes, and B Behrens. Macro-mechanical modeling and experimental validation of anisotropic, pressure-and temperature-dependent behavior of short fiber composites. *Composite Structures*, 211:630–643, 2019.
- [17] Luca Quagliato, Joonhee Lee, João Henrique Fonseca, Dosuck Han, Hyungyil Lee, and Naksoo Kim. Influences of stress triaxiality and local fiber orientation on the failure strain for injection-molded carbon fiber reinforced polyamide-6. *Engineering Fracture Mechanics*, 250:107784, 2021.
- [18] Alexandru Isaincu, Micota Dan, Viorel Ungureanu, and Liviu Marșavina. Numerical investigation on the influence of fiber orientation mapping procedure to the mechanical response of short-fiber reinforced composites using moldflow, digimat and ansys software. *Materials today: proceedings*, 45:4304–4309, 2021.
- [19] Haoran Li. Simulation of injection-moulded composite structures for automotive applications. *Final Thesis for the Master of Science Degree, Department of Mechanical Engineering, IMPERIAL COLLEGE LONDON*, 2022.
- [20] Jörg Schröder and Klaus Hackl. *Plasticity and beyond: microstructures, crystal-plasticity and phase transitions*, volume 550. Springer, 2013.
- [21] Jayant M Mahishi. An integrated micromechanical and macromechanical approach to fracture behavior of fiber-reinforced composites. *Engineering fracture mechanics*, 25(2):197–228, 1986.
- [22] Arwen Smits, Danny Van Hemelrijck, TP Philippidis, and Albert Cardon. Design of a cruciform specimen for biaxial testing of fibre reinforced composite laminates. *Composites science and technology*, 66(7-8):964–975, 2006.
- [23] SH Chen and B Feng. Size effect in micro-scale cantilever beam bending. *Acta Mechanica*, 219:291–307, 2011.

- [24] Muammer Koç, Eren Billur, and Ömer Necati Cora. An experimental study on the comparative assessment of hydraulic bulge test analysis methods. *Materials & Design*, 32(1):272–281, 2011.
- [25] Fernand Ellyin and John D Wolodko. Testing facilities for multiaxial loading of tubular specimens. *ASTM special technical publication*, 1280:7–24, 1997.
- [26] A Makinde, L Thibodeau, and KW Neale. Development of an apparatus for biaxial testing using cruciform specimens. *Experimental mechanics*, 32:138–144, 1992.
- [27] MJKA Hinton, PD Soden, and Abdul-Salam Kaddour. *Failure criteria in fibre reinforced polymer composites: the world-wide failure exercise*. Elsevier, 2004.
- [28] MJ Hinton and AS Kaddour. The background to the second world-wide failure exercise. *Journal of composite materials*, 46(19-20):2283–2294, 2012.
- [29] PP Camanho, MA Bessa, G Catalanotti, M Vogler, and R Rolfes. Modeling the inelastic deformation and fracture of polymer composites–part ii: Smeared crack model. *Mechanics of Materials*, 59:36–49, 2013.
- [30] AR Melro, PP Camanho, FM Andrade Pires, and ST Pinho. Micromechanical analysis of polymer composites reinforced by unidirectional fibres: Part i–constitutive modelling. *International Journal of Solids and Structures*, 50(11-12):1897–1905, 2013.
- [31] AR Melro, PP Camanho, FM Andrade Pires, and ST Pinho. Micromechanical analysis of polymer composites reinforced by unidirectional fibres: Part ii–micromechanical analyses. *International Journal of Solids and Structures*, 50(11-12):1906–1915, 2013.
- [32] Marcelo Leite Ribeiro, Volnei Tita, and Dirk Vandepitte. A new damage model for composite laminates. *Composite Structures*, 94(2):635–642, 2012.
- [33] AB De Morais. Evaluation of a trilinear traction-separation law for mode ii delamination using the effective crack method. *Composites Part A: Applied Science and Manufacturing*, 121:74–83, 2019.
- [34] Sylvain Drapier, Jean-Claude Grandidier, and Michel Potier-Ferry. Towards a numerical model of the compressive strength for long fibre composites. *European Journal of Mechanics-A/Solids*, 18(1):69–92, 1999.
- [35] S Drapier, J-C Grandidier, and M Potier-Ferry. A structural approach of plastic microbuckling in long fibre composites: comparison with theoretical and experimental results. *International Journal of Solids and Structures*, 38(22-23):3877–3904, 2001.
- [36] SR Frost. Compressive behaviour of long-fibre unidirectional composites. *Journal of Composite Materials*, 26(8):1151–1172, 1992.

- [37] D Liu, NA Fleck, and MPF1102 Sutcliffe. Compressive strength of fibre composites with random fibre waviness. *Journal of the Mechanics and Physics of Solids*, 52(7):1481–1505, 2004.
- [38] BG Green, MR Wisnom, and SR Hallett. An experimental investigation into the tensile strength scaling of notched composites. *Composites Part A: Applied Science and Manufacturing*, 38(3):867–878, 2007.
- [39] SILVIA Fara and ANDREA Pavan. Fibre orientation effects on the fracture of short fibre polymer composites: on the existence of a critical fibre orientation on varying internal material variables. *Journal of materials science*, 39:3619–3628, 2004.
- [40] FT Ibáñez-Gutiérrez, S Cicero, and IA Carrascal. On the influence of moisture content on the fracture behaviour of notched short glass fibre reinforced polyamide 6. *Composites Part B: Engineering*, 159:62–71, 2019.
- [41] D Ferreno, I Carrascal, E Ruiz, and JA Casado. Characterisation by means of a finite element model of the influence of moisture content on the mechanical and fracture properties of the polyamide 6 reinforced with short glass fibre. *Polymer testing*, 30(4):420–428, 2011.
- [42] A Hassan, R Yahya, AH Yahaya, ARM Tahir, and PR Hornsby. Tensile, impact and fiber length properties of injection-molded short and long glass fiber-reinforced polyamide 6, 6 composites. *Journal of reinforced plastics and composites*, 23(9):969–986, 2004.
- [43] Aziz Hassan, Asfarina A Hassan, and MI Mohd Rafiq. Impact properties of injection molded glass fiber/polyamide-6 composites: effect of testing parameters. *Journal of reinforced plastics and composites*, 30(10):889–898, 2011.
- [44] Bouchaib Mouhmid, Abdellatif Imad, Noureddine Benseddiq, and D Lecompte. An experimental analysis of fracture mechanisms of short glass fibre reinforced polyamide 6, 6 (sgfr-pa66). *Composites science and technology*, 69(15-16):2521–2526, 2009.
- [45] SY Fu, B Lauke, E Mäder, X Hu, and CY Yue. Fracture resistance of short-glass-fiber-reinforced and short-carbon-fiber-reinforced polypropylene under charpy impact load and its dependence on processing. *Journal of Materials Processing Technology*, 89:501–507, 1999.
- [46] Thanh-Phong Dao, Hieu Giang Le, and Shyh-Chour Huang. Investigation of formulation of the energy release rate in the fracture mechanics of short fiber composite. *Journal of Engineering Technology and Education*, 9(4):451–459, 2012.
- [47] J Karger-Kocsis. Instrumented impact fracture and related failure behavior in short- and long-glass-fiber-reinforced polypropylene. *Composites science and technology*, 48(1-4):273–283, 1993.

- [48] M Akay, DF O'regan, and RS Bailey. Fracture toughness and impact behaviour of glass-fibre-reinforced polyamide 6, 6 injection mouldings. *Composites Science and Technology*, 55(2):109–118, 1995.
- [49] J Karger-Kocsis and K Friedrich. Fracture behavior of injection-molded short and long glass fiber—polyamide 6.6 composites. *Composites Science and Technology*, 32(4):293–325, 1988.
- [50] ZA Mohd Ishak, US Ishiaku, and J Karger-Kocsis. Microstructure-related fracture behaviour of injection moulded short fibre reinforced polyarylamide in dry and wet states. *Journal of materials science*, 33:3377–3389, 1998.
- [51] N Takeda, DY Song, and K Nakata. Effects of temperature and water content on impact properties of injection-molded glass nylon-6 composites. *Advanced Composite Materials*, 5(3):201–212, 1996.
- [52] Soraia Pimenta, Silvestre T Pinho, Paul Robinson, Kok H Wong, and Stephen J Pickering. Mechanical analysis and toughening mechanisms of a multiphase recycled cfrp. *Composites Science and Technology*, 70(12):1713–1725, 2010.
- [53] Silvestre T Pinho, Paul Robinson, and Lorenzo Iannucci. Fracture toughness of the tensile and compressive fibre failure modes in laminated composites. *Composites science and technology*, 66(13):2069–2079, 2006.
- [54] RW Truss, PJ Hine, and RA Duckett. Interlaminar and intralaminar fracture toughness of uniaxial continuous and discontinuous carbon fibre/epoxy composites. *Composites Part A: Applied Science and Manufacturing*, 28(7):627–636, 1997.
- [55] Giuseppe Catalanotti, PP Camanho, J Xavier, CG Dávila, and AT Marques. Measurement of resistance curves in the longitudinal failure of composites using digital image correlation. *Composites Science and Technology*, 70(13):1986–1993, 2010.
- [56] Donald S Dugdale. Yielding of steel sheets containing slits. *Journal of the Mechanics and Physics of Solids*, 8(2):100–104, 1960.
- [57] Grigory Isaakovich Barenblatt. The mathematical theory of equilibrium cracks in brittle fracture. *Advances in applied mechanics*, 7:55–129, 1962.
- [58] Y Mi, Michael A Crisfield, GAO Davies, and HB Hellweg. Progressive delamination using interface elements. *Journal of composite materials*, 32(14):1246–1272, 1998.
- [59] Olivier Allix, P Ladeveze, and Alberto Corigliano. Damage analysis of interlaminar fracture specimens. *Composite structures*, 31(1):61–74, 1995.
- [60] Maurício V Donadon, Sérgio Frascino M De Almeida, Mariano A Arbelo, Alfredo R de Faria, et al. A three-dimensional ply failure model for composite structures. *International Journal of Aerospace Engineering*, 2009, 2009.

- [61] Ron HJ Peerlings, René de Borst, WAM Brekelmans, and Marc GD Geers. Gradient-enhanced damage modelling of concrete fracture. *Mechanics of Cohesive-frictional Materials: An International Journal on Experiments, Modelling and Computation of Materials and Structures*, 3(4):323–342, 1998.
- [62] A Needleman. An analysis of tensile decohesion along an interface. *Journal of the Mechanics and Physics of Solids*, 38(3):289–324, 1990.
- [63] Viggo Tvergaard and John W Hutchinson. The relation between crack growth resistance and fracture process parameters in elastic-plastic solids. *Journal of the Mechanics and Physics of Solids*, 40(6):1377–1397, 1992.
- [64] Viggo Tvergaard and John W Hutchinson. The influence of plasticity on mixed mode interface toughness. *Journal of the Mechanics and Physics of Solids*, 41(6):1119–1135, 1993.
- [65] Lucas Amaro de Oliveira and Mauricio Vicente Donadon. Delamination analysis using cohesive zone model: A discussion on traction-separation law and mixed-mode criteria. *Engineering Fracture Mechanics*, 228:106922, 2020.
- [66] Fransisco Folgar and Charles L Tucker III. Orientation behavior of fibers in concentrated suspensions. *Journal of reinforced plastics and composites*, 3(2):98–119, 1984.
- [67] Colin Eberhardt and Ashley Clarke. Fibre-orientation measurements in short-glass-fibre composites. part i: automated, high-angular-resolution measurement by confocal microscopy. *Composites Science and Technology*, 61(10):1389–1400, 2001.
- [68] G Gsellmann, M Jerabek, and D Salaberger. Comparison of predicted and measured fiber orientations in injection molded parts. In *Proc. 6th Conf. Ind. Comput. Tomogr*, 2016.
- [69] Huan-Chang Tseng, Rong-Yeu Chang, and Chia-Hsiang Hsu. Improved fiber orientation predictions for injection molded fiber composites. *Composites Part A: Applied Science and Manufacturing*, 99:65–75, 2017.
- [70] John Douglas Eshelby. The determination of the elastic field of an ellipsoidal inclusion, and related problems. *Proceedings of the royal society of London. Series A. Mathematical and physical sciences*, 241(1226):376–396, 1957.
- [71] D Hibbit, B Karlsson, and P Sorensen. Abaqus/standard analysis user’s manual. *Hibbit, Karlsson, Sorensen Inc, Providence, USA*, 2007.
- [72] Srinivas C Tadepalli, Ahmet Erdemir, and Peter R Cavanagh. Comparison of hexahedral and tetrahedral elements in finite element analysis of the foot and footwear. *Journal of biomechanics*, 44(12):2337–2343, 2011.

- [73] Antonio Bilotta, Giovanni Formica, and Emilio Turco. Performance of a high-continuity finite element in three-dimensional elasticity. *International Journal for Numerical Methods in Biomedical Engineering*, 26(9):1155–1175, 2010.
- [74] Daljeet K Singh, Amol Vaidya, Vinoy Thomas, Merlin Theodore, Surbhi Kore, and Uday Vaidya. Finite element modeling of the fiber-matrix interface in polymer composites. *Journal of Composites Science*, 4(2):58, 2020.
- [75] Pedro Ponces Camanho, C G Davila, and MF De Moura. Numerical simulation of mixed-mode progressive delamination in composite materials. *Journal of composite materials*, 37(16):1415–1438, 2003.
- [76] JL Thomason. Structure–property relationships in glass-reinforced polyamide, part 1: The effects of fiber content. *Polymer composites*, 27(5):552–562, 2006.
- [77] Michael B Stephenson and Ted D Blacker. Using conjoint meshing primitives to generate quadrilateral and hexahedral elements in irregular regions. Technical report, Sandia National Labs., Albuquerque, NM (USA), 1989.
- [78] Astm d695-15 standard test method for compressive properties of rigid plastics, 2015.
- [79] American Society for Testing and Materials. *Standard Test Method for Compressive Properties of Polymer Matrix Composite Materials with Unsupported Gage Section by Shear Loading*. ASTM International, 2006.
- [80] D ASTM et al. Standard test method for compressive properties of polymer matrix composite materials using a combined loading compression (clc) test fixture. ASTM West Conshohocken, PA, 2009.
- [81] Marcio Loos. *Carbon nanotube reinforced composites: CNT Polymer Science and Technology*. Elsevier, 2014.

## A Appendix

### A.1 Halpin-Tsai SFRP model

The Halpin–Tsai model equations [81] were used as an index to validate the FE model prediction of the PA66-GF50 modulus. For composites with aligned short fibres, the Halpin–Tsai model describes the modulus of elasticity as shown in Equation A.1 and A.2. Notably, the Halpin–Tsai equations predict the modulus to be 18.74GPa; the experimental tensile curve exhibited a modulus of 19.08GPa; the single fibre matrix element model resultant in a modulus of 15.01GPa.

$$\frac{E_c}{E_m} = \frac{1 + \eta \zeta V_f}{1 - \eta V_f} \quad (\text{A.1})$$

$$\eta = \frac{E_f/E_m - 1}{E_f/E_m + \zeta} \quad (\text{A.2})$$

where  $\eta$  is a parameter that depends on the geometry of the fibre,  $\eta = \frac{2l_f}{d}$  was used for the calculation of the longitudinal modulus.

### A.2 Effect of EM sliding

To investigate the effect of the EM sliding, the horizontal and vertical displacements of the side trackers were plotted and compared with the load-displacement curves of the four tensile tests, as shown in Figures A.1, A.2, A.3 and A.4. To facilitate clear comparisons, the x-axis of all curves characterises the vertical displacement of the top tracker.

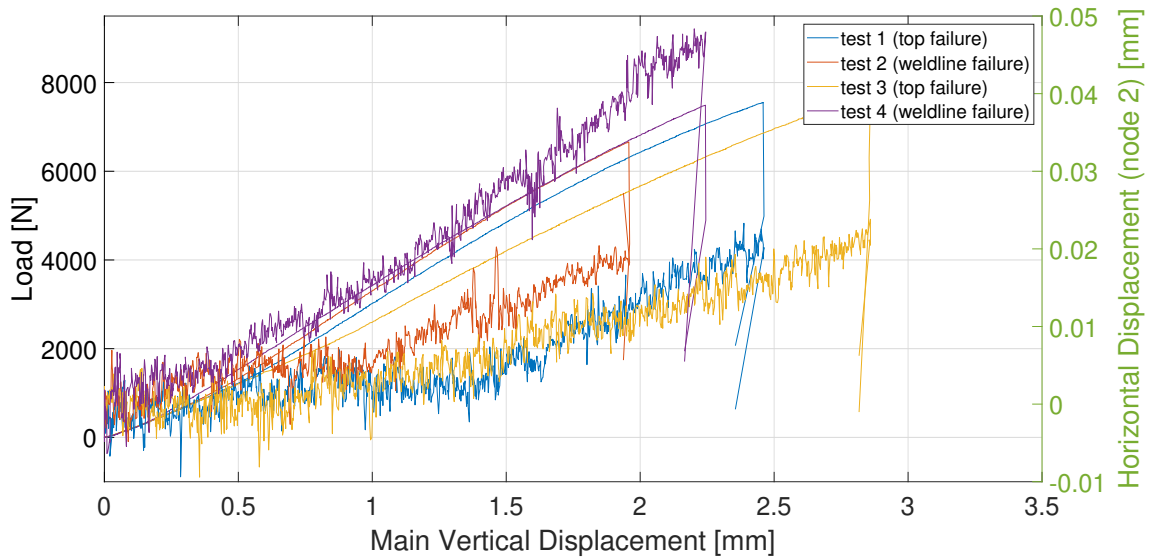


**Figure A.1:** Horizontal displacements of the left tracker recorded in tensile tests.



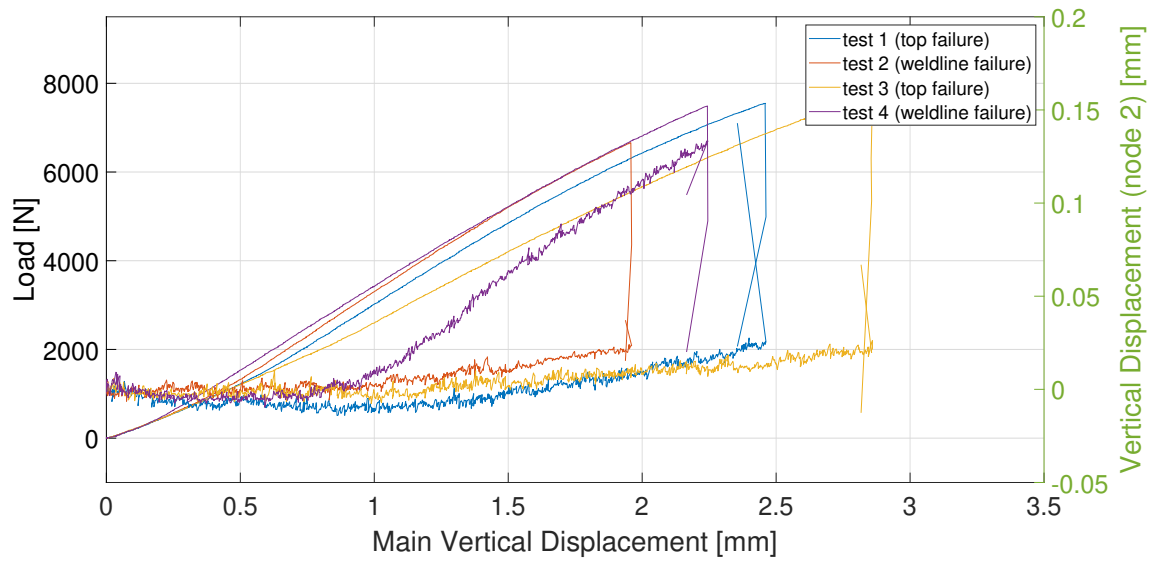


**Figure A.2:** Vertical displacements of the left tracker recorded in tensile tests.

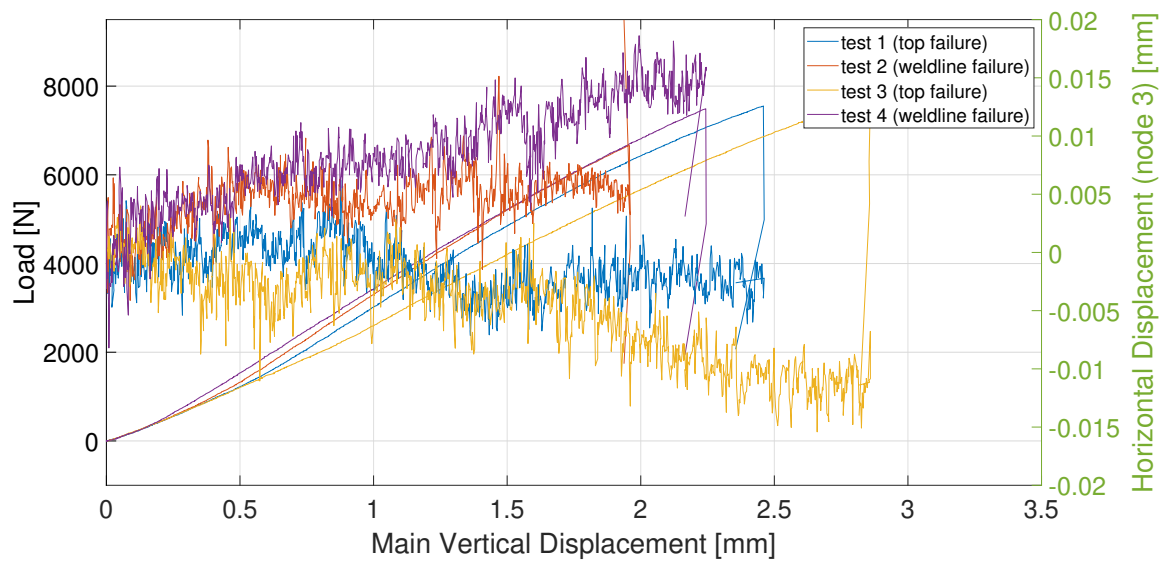


**Figure A.3:** Horizontal displacements of the right tracker recorded in tensile tests.

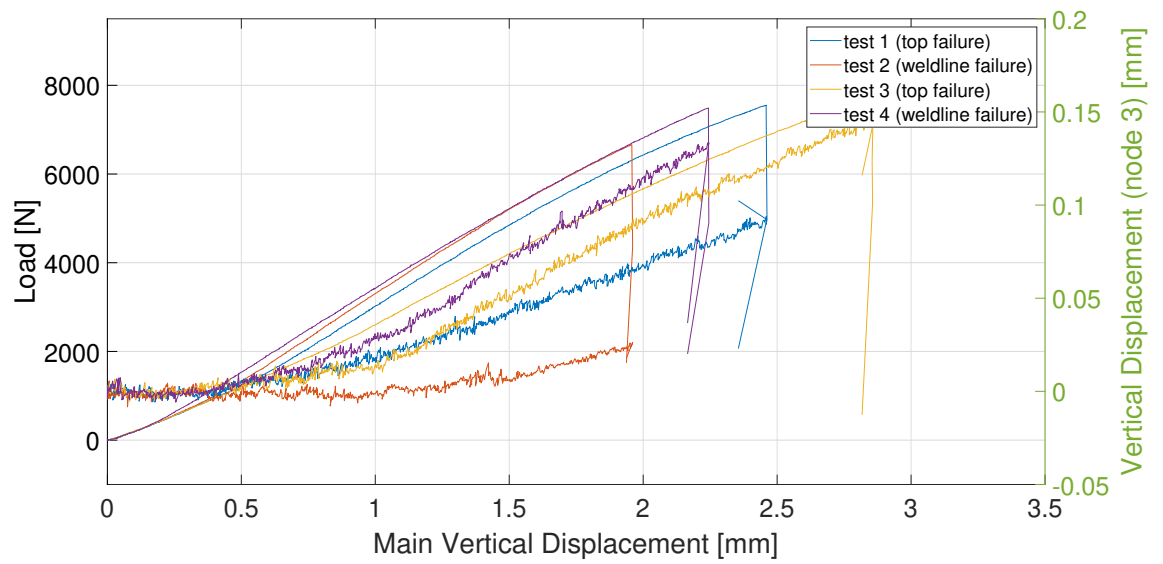


**Figure A.4:** Vertical displacements of the right tracker recorded in tensile tests.